Université de Strasbourg

UNIVERSITÉ DE STRASBOURG

THÈSE DE DOCTORAT

pour obtenir le titre de

DOCTEUR EN PHYSIQUE DE LA MATIÈRE CONDENSÉE

L'influence de la relaxation structurale au mouvement du spin d'électrons dans des systèmes ferromagnétiques: expérience et théorie

---

par HALLAL Ali

soutenue le 13 October, 2011

Membres du Jury:

Directeur de Thése	: Wolfgang Weber
Rapporteur Externe	: Hubert Ebert
	: Yves Lassailly
Examinateur	: Hugues Dreysse.
Invité	: Mébarek Alouani

Institut de physique et Chimie des Matériaux de Strasbourg

IPCMS

A mes parents,
et a mon épouse

"Science consists of two parts - experiment and theory - which are in constant interplay with each other. It is hardly possible to carry out a meaningful experiment, unless one has a specific idea or theory in mind, and a scientific theory is worthless unless it is based on experimental observations."
Per-Olov Löwdin (1916-2000)

Résumé

La structure des interfaces dans des films magnétiques joue un rôle crucial dans les dispositifs du spintronique. En fait, un certain nombre de travaux expérimentaux et théoriques ont été consacrées à étudier l'influence de la structure interfaciale sur la magnétorésistance tunnel (TMR), en particulier dans la jonction tunnel magnétique (JTM) Fe/MgO/Fe. La plupart de ces recherches ont été concentrées sur l'effet de désordre, d'oxydation, ou des vacances de O et Mg [1, 2, 3, 4]. D'autre part, il y a très peu d'études sur la relation entre la relaxation structurale et la transmission (ou réflexion) dépendant du spin [5, 6]. Ces études ont montrés que l'amélioration de l'effet de magnétorésistance est possible en contrôlant la structure.

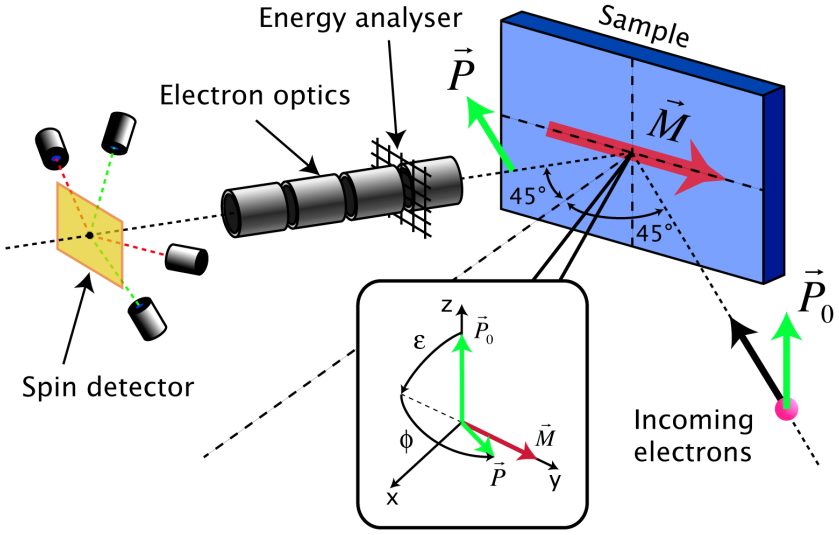

Figure 1: L'expérience consiste en une source d'électrons polarisés en spin, un échantillon ferromagnétique, une grille de retard pour l'analyse d'énergie et un système de détection de spin. Les deux types de mouvement de spin, à savoir une précession d'un angle ε et une rotation d'un angle ϕ, sont définis dans l'encadré.

Pour tenter de démêler les propriétés interfaciales dépendantes du spin, des expériences dans lesquelles la polarisation de spin des électrons est mesurée avant et après l'interaction avec un film ferromagnétique sont effectuées. Dans ces expériences un faisceau d'électrons polarisés en spin, dont la polarisation initiale $\mathbf{P_0}$ est perpendiculaire à l'aimantation $\mathbf{M}$ du film ferromagnétique, présente deux types de mouvement du spin lors de sa réflexion sur le film

ferromagnétique [7, 8]: une précession de la polarisation **P** autour de **M** d'un angle ε et une rotation d'un angle ϕ dans le plan engendré par **P** et **M** (voir encadré en Fig. 1).

La Figure 1 montre le schéma du dispositif expérimental, qui consiste en une source d'électrons polarisés en spin, un film ferromagnétique, un analyseur d'énergie et un détecteur de spin, le tout maintenu sous ultravide. Le faisceau d'électrons polarisés est obtenu à partir d'un cristal de GaAs par pompage optique avec de la lumière polarisée circulairement. Le faisceau incident est à 45° par rapport à la surface de l'échantillon. Pour observer un mouvement de spin maximale, $\mathbf{P_0}$ doit être orienté perpendiculairement par rapport à **M** du film. La polarisation de spin des électrons élastiques réflechis par l'échantillon, auxquelles on a limité notre étude, est finalement mesurée par un détecteur de spin.

Dans la première partie de ma thèse on a étudié le mouvement de spin de l'électron en réflexion à partir d'un film mince ferromagnétique de Fe pendant sa croissance sur Ag (001). Comme les paramètres de maille de Fe et Ag sont différentes, la croissance pseudomorphe de Fe induit l'accumulation d'énergie élastique. A partir d'une épaisseur critique cette énergie est libérée par la création des dislocations interfaciales dans le film [9]. Par conséquent, le paramètre de maille du film devrait varier dans une large gamme d'épaisseur.

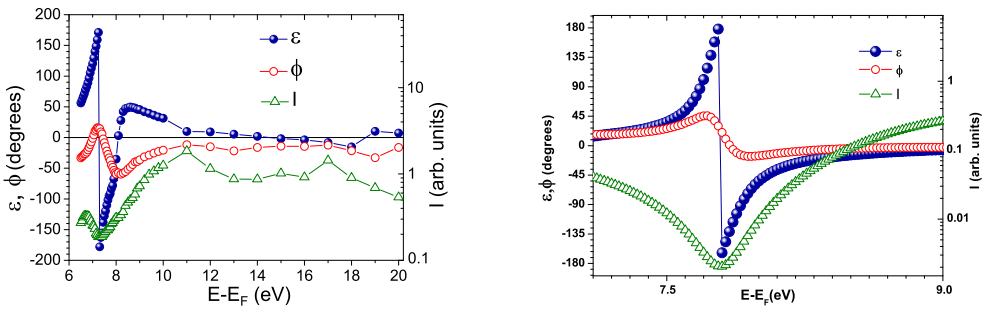

Figure 2: (Gauche) La réflectivité I intégrée en spin, l'angle de précession ε et l'angle de rotation ϕ en fonction de l'énergie des électrons primaires $E - E_F$ pour une épaisseur de Fe de 4,6 nm après recuit à 420 K. (Droite) I, ε et ϕ calculés en fonction de l'énergie des électrons primaires pour un film de Fe complétement rélaxé.

Nos expériences sur les films de Fe déposés sur la surface d'Ag(001) ont montré que ε peut atteindre sa valeur maximale possible, à savoir 180° (cf.

Fig. 2 (gauche)). Il s'agit de la limite ultime pour la manipulation de spin en réflexion. L'existence de cette précession de spin géante semble être très sensible à la relaxation du film de Fe au cours de sa croissance. En fait, un recuit, qui est reconnu pouvoir favoriser la relaxation des contraintes, est nécessaire pour obtenir cette valeur de précession géante. Afin de vérifier l'effet de la relaxation du maille sur la précession de spin, des calculs SPLEED (spin-dependent low energy electron diffraction) ont été effectués pour différents degrés de relaxations de la maille. La structure de bande électronique est calculée en utilisant l'approximation LMTO (Linear Muffin-Tin Orbitals) [10], qui offre un potentiel convergé pour faire le calcul SPLEED à l'aide de la méthode Korringa-Kohn-Rostoker (KKR) [11]. Nos calculs ont reproduit les tendances expérimentales en fonction de la relaxation, en particulier les valeurs géantes de la précession de spin autour de 7,8 eV pour un film bien rélaxé (cf. Fig. 2 (droite)), qui coincide avec la structure qu'on trouve dans les expériences à 7,4 eV. Fait intéressant, les calculs effectués sur fcc-Co(001), bcc-Co(001) et bcc-Ni(001) prédisent un comportement similaire.

Dans la deuxième partie de ma thèse on a étudié l'effet de la relaxation de surface sur le mouvement du spin d'électrons dans le système MgO/Fe. Une analyse par diffraction des rayons X de l'interface MgO/Fe(001) a montré que déjà une couverture d'une sous-monocouche de MgO est capable d'induire une relaxation importante de la couche de surface de Fe [12].

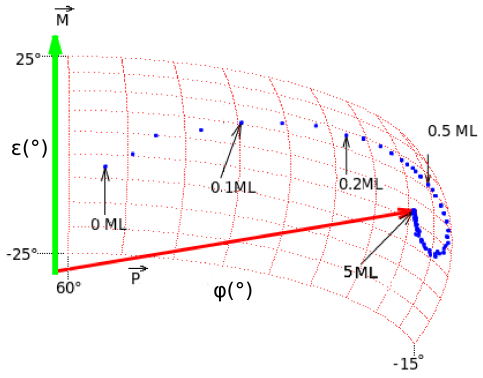

Figure 3: Les angles de mouvement de spin dans Fe(001) sont très sensibles à une variation de l'épaisseur de MgO.

Dans les expériences que nous avons réalisés, les angles de mouvement de spin ont été étudiés en fonction de l'épaisseur de MgO. Une sensibilité très forte de ε et ϕ à la couverture avec MgO est observée pour certaines

gammes d'énergie (Fig. 3). Un changement du magnétisme de la surface de Fe pendant le dépôt de MgO est exclu comme origine de ces variations par des mesures magnéto-optique d'effet Kerr. La relaxation hors-plan de la surface de Fe lors du dépôt de MgO est peut être responsable de ce comportement. Pour vérifier cette hypothèse, nous avons effectué des calculs *ab initio* pour différents degrés de relaxation entre le prémier plan (la surface) et le deuxième plan du film de Fe. Bien que les valeurs calculés diffèrent significativement de celles trouvées expérimentalement à certaines énergies, les structures globales ainsi que la tendance en fonction de l'épaisseur de MgO sont reproduits. En résumé, les calculs montrent que la relaxation inter-plan induite dans le film de Fe par la présence de MgO est responsable du comportement observé dans notre expérience.

Apart ces études concernants le comportement des électrons au-dessus de l'énergie de vide, l'effet d'une relaxation structurale sur la magnétorésistance tunnel de la jonction tunnel magnétique Fe/MgO/Fe a été étudié. Les calculs montrent également un comportement assez sensible des propriétés électronique à la relaxation structurale.

En conclusion, des mesures de réflexion d'électrons dépendante de spin et des calculs *ab initio* montrent que la direction de la polarisation de spin des électrons réfléchis est sensible aux petites variations de la relaxation structurale.

Acknowledgement

I would like to express my gratitude to all those who gave me the possibility to complete this thesis.

I am deeply indebted to my supervisor Prof. Dr. W. Weber whose stimulating suggestions and encouragement helped me all over the period of my thesis. Thank you for offering this valuable chance to perform my PhD studies under your worthful and precious supervision. Thank you for your efforts, scientific instructions and discussions that you provided me with, in order to achieve my Thesis.

I am also grateful to Prof. Mébarek Alouani who supervised my theoretical work. Thank you a lot for the time, worthful discussions and encouragement you provided me in order to achieve this thesis. You were the unofficial director of my thesis. I would like also to address my thanks to Prof. Jurgan Henk for providing us with the numerical code omni2K. I am also thankful to Dr. Haitham Zaraket who introduced me to the field of research.

I have furthermore to thank the members of the jury Prof. Hubert Ebert, Dr. Yves Lassailly, and Prof. Hugues Dreysse who accepted to review this work. I want also to thank the director of the Institut de physique et Chimie des Matériaux de Strasbourg who gave me the permission to perform this work in this institute. I'm also thankful to the staff of the institute especially the Surfaces and Interfaces department for their help in accomplishing this thesis.

Thanks to all my coworkers whom I enjoyed working with. Thank you Dr. Logane Tati Bismaths, Dr. Thibaut Berdot, Dr. Puja Dey, Mohmad Hamieh, and Fatima Djeghloul. Thanks to all my office colleagues who provided a comfortable environment. Dr. Saqib Javaid, Filip Schleicher, Dr. J.-B. Beaufrand.

Special thanks to every one of my friends for the good moments that we shared together. Hasan kesserwan, Hussein Hijazei, Mouhammad khalil, Ali Jaafar, Mohammad Haidar, Jamal mohamad and his wife Rania, Abed Ghaddar,Ali Hamieh, Hussein Ftoni, Wassim Jaber, Mouhammad Mokadam, Ahmed Maghraoui and Ferdaous Ben Romdhane ....Thank you all.

I would like to thank my parents whose presence during my defence meant a lot to me. Thank you for supporting and encouraging me during all these years no matter what I say I can not thank you enough.

A deep thank you from my heart to the one who stood next to me and supported me in the happy and sad moments a simple thank you is not enough... Love you Fatima.

Finally, a special thank you to sir Abu Saleh and I hope to see him soon.

Contents

List of Figures

Chapter 1

Introduction

The interfacial structure between a magnetic/non-magnetic film plays a crucial role in spintronic devices. In this sense, a number of experimental and theoretical works were devoted to investigate the influence of the interfacial structure on tunneling magnetoresistance (TMR), namely in Fe/MgO/Fe magnetic tunnel junctions (MTJ). However, most of these researches concentrated on the effect of disorder, oxidation, or oxygen and MgO vacancies [1, 2, 4, 3]. On the other hand, there are very few reports on the relation between the lattice relaxation and the spin-dependent transmission or reflection amplitude [5, 6]. These studies show possible ways to enhance the magnetoresistance effect by controlling the interfacial structure. In order to exploit it in a controlled manner, a better understanding of this effect is required. In the attempt to

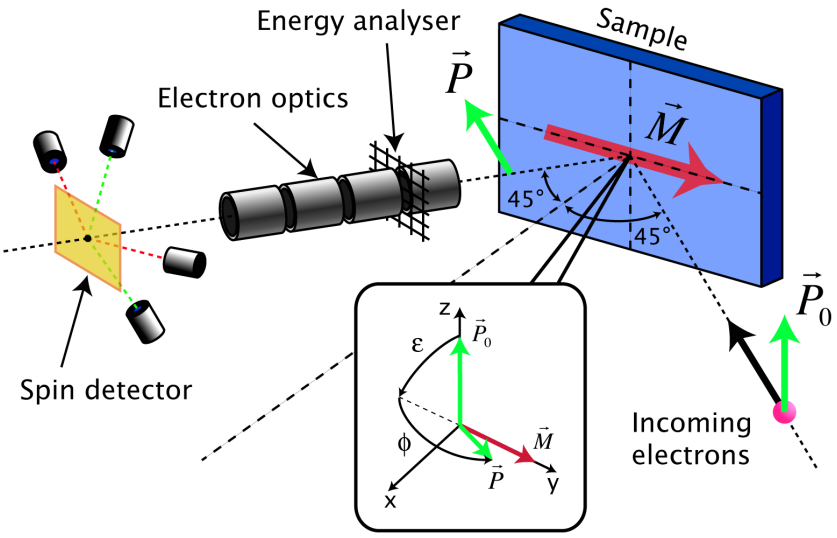

Figure 1.1: Spin-polarized electron reflection experiment, consisting of a spin-polarized electron source, a remanently magnetized sample, a retardation grid for the energy analysis, and a spin detection system. The two types of spin motion, i. e. the precession ε and the rotation ϕ, are defined in the inset.

unravel the interfacial spin-dependent properties, experiments in which the

spin polarization of the electrons is measured before and after the interaction with a ferromagnetic film are performed. In such experiments, an incident spin-polarized electron beam, whose polarization $\mathbf{P_0}$ being perpendicular to the magnetization $\mathbf{M}$ of the film, will exhibit two kinds of spin motions upon its reflection from the ferromagnetic film [7, 8], namely a precession of the polarization $\mathbf{P}$ around $\mathbf{M}$ by an angle ε and a rotation by an angle ϕ in the plane spanned by $\mathbf{P}$ and $\mathbf{M}$ (see inset in Fig. 1.1).

Fig. 1.1 shows the schematics of the experimental set-up, which consists of a spin-polarized electron source, a ferromagnetic film which is magnetized remanently in-plane by a magnetic field pulse, and a spin detector. The 70 % polarized electron beam is obtained from a GaAs-type source by optically pumping the crystal with circularly polarized light. The beam is incident at 45° with respect to the sample's surface. To observe a maximum spin motion, $\mathbf{P_0}$ has to be oriented perpendicularly with respect to $\mathbf{M}$ of the film. The spin polarization of the elastically scattered electrons, to which I restricted my study, is finally measured by a spin detector.

In the first part of my thesis, I studied the electron spin motion in reflection from a thin ferromagnetic Fe film during growth on Ag(001). As the bulk lattice parameters of Fe and Ag are different a strain is induced in the Fe film during growth. Above a critical thickness this strain is successively relieved by the creation of interfacial dislocations in the film [9]. Hence, the lattice parameter of the film is expected to vary over a wide range of thickness.

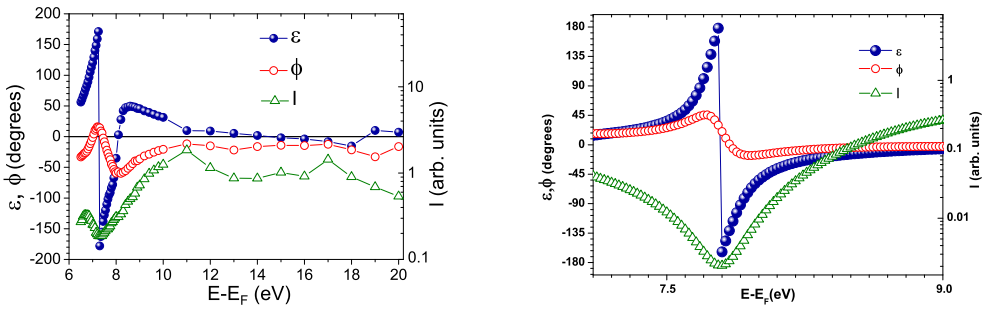

Figure 1.2: Left: Spin-integrated electron reflectivity I, precession angle ε and rotation angle ϕ as a function of the primary electron energy $E - E_F$ for a 4.6 nm thick Fe film after annealing at 420 K. Right: Calculated Precession angle ε, reflecetion Intensity I, and rotation angle ϕ versus primary electron energy $E - E_F$ for non strained Fe structure.

My experiments on Fe films deposited on Ag(001) showed that the spin precession angle in reflection can reach its maximum possible value, namely 180° (cf. Fig. 1.2 (left)). This marks the ultimate limit of spin manipulation in reflection. Such large values have not been realized before, even in transmission experiments in which the precession angle increases linearly with the thickness of the ferromagnetic layer. Most importantly, the observation of this 180° spin precession seems to be very sensitive to the relaxation of the Fe film during its growth. In fact, annealing of the Fe film, which is known to promote strain relaxation, is necessary to obtain this giant precession value. In order to verify the effect of lattice relaxation on the spin precession, spin-dependent low-energy electron diffraction calculations have been performed for different degrees of lattice relaxations. The electronic band structure is calculated using a linear orbital muffin-tin approximation (LMTO) [10], which provides a converged potential to compute the spin polarized low-energy electron diffraction (SPLEED) by means of the layer Korringa-Kohn-Rostoker method [11].

The calculations clearly reproduce the experimental trends, especially the giant spin precession structure around 7.8 eV (cf. Fig. 1.2 (right)) which coincides with its experimental counter part at 7.4 eV. For large lattice strain, both experiment and theory show small precession values. As the strain decreases the precession angle increases and reaches finally 180°. Interestingly, calculations performed on fcc-Co(001), bcc-Co(001), and bcc-Ni(001), predict a similar behavior.

In the second part, I investigated the effect of surface relaxation in the system MgO/Fe on the electron-spin motion. An X-ray diffraction analysis of the MgO/Fe(001) interface showed that already sub-monolayer coverages of MgO are able to induce a significant relaxation of the Fe surface layer [12], where the out-of-plane lattice relaxation increases up to 18% of its bulk value due to formation of Fe-O bonds. In my experiments, the spin motion angles were studied as a function of the MgO coverage. A very strong sensitivity of the spin-motion angles, ε and ϕ, to the MgO coverage is observed for certain energy ranges (cf. Fig. 1.3). From magneto-optical Kerr effect measurements, any possible strong change of the Fe surface magnetism during MgO deposition is excluded to be the origin of these dramatic variations of the spin-motion angles. The drastic out-of-plane relaxation of the Fe surface during deposition of MgO is believed to be responsible for this behavior.

To verify these experimental observations, *ab initio* electronic band struc-

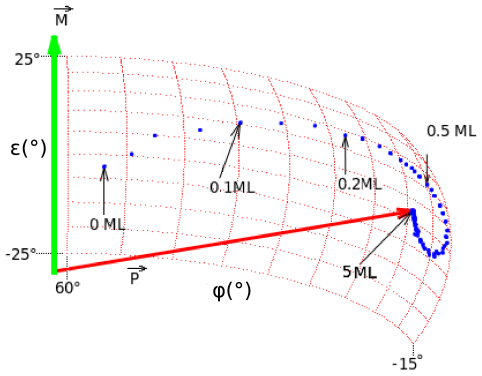

Figure 1.3: The spin motion angles in Fe (001) are very sensitive to sub-monolayer coverages of MgO.

ture calculations have been performed for different degrees of out-of-plane relaxations. Since very small amounts of MgO are already able to introduce a significant effect, the calculations were done by just considering a relaxation of the last Fe layer, without actually "putting" MgO on top of the Fe layer. An increase in relaxation, i.e. the first Fe interlayer distance is increasing, corresponds to an increase in MgO coverage. Although the absolute values in the calculations differ quite significantly from the experimental ones at certain energies, the global structures as well as the tendency for increasing MgO coverage are reproduced. In summary, our calculated precession and rotation angles at low kinetic energies show that the MgO-induced relaxation of the Fe surface plane is indeed responsible for this behavior.

In the third part of my thesis, I investigated theoretically the effect of structural relaxation on the transport properties in Fe/MgO/Fe magnetic tunnel junction (MTJ). The transmission values of Fe/MgO/Fe tunnel junctions were calculated within an *ab-initio* electronic transport code based on a combination of Density Functional Theory (DFT) and Non-Equilibrium Green's function transport methods (NEGF) SMEGOL (Spin and Molecular Electronics in Atomically-Generated Orbital Landscapes). The Kohn-Sham equations are solved in the NEGF scheme and the current is then obtained from the Landauer formula.

The transport properties of Fe/MgO/Fe MTJs are studied as a function of the Fe-Fe interlayer distances near the interface. The conductance coefficients were calculated for different degree of relaxation. First, both interfaces where relaxed (symmetric structure) by varying the out-of-plane relaxation at the

interface. Second, only one interface is relaxed (asymmetric structure). The behavior of the TMR as function of the relaxation depends on whether the structure is symmetric or not, and whether the interface is oxidized or not. In general, the TMR is largely reduced for asymmetric relaxation bringing the theoretical TMR closer to their experimental counter part. This reduction might explain the limitation observed in the experimental studies [13], where no values above 250% have been observed in such a system.

In conclusion, spin-dependent electron reflection measurements and *ab initio* calculations on ferromagnetic materials show that the spin polarization direction of the reflected electrons is very sensitive to small variations of the lattice relaxation. This points out the possibility of modulating the electron spin dependent transmission/reflection amplitudes and the spin motion by changing the interfacial structure in MTJ or by developing a strain in the ferromagnetic film.

Part I

Electron-spin motion: Concept and experiment

Chapter 2

Spin and Electron-spin motion

Contents

This chapter is devoted to give a brief history of the origin of the electron spin and to recall basic spin and spin polarization notations. We then end with a brief description of the electron spin-motion, which is the subject of this thesis.

2.1 Electron spin

2.1.1 Stern-Gerlach experiment

An experiment of atom's deflection named after Otto Stern and Walther Gerlach [15] performed in Frankfurt,Germany in 1920, was the first experiment to show the existence of an intrinsic property of the electron called spin. Although their experimental result was not used to proof the existence of the electron spin, nowadays it is widely used to illustrate the existence of the spin and its quantization properties. Stern and Gerlach directed a silver beam

through an inhomogeneous magnetic field, then the beam hits a screen showing how the Ag atoms are deflected after interacting with the inhomogeneous magnetic field (cf. Figure 2.1). In order to suppress the effect of the Lorentz force, the silver beam was neutrally charged in the experiment.

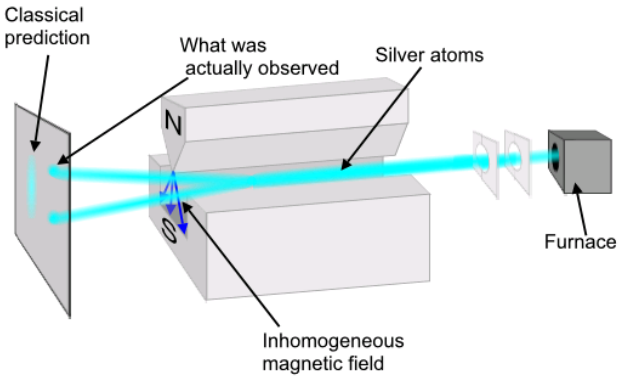

Figure 2.1: Schematics of the Stern-Gerlach experiment.

Classically, the Ag atom is considered as a spinning magnetic dipole, where in the presence of a homogeneous magnetic field it will precess due to the torque exerted by the magnetic field on it. If the magnetic field is inhomogeneous, the dipole traversing the magnetic field will be deflected depending on its orientation. According to the dipole- magnetic field interaction: $\boldsymbol{F} = \boldsymbol{\nabla}(\boldsymbol{m}.\boldsymbol{H})$, where $\boldsymbol{m}$ is the dipole and $\boldsymbol{H}$ is the inhomogeneous magnetic field, one expects to see on the screen a smooth distribution of the Ag atoms.

While Bohr and Sommerfeld [17] predicted that an atom of angular moment $l = 1$ would have a quantized magnetic moment with the same size but of opposite directions, the aim of the Stern-Gerlach experiment was to test the validity of this hypothesis [16]. Their result confirmed the Bohr-Sommerfeld hypothesis as they observed two spots on the detector screen corresponding to two opposite magnetic moments. Later in 1927, a similar experiment using hydrogen atoms with $l = 0$ reproduced the two spots [18], which posed a problem to the Bohr-Sommerfeld hypothesis. The interpretation of the Stern-Gerlach experiment is nowadays referred to the electrons having a magnetic moment called spin.

However, the concept of electron spin was first proposed in 1925 by Goudsmit and Uhlenbeck [19] in order to explain the fine-structures in the atomic spectra in the presence of an external magnetic field known as Zee-

man effect. While the quantum mechanics with three quantum numbers n,l, and m could not explain the fine-structures, a fourth quantum number was needed. Goudsmit and Uhlenbeck suggested the idea of a spinning electron which gives rise to an intrinsic angular momentum in addition to the orbital angular momentum.

2.1.2 Dirac equation

The result of the Stern-Gerlach experiment posed a problem to Schrödinger's equation which did not include the notation of electron spin. In order to solve this problem Pauli had to introduce the spin formalism into Schrödinger's equation by hand using what is called the three Pauli spin matrices:

$$\sigma_x = \begin{pmatrix} 0 & 1 \\ 1 & 0 \end{pmatrix}; \sigma_y = \begin{pmatrix} 0 & -i \\ i & 0 \end{pmatrix}; \sigma_z = \begin{pmatrix} 1 & 0 \\ 0 & -1 \end{pmatrix}. \tag{2.1}$$

Later in 1928, Paul Dirac came with a relativistic quantum equation which provided a description of the elementary spin-$\frac{1}{2}$ as an intrinsic property of the electron.

The Dirac equation for a free electron is defined as follows

$$\left(\beta mc^2 + \sum_{k=1}^{3} \alpha_k p_k c\right) \psi(x,t) = i\hbar \frac{\partial \psi(x,t)}{\partial t}, \tag{2.2}$$

where m is the rest mass of the electron, c the speed of light, p the momentum operator, x and t are the space and time coordinates, respectively, $\hbar$ is the reduced Planck's constant, ψ is the wave function of the electron, with α_k and β are 4×4 matrices, such that:

$$\alpha_x = \begin{pmatrix} 0 & 0 & 0 & 1 \\ 0 & 0 & 1 & 0 \\ 0 & 1 & 0 & 0 \\ 1 & 0 & 0 & 0 \end{pmatrix}; \alpha_y = \begin{pmatrix} 0 & 0 & 0 & -i \\ 0 & 0 & i & 0 \\ 0 & -i & 0 & 0 \\ i & 0 & 0 & 0 \end{pmatrix}; \alpha_z = \begin{pmatrix} 0 & 0 & 1 & 0 \\ 0 & 0 & 0 & -1 \\ 1 & 0 & 0 & 0 \\ 0 & -1 & 0 & 0 \end{pmatrix}. \tag{2.3}$$

$$\beta = \begin{pmatrix} 1 & 0 & 0 & 0 \\ 0 & 1 & 0 & 0 \\ 0 & 0 & -1 & 0 \\ 0 & 0 & 0 & -1 \end{pmatrix}. \tag{2.4}$$

One might use the quantum field theory units by taking $c = \hbar = 1$, so that the Dirac equation can be written as:

$$(-i\boldsymbol{\alpha}.\boldsymbol{\nabla} + \beta m)\,\psi = i\frac{\partial \psi}{\partial t}. \tag{2.5}$$

It is obvious that:

$$\boldsymbol{\alpha} = \begin{bmatrix} 0 & \boldsymbol{\sigma} \\ \boldsymbol{\sigma} & 0 \end{bmatrix}; \beta = \begin{bmatrix} \mathbf{I} & 0 \\ 0 & -\mathbf{I} \end{bmatrix}, \tag{2.6}$$

where $\mathbf{I}$ and $\boldsymbol{\sigma}$ are the unitary and Pauli 2×2 matrices, respectively. Consequently the solution of the Dirac equation for a free electron can be written in the following form:

$$\psi = we^{-ip.x}, \tag{2.7}$$

where w is defined as the Dirac spinor

$$w = \begin{bmatrix} \chi \\ \phi \end{bmatrix}. \tag{2.8}$$

Introducing the plane wave solution into the free electron Dirac equation results in:

$$E \begin{bmatrix} \chi \\ \phi \end{bmatrix} = \begin{bmatrix} m\mathbf{I} & \boldsymbol{\sigma}.\boldsymbol{p} \\ \boldsymbol{\sigma}.\boldsymbol{p} & -m\mathbf{I} \end{bmatrix} \begin{bmatrix} \chi \\ \phi \end{bmatrix}. \tag{2.9}$$

The solutions of the two coupled equations $(E - m)\,\chi = (\boldsymbol{\sigma}.\boldsymbol{p})\phi$ and $(E + m)\,\phi = (\boldsymbol{\sigma}.\boldsymbol{p})\chi$ are:

$$w_1 = \begin{bmatrix} \chi \\ \phi \end{bmatrix} = \begin{bmatrix} \chi \\ \frac{\boldsymbol{\sigma}.\boldsymbol{p}}{E+m}\chi \end{bmatrix}; w_2 = \begin{bmatrix} \chi \\ \phi \end{bmatrix} = \begin{bmatrix} -\frac{\boldsymbol{\sigma}.\boldsymbol{p}}{E+m}\phi \\ \phi \end{bmatrix}. \tag{2.10}$$

One of the above solutions describes a free electron while the other a free positron. Since we are dealing only with electrons in this thesis, we will consider only the first case with a positive energy. Thus the convenient definitions of χ spinors are:

$$\chi^1 = \begin{pmatrix} 1 \\ 0 \end{pmatrix}; \chi^2 = \begin{pmatrix} 0 \\ 1 \end{pmatrix}. \tag{2.11}$$

The two $\chi^{(s)}$ spinors represent the electron spin states up $|\uparrow\rangle$ and down $|\downarrow\rangle$; $s = 1$ for up and $s = 2$ for down. It turns out that the orbital angular momentum does not commute with the Hamiltonian of the Dirac equation:

$$[H, l] = \boldsymbol{\sigma} \times \boldsymbol{\nabla}. \tag{2.12}$$

Physically this means that the orbital angular momentum is not a constant of motion. In order not to violate the total angular momentum conservation law, l must be replaced by another operator which commutes with H. One way to do that is to find an operator whose commutator with H is opposite to that of $[H, l]$. This operator turns out to be nothing else than the spin operator :

$$[H, S] = -\boldsymbol{\sigma} \times \boldsymbol{\nabla}, \tag{2.13}$$

with

$$\boldsymbol{S} = \frac{\hbar}{2}\boldsymbol{\sigma}, \tag{2.14}$$

where $\boldsymbol{\sigma}$ is the generalized Pauli matrix. It is obvious that the Dirac equation defines the spin as an intrinsic property of the electron even for the non-free electron Dirac equation. From the previous equations one can easily prove the following properties of the S operator:

$$\begin{cases} \boldsymbol{S}^2|\uparrow\rangle &= \frac{3}{4}\hbar^2|\uparrow\rangle \\ \boldsymbol{S}^2|\downarrow\rangle &= \frac{3}{4}\hbar^2|\downarrow\rangle \\ \boldsymbol{S}_z|\uparrow\rangle &= +\frac{1}{2}\hbar|\uparrow\rangle \\ \boldsymbol{S}_z|\downarrow\rangle &= -\frac{1}{2}\hbar|\uparrow\rangle, \end{cases} \tag{2.15}$$

with

$$\begin{cases} \langle\uparrow|\downarrow\rangle &= 0 \\ \langle\uparrow|\uparrow\rangle &= \langle\downarrow|\downarrow\rangle = 1. \end{cases} \tag{2.16}$$

2.2 Spin polarization

2.2.1 Pure spin state

An ensemble of electrons is said to be polarized if the electron spins have a preferential orientation. In this case the electron spin can be described by a single spin function called pure state $\chi = \binom{a_1}{a_2} = a_1|\uparrow\rangle + a_2|\downarrow\rangle$, which represents all the spins oriented in the same direction $\boldsymbol{e}(\theta, \varphi)$ (cf. Figure 2.2) with $a_1 = \cos\frac{\theta}{2}$ and $a_2 = \cos\frac{\varphi}{2}$.

In the pure spin state χ, the components of the polarization vector are given by the expectation values of the Pauli spin operators $\boldsymbol{\sigma} = \frac{2}{\hbar}\boldsymbol{S}$:

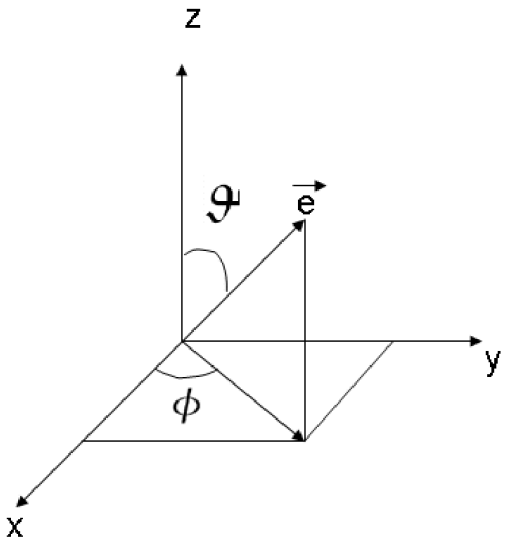

Figure 2.2: Direction of spin.

$$\boldsymbol{P} = \frac{\langle\chi|\boldsymbol{\sigma}|\chi\rangle}{\langle\chi|\chi\rangle}. \tag{2.17}$$

Thus, the three components of the spin polarization vector are:

$$P_x = a_1^* a_2 + a_2^* a_1 = \sin\theta\cos\varphi \tag{2.18}$$

$$P_y = i(a_2^* a_1 - a_1^* a_2) = \sin\theta\sin\varphi \tag{2.19}$$

$$P_z = |a_1|^2 - |a_2|^2 = \cos\theta. \tag{2.20}$$

Since we assumed that all electron spins can be described by a single spin function (pure state), the polarization vector has the direction of $\boldsymbol{e}$, having a degree of polarization $P = \sqrt{P_x^2 + P_y^2 + P_z^2}$ that equals to one.

2.2.2 Partially polarized electron beam

Up to now only totally polarized electron beams were considered, i.e. all electrons of the beam are in the same spin state. In this part we will consider a partially polarized beam, which represents a statistical mixture of different spin states. Thus the polarization of the total system is just the average of the polarization vector of the individual systems which are in pure spin states:

$$\boldsymbol{P} = \sum_i w^{(i)} \boldsymbol{P}^{(i)} = \sum_i w^{(i)} \frac{\langle \chi^{(i)} | \boldsymbol{\sigma} | \chi^{(i)} \rangle}{\langle \chi^{(i)} | \chi^{(i)} \rangle}, \tag{2.21}$$

where $w^{(i)}$ is a weighting factor that takes into account the relative proportion of the pure spin state $\chi^{(i)}$. With $N^{(i)}$ the number of electrons being in the pure spin state $\chi^{(i)}$, we obtain:

$$w(i) = \frac{N^{(i)}}{\sum_i N^{(i)}}. \tag{2.22}$$

For simplicity we take the direction of polarization along the z direction. In this case the polarization is given by $P = \frac{N_\uparrow - N_\downarrow}{N_\uparrow + N_\downarrow}$, where $N_\uparrow$ and $N_\downarrow$ are the numbers of electrons having a spin value of $\hbar/2$ and $-\hbar/2$, respectively.

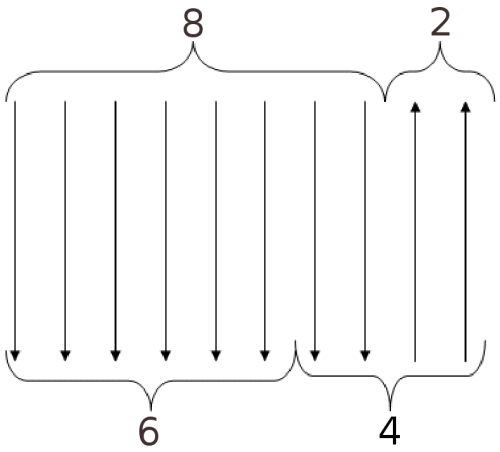

Figure 2.3: Partially polarized beam.

2.2.3 Density matrix

Usually the density matrix ϱ is a useful tool for describing a mixed state in quantum mechanics. Thus, it is possible to use ϱ to describe a mixed state in the partially spin-polarized electron beam [20, 30]. The general form of ϱ is:

$$\varrho = \sum_i w^i |\chi^i\rangle\langle\chi^i|. \tag{2.23}$$

In our case ϱ becomes :

$$\varrho = \sum_i w^i \begin{pmatrix} a_1^i \\ a_2^i \end{pmatrix} \begin{pmatrix} a_1^{i\,*} & a_2^{i\,*} \end{pmatrix} = \sum_i w^i \begin{pmatrix} |a_1^{i\,2}| & a_1^i a_2^{i\,*} \\ a_1^{i\,*} a_2^i & |a_2^{i\,2}| \end{pmatrix}. \tag{2.24}$$

From the above equation and from the set of equations (2.18-2.20) one can write:

$$\sum_i w^{(i)} a_1^{(i)} a_2^{(i)*} = \frac{1}{2}(P_x - iP_y) \tag{2.25}$$

$$\sum_i w^{(i)} a_1^{(i)*} a_2^{(i)} = \frac{1}{2}(P_x + iP_y). \tag{2.26}$$

Since $\sum_n w^{(i)} |a_1^{(i)}|^2$ resembles the probability to find the beam in the spin-up state, it can be expressed as $N_\uparrow/(N_\uparrow - N_\downarrow) = \frac{1}{2}(1 + P_z)$. Analogously, we find $\sum_i w^{(i)} |a_2^{(i)}|^2 = \frac{1}{2}(1 - P_z)$. Therefore, the density matrix can be written as:

$$\varrho = \frac{1}{2} \begin{pmatrix} 1 + P_z & P_x - iP_y \\ P_x + iP_y & 1 - P_z \end{pmatrix} = \frac{1}{2}(\mathbf{1} + \mathbf{P}.\boldsymbol{\sigma}). \tag{2.27}$$

Considering a polarization along the z direction, i.e. $P_x = P_y = 0$, the density matrix becomes:

$$\varrho = \frac{1}{2} \begin{pmatrix} 1 + P & 0 \\ 0 & 1 - P \end{pmatrix}. \tag{2.28}$$

For a totally polarized beam along the z-direction, the ϱ is written as follows:

$$\varrho_{\text{totpol}} = \begin{pmatrix} 1 & 0 \\ 0 & 0 \end{pmatrix}, \tag{2.29}$$

and for an unpolarized beam:

$$\varrho_{\text{unpol}} = \begin{pmatrix} \frac{1}{2} & 0 \\ 0 & \frac{1}{2} \end{pmatrix}. \tag{2.30}$$

Thus, a partially polarized beam can be expressed as [20]:

$$\varrho = \begin{pmatrix} 1 + P & 0 \\ 0 & 1 - P \end{pmatrix} = (1 - P)\varrho_{\text{unpol}} + P\varrho_{\text{totpol}}. \tag{2.31}$$

Finally, an electron beam with an arbitrary polarization can be considered to be made up of a totally polarized fraction and an unpolarized fraction which are mixed in the ratio $P/(1-P)$ (cf. Fig.2.3). For an ensemble of 100 electrons, that has 80 electrons with spin $+\hbar/2$ in the z direction and 20 with $-\hbar/2$ in the $-z$ direction, i.e. $N_\uparrow = 80$ and $N_\downarrow = 20$, one can say that 60 % of the beam is totally polarized while 40 % is unpolarized.

2.2.4 Tunnel magneto-resistance

In 1856, W. Thomson (Lord Kelvin) [21] was able to change the electrical resistance of ferromagnetic materials by applying an external magnetic field. He found that the resistance increases when the current and the applied magnetic field are in the same direction, while it decreases when they are perpendicular to each others. This dependency of the electric resistance on the magnetic field is known as the ordinary magneto-resistance (OMR). More recent researches discovered materials showing giant magneto-resistance (GMR) [22, 23], and tunnel magneto-resistance (TMR). In such materials the electrical resistance dependency on the magnetic field can reach high values that open wide possibilities for spintronic applications.

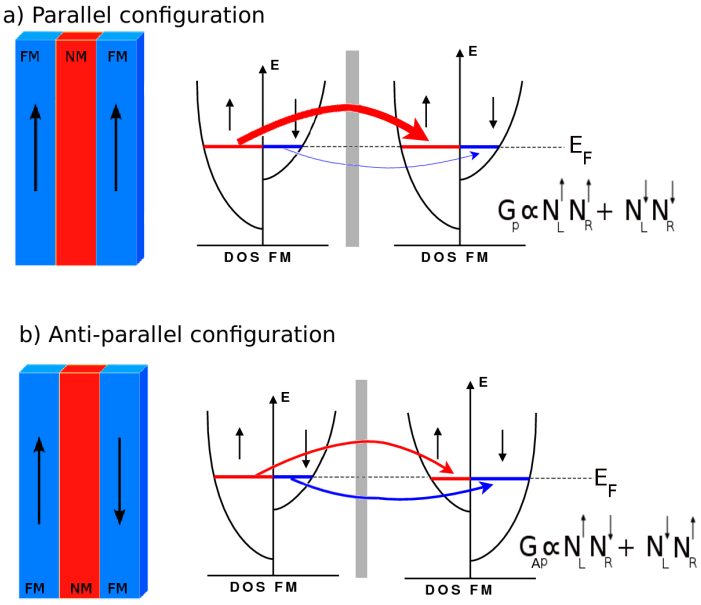

Figure 2.4: Schematic description of the TMR as explained by Julliere model.

TMR was first observed by Jullière in a Fe/Ge/Co junction in 1975 [24]. To explain his observation Jullière introduced a model which is based on two assumptions. First, he assumed that the electron-spin is conserved during the tunneling process. Thus tunneling of up- and down-spin electrons are considered to be independent of each other, so that the conductance occurs in two independent spin channels. According to this assumption, electrons from the first ferromagnetic film are accepted only by unfilled states of the same spin in the second film. So, in the case where the two ferromagnetic films are magnetized parallel, minority spin electron tunnel into minority states and majority spin electron tunnel into majority states. However, in the case where the two films are anti-parallel magnetized majority spin electron of the first film tunnel into minority states in the second film and vice versa. Second, Jullière assumed that the conductance (G) for a particular spin orientation (parallel: $\uparrow\uparrow$, anti-parallel: $\uparrow\downarrow$) is proportional to the product of the effective density of states (N) of the two ferromagnetic electrodes (left: L, right: R):

$$G^{\uparrow\uparrow} \propto N_L^{\uparrow} N_R^{\uparrow},\ G^{\downarrow\downarrow} \propto N_L^{\downarrow} N_R^{\downarrow},\ G^{\uparrow\downarrow} \propto N_L^{\uparrow} N_R^{\downarrow},\ G^{\downarrow\uparrow} \propto N_L^{\downarrow} N_R^{\uparrow}. \tag{2.32}$$

According to these two assumptions, and writing the TMR as the ratio of the change in conductance to the minimum conductance as follows :

$$TMR = \frac{G_p - G_{AP}}{G_{AP}}, \tag{2.33}$$

with $G_p = G^{\uparrow\uparrow} + G^{\downarrow\downarrow}$ and $G_{AP} = G^{\uparrow\downarrow} + G^{\downarrow\uparrow}$, one can define the polarization of the left and right electrodes by

$$P_{L,R} = \frac{N_{L,R}^{\uparrow} - N_{L,R}^{\downarrow}}{N_{L,R}^{\uparrow} + N_{L,R}^{\downarrow}} = \frac{\Delta N_{L,R}}{N_{L,R}}. \tag{2.34}$$

Thus the TMR can be written as:

$$TMR = \frac{2P_L P_R}{(1 - P_L P_R)}. \tag{2.35}$$

The Jullière model was used to estimate the magnitude of the TMR in magnetic tunnel junctions from the known values of the spin polarization of ferromagnets obtained in experiments with superconductors. Since the TMR is expressed in terms of the spin polarization, the Jullière formula is most convenient for comparing TMR values for systems with different electrodes but identical barriers.

A more convenient theoretical approach which can be used to estimate TMR in tunnel junctions was developed by Landauer [25]. In this approach the two leads are connected to two electron reservoirs and the current flow is viewed as a transmission process. In the case of a system with 2-D periodicity transverse to the direction of propagation, the Landauer formula can be written as:

$$G = \frac{2e^2}{h} \sum_{i,j} T_{i,j}(E_F). \tag{2.36}$$

where $T_{i,j}$ is the probability that an electron will be transmitted from the i^{th} state at the left of the sample to the j^{th} state at the right of the sample. This approach has proven to be extremely useful for calculating transport properties of molecular systems and nano-structured materials.

2.3 Electron-spin motion

While numerous studies have been done in the past on the reflection of spin-polarized electrons from ferromagnetic films [26, 27, 28], the spin-motion experiments that are presented in the following are distinguished by the fact that the spin polarization vector $\mathbf{P}_0$ of the incident electrons is perpendicularly oriented with respect to the magnetization vector $\mathbf{M}$ of the ferromagnet (cf. Fig. 2.5). It is only with this non-collinear initial configuration that the spin motion can be observed. In this particular spin configuration the spin can be considered as a coherent superposition of a majority-spin (with its magnetic moment parallel to $\mathbf{M}$) and a minority-spin state (with its magnetic moment anti-parallel to $\mathbf{M}$). These two spin states are represented by a (1,0) and a (0,1) spinor, respectively, and the initial spin configuration reads:

$$\chi_0 \sim \begin{pmatrix} 1 \\ 0 \end{pmatrix} + \begin{pmatrix} 0 \\ 1 \end{pmatrix}. \tag{2.37}$$

The two partial waves have an arbitrary but identical phase prior to the interaction with the ferromagnetic material. However, since the interaction is spin dependent, the amplitudes of the two spin wave functions are different after the interaction, and the total spin wave function will be:

$$\chi \sim |r^{\uparrow}|e^{i\theta^{\uparrow}} \begin{pmatrix} 1 \\ 0 \end{pmatrix} + |r^{\downarrow}|e^{i\theta^{\downarrow}} \begin{pmatrix} 0 \\ 1 \end{pmatrix}. \tag{2.38}$$

with $|r^{\uparrow,\downarrow}|$ the moduli of the spin-dependent reflection amplitudes and $\theta^{\uparrow,\downarrow}$ the corresponding phases. By taking into account the incomplete spin polarization $\mathbf{P}_0$ of the incident electron beam, the expectation values of the Pauli matrices

$$\sigma_x = \begin{pmatrix} 0 & 1 \\ 1 & 0 \end{pmatrix}, \sigma_y = \begin{pmatrix} 0 & -i \\ i & 0 \end{pmatrix}, \sigma_z = \begin{pmatrix} 1 & 0 \\ 0 & -1 \end{pmatrix}, \tag{2.39}$$

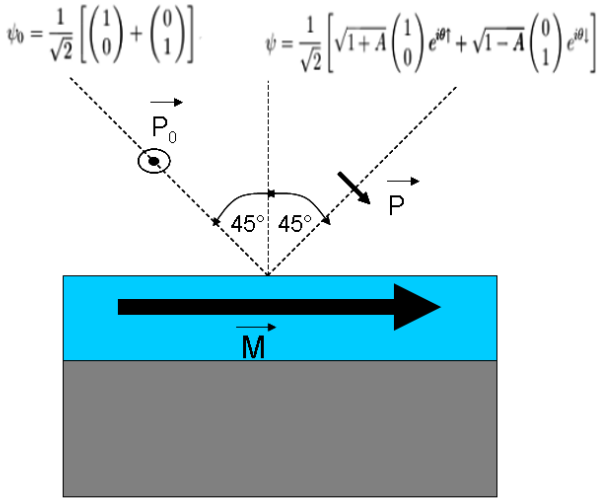

Figure 2.5: Incident electron beam with a polarization perpendicular to the magnetization of the ferromagnetic material. The spin wave function components become spin-dependent after reflection from the magnetic interface.

yield the spin polarization vector $\mathbf{P}$ of the electron beam after reflection. With the initial polarization $\mathbf{P}_0$ parallel to the x-axis and the magnetization $\mathbf{M}$ parallel to the z-axis we obtain:

$$\mathbf{P} = \frac{<\chi|\sigma|\chi>}{<\chi|\chi>} = \begin{pmatrix} P_0|r^{\uparrow}||r^{\downarrow}|\cos\left(\theta^{\downarrow}-\theta^{\uparrow}\right) \\ P_0|r^{\uparrow}||r^{\downarrow}|\sin\left(\theta^{\downarrow}-\theta^{\uparrow}\right) \\ \left(|r^{\uparrow}|^2-|r^{\downarrow}|^2\right)\left(|r^{\uparrow}|^2+|r^{\downarrow}|^2\right)^{-1} \end{pmatrix}. \tag{2.40}$$

By introducing the intensity asymmetry

$$A = \frac{|r^{\uparrow}|^2-|r^{\downarrow}|^2}{|r^{\uparrow}|^2+|r^{\downarrow}|^2} \tag{2.41}$$

and the angle

$$\varepsilon = \theta^{\downarrow}-\theta^{\uparrow} \tag{2.42}$$

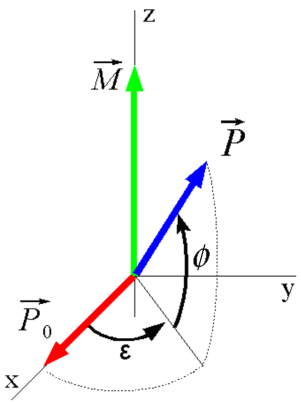

Figure 2.6: Illustration of the two types of motion of the spin polarization vector. The initial spin polarization $\mathbf{P}_0$ precesses around the magnetization $\mathbf{M}$ by an angle ε and rotates in the plane **P-M** by an angle ϕ.

the spin polarization vector becomes:

$$\mathbf{P} = \begin{pmatrix} P_0\sqrt{1-A^2}\cos\varepsilon \\ P_0\sqrt{1-A^2}\sin\varepsilon \\ A \end{pmatrix} \tag{2.43}$$

This corresponds to a precession of the polarization vector around the magnetization direction by an angle ε and a rotation by an angle ϕ in the plane spanned by $\mathbf{P}$ and $\mathbf{M}$ (cf. Fig. 2.6):

$$\phi = \arctan\left(\frac{A}{P_0\sqrt{1-A^2}}\right). \tag{2.44}$$

For experimental reasons it is more convenient to give the expression of the polarization vector after the interaction with the ferromagnet in another reference than that chosen in the previous paragraph. Drouhin and Rougemaille [31] found a compact expression that makes possible the calculation of the polarization of a beam of electrons after interaction for any direction of the incident polarization $\boldsymbol{P_0}$ and the magnetization $\boldsymbol{M}$:

$$\boldsymbol{P} = \frac{R_\varepsilon(\boldsymbol{u})\boldsymbol{P_0} + A\boldsymbol{u}}{1 + A\boldsymbol{u}.\boldsymbol{P_0}}, \tag{2.45}$$

where $\boldsymbol{u}$ is a unitary vector parallel to the magnetization direction and $R_\varepsilon(\boldsymbol{u})$ is the rotation matrix of an angle ε around the vector $\boldsymbol{u}$. For example, consider a vector $\boldsymbol{b} = \begin{pmatrix} x' \\ y' \\ z' \end{pmatrix}$ to be the image of a vector $\boldsymbol{a} = \begin{pmatrix} x \\ y \\ z \end{pmatrix}$ after rotation, the

Rodrigues formula for a rotation with an angle ε around the vector $\boldsymbol{u}$ is written as:

$$\begin{aligned} \boldsymbol{b} &= R_\varepsilon(\boldsymbol{u}).\boldsymbol{a} \\ R_\varepsilon(\boldsymbol{u}) &= \mathbb{I} + \sin\varepsilon[\boldsymbol{u}]_\times + (1-\cos\varepsilon)(\boldsymbol{u}\boldsymbol{u}^\intercal - \mathbb{I}), \end{aligned} \tag{2.46}$$

where $\mathbb{I}$ is the unitary matrix, and $[\boldsymbol{u}]_\times = \begin{bmatrix} 0 & -1 & 1 \\ 1 & 0 & -1 \\ -1 & 1 & 0 \end{bmatrix}$ is the cross product

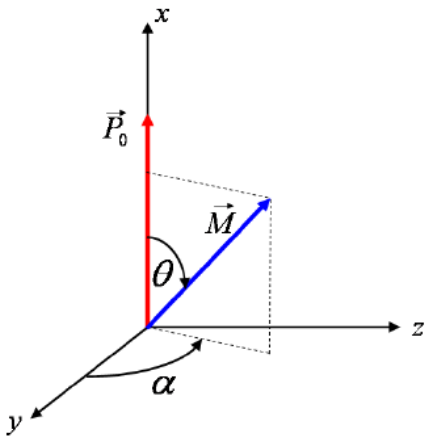

Figure 2.7: Definition of the angles α and θ.

matrix of $\boldsymbol{u}$. In our case, the components of the rotation matrix $R_\varepsilon(\boldsymbol{u})$ in the reference $\{x, y, z\}$ are:

$$\begin{cases} R_{1,1} = \sqrt{1-A^2}\cos\varepsilon + (1-\sqrt{1-A^2}\cos\varepsilon)\cos^2\theta \\ R_{1,2} = (1-\sqrt{1-A^2}\cos\varepsilon)\cos\alpha\sin\theta\cos\theta - \sqrt{1-A^2}\sin\alpha\sin\varepsilon \\ R_{1,3} = (1-\sqrt{1-A^2}\cos\varepsilon)\sin\alpha\sin\theta\cos\theta - \sqrt{1-A^2}\cos\alpha\sin\varepsilon \\ R_{2,1} = (1-\sqrt{1-A^2}\cos\varepsilon)\cos\alpha\sin\theta\cos\theta - \sqrt{1-A^2}\sin\alpha\sin\varepsilon\sin\theta \\ R_{2,2} = \sqrt{1-A^2}\cos\varepsilon + (1-\sqrt{1-A^2}\cos\varepsilon)\cos^2\theta\sin^2\theta \\ R_{2,3} = (1-\sqrt{1-A^2}\cos\varepsilon)\sin\alpha\cos\alpha\sin^2\theta - \sqrt{1-A^2}\sin\alpha\sin\varepsilon\cos\theta \\ R_{3,1} = (1-\sqrt{1-A^2}\cos\varepsilon)\sin\alpha\sin\theta\cos\theta - \sqrt{1-A^2}\sin\alpha\sin\varepsilon\sin\theta\cos\alpha \\ R_{3,2} = (1-\sqrt{1-A^2}\cos\varepsilon)\sin\alpha\cos\alpha + \sqrt{1-A^2}\sin\alpha\sin\varepsilon\cos\theta \\ R_{3,3} = \sqrt{1-A^2}\cos\varepsilon + (1-\sqrt{1-A^2}\cos\varepsilon)\sin^2\theta\sin^2\alpha, \end{cases} \tag{2.47}$$

with the angles α and θ defined in the figure 2.7. In the experiment the initial polarization is perpendicular to the magnetization and the incident electron

beam makes an angle of 45° with respect to the normal of the sample, thus $\theta = 90°$ and $\alpha = 45°$. According to this configuration the reflected polarization becomes:

$$\begin{cases} P_x = P_0\sqrt{1-A^2}\cos\varepsilon \\ P_y = \frac{1}{\sqrt{2}}\left(A + P_0\sqrt{1-A^2}\sin\varepsilon\right) \\ P_z = \frac{1}{\sqrt{2}}\left(A - P_0\sqrt{1-A^2}\sin\varepsilon\right) \end{cases} . \tag{2.48}$$

Chapter 3

Experimental Techniques

Contents

The experimental set-up is divided into three chambers separated by valves: the source chamber in which the source of polarized electrons is prepared, the main chamber in which the preparation of the ferromagnetic films and the measurements are done, and the spin-detector chamber. Figure 3.1 shows the schematics of the experiment.

3.1 Source chamber

In this chamber the pressure is maintained at 10^{-11} mbar using an ionic pomp. At this pressure the polarized electron source, which is a Zn-doped Gallium Arsenide (GaAs) crystal, is prepared.

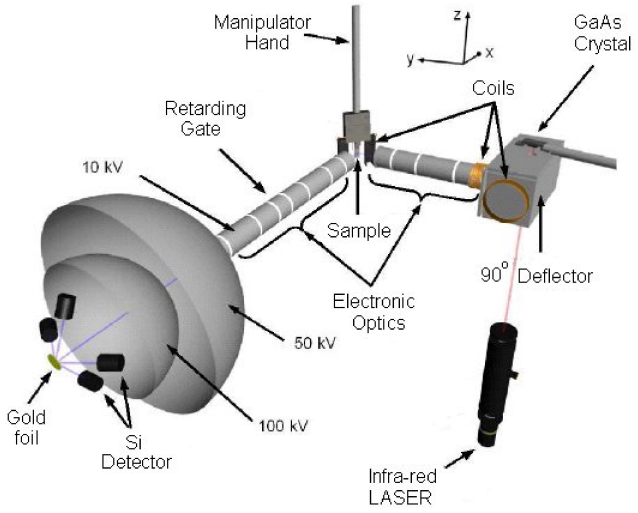

Figure 3.1: Schematics of the experiment.

3.1.1 GaAs as polarized electron source

Prior to each measurement, the source must be activated. In order to do so one must reduce the work function of the crystal to facilitate the emission of electrons (cf. Fig. 3.2) which becomes possible by depositing successive layers of cesium and oxygen on the surface of the GaAs crystal. Then the source is moved towards the main chamber where it is placed above the electron optics which lead the emitted electrons to the sample. If there is a good pressure in the main chamber the crystal remains active for a dozen of hours. A too high pressure, however, will lead to a contamination of the GaAs surface making the crystal unusable. After each use the crystal is heated to a temperature of about 500 °C in the source chamber to eliminate the cesium and oxygen deposited and any possible contamination. In this way the GaAs surface is regenerated, which can then be reactivated once again.

The activated GaAs photocathodes are widely used as sources of spin-polarized electrons for the study of magnetic materials and in high-energy physics. In order to obtain polarized electrons the GaAs crystal is excited by circularly polarized light with an energy equal to the GaAs band gap [32].

A beam of left circularly polarized light σ^+ (photons have a magnetic moment $m = +1$; solid line in figure 3.3) or of right circularly polarized light σ^- (photons have a magnetic moment $m = -1$; dotted line in figure

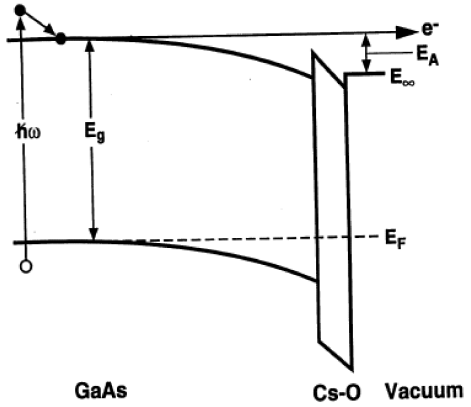

Figure 3.2: The decrease of the GaAs affinity after adding CsO.

3.3) is sent onto the activated GaAs crystal, which in its fundamental state consists of atoms in the state $P_{3/2}$ $(l = 1; j = 3/2; m_j = \pm 1/2, \pm 3/2)$ and $P_{1/2}$ $(l = 1; j = 1/2; m_j = \pm 1/2)$. The excitation of electrons being in the latter state, however, can be avoided by not exceeding the band gap energy of 1.42 eV. The selection rules require that $\Delta l = \pm 1$ and $\Delta m = \pm 1$, so that only two final states are possible: $S_{1/2}$ $(l = 0; j = 1/2; m_j \pm 1/2)$.

A light polarization σ^+ allows the following transitions: $m_j = -3/2 \rightarrow m_j = -1/2$ and $m_j = -1/2 \rightarrow m_j = 1/2$. A light polarization σ^-, on the other hand, allows: $m_j = 3/2 \rightarrow m_j = 1/2$ and $m_j = 1/2 \rightarrow m_j = -1/2$.

The transition probabilities related to the levels are calculated from the wave functions of the initial and final states and are indicated in the circles. With a light energy of 1.42 eV, i.e. avoiding the excitation of electrons in the state $P_{1/2}$, the theoretically expected degree of polarization is $P = \frac{3-1}{3+1} = 50\%$.

Experimentally, we reach approximately a polarization of 25 % . This is explained by the strong diffusion of the excited electrons before being ejected into the vacuum. As these diffusion processes are in general not spin conserving, the polarization of the emitted electrons must be smaller. We can, however, get very high degrees of polarization of about 80 % using crystals of GaAs with a constrained surface, causing a lifting of the degenerated $P_{3/2}$ levels.

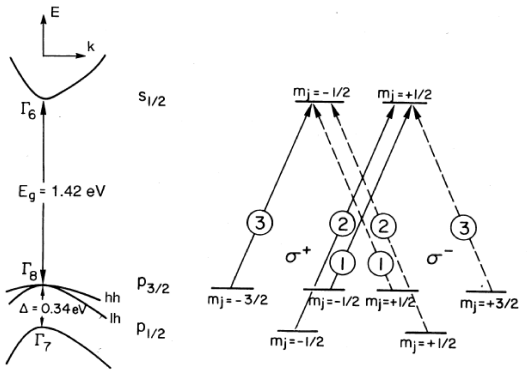

Figure 3.3: The electronic structure of GaAs.

3.2 Main chamber

Maintained at a pressure of 10^{-10} mbar by a primary pump, a turbomolecular pump and an ionic pump, the main chamber consists of several sub-systems.

3.2.1 Electron optics

The electron optics (cf. Fig. 3.4) is used to guide the emitted electrons from the GaAs source to the sample. It consists essentially of electrostatic elements. In this way the trajectory of the electrons can be changed without changing the direction of the electron spin. The first part consists of a Herzog plate (E_p) accelerating the electrons from the surface of the GaAs crystal to the 90 °-deflector (K_i and K_a). It provides a polarization perpendicular to the magnetization of the sample. At the deflector end, electrons are focused onto the sample with the aid of three electrostatic lenses (L1, L2 and L3). Finally, the electron beam has a diameter of about 1 mm when it reaches the surface of the sample. Coils are placed around the electron optics to compensate the influence of the Earth's magnetic field on the spin polarization direction.

3.2.2 Ion gun

Once a film is deposited and measured, an argon-ion gun can be used to etch these layers in order to be able to reuse the substrate again. Under a pressure of 3.10^{-6} mbar, an accelerating voltage of 1.5 kV and a sample current of 3 μA, it is possible to remove a dozen of nanometers in one hour.

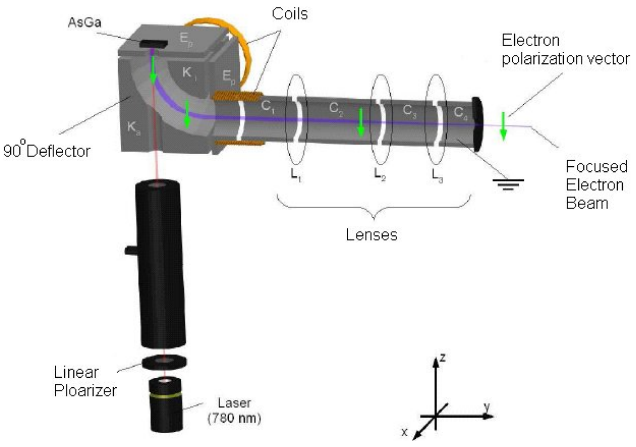

Figure 3.4: Electron optics guiding the electrons towards the sample.

3.2.3 Evaporators

The samples are prepared by evaporating pure elements or compositions on top of a substrate. For that we have used two types of evaporators at high voltage (cf. Fig. 3.5). For the deposition of MgO we used an evaporator which is composed of a filament and a crucible in which the MgO powder is placed. For Fe, on the other hand, the crucible is replaced by a rod of Fe.

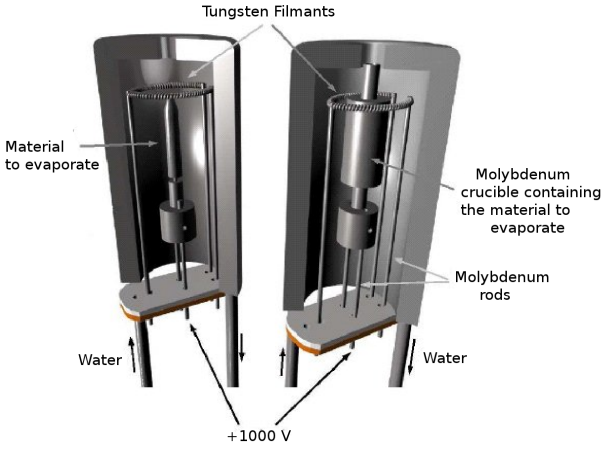

Figure 3.5: The two different types of evaporators used for the sample preparation.

The principle of evaporation is as follows: a current of about 3 A is sent through the filament, resulting in an emission of electrons due to the thermo-electric effect. These electrons are accelerated to the crucible or rod which

are kept at a positive potential of about 1000 V with respect to the filament. This leads finally to an increase in temperature of the material to evaporate.

3.2.4 Quartz microbalance

The flow of the evaporated material is calibrated by a quartz microbalance, being composed of a piezoelectric crystal that vibrates at a frequency of 5.9 MHz. During evaporation there is a mass change of the quartz due to the amount of deposited material, leading to a change of the eigen frequency of the quartz. As this change depends linearly on the deposited mass the deposition rate can easily be calculated.

3.2.5 LEED

In the case of mono-crystalline substrates, the crystal structure of the deposited film can be controlled by low-energy electron diffrection (LEED) (cf. Fig. 3.6).

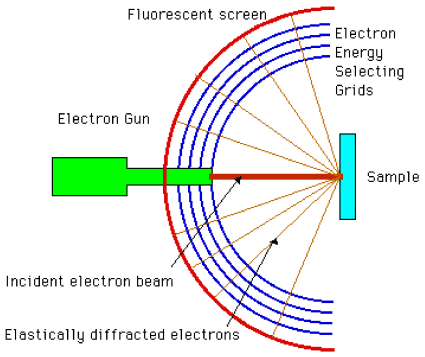

Figure 3.6: Schematics of LEED.

LEED is composed of an electron gun, a spherical phosphorescent screen and three concentric grids. The electron gun sends an electron beam to probe the surface with energies between 50 and several hundreds of eV. At these energies the mean free path of the electrons is only a few Angstroms, so that LEED is very surface sensitive. The two central grids, having a negative potential slightly below the elastic electron energy, stop electrons that have suffered inelastic scattering processes. The elastically diffracted electrons, on the other hand, can pass and are accelerated to a few keV so that they can

excite the phosphorescent screen. The diffraction diagram obtained in this way is the reciprocal network of the surface of the sample.

3.3 Spin detector

An argument originating from Bohr and Pauli shows that it is not possible to separate the two spin states of a free electron beam in the same way as silver atoms with different angular momenta in a Stern-Gerlach experiment. Thus, it is impossible to determine the spin polarization of a free electron beam in this way.

Another possibility for measuring the spin polarization of a free electron beam is the use of the spin-orbit interaction between the incident electrons and an atom which will scatter the electrons; an idea first suggested by Mott.

3.3.1 Principle of the Mott spin detector

The Mott spin detector consists of a thin gold foil (100 nm), which scatters the polarized electron beam at high energy (cf. Fig. 3.7). Gold has the advantage of having a high atomic number, i.e. it shows a strong spin-orbit coupling. The scattered electrons are detected by four semiconductor detector: Left, Right, Top, and Bottom detectors. The Left and Right determine the y-component of the polarization, whereas the Top and Bottom determine the z-component (cf. Fig. 3.7).

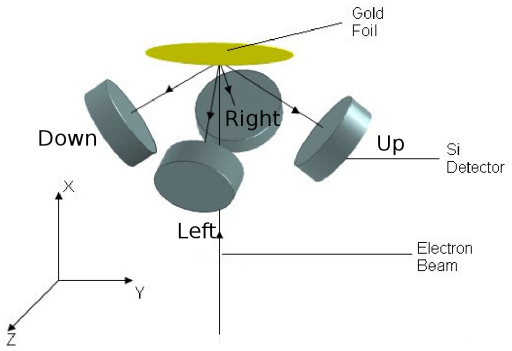

Figure 3.7: Schematics of the Mott spin detector.

In the rest frame of the incident electron, the gold atom moves towards

the electron. As a consequence, the electron "sees" a circular magnetic field the gradient of which exercises a force on the spin of the electron.

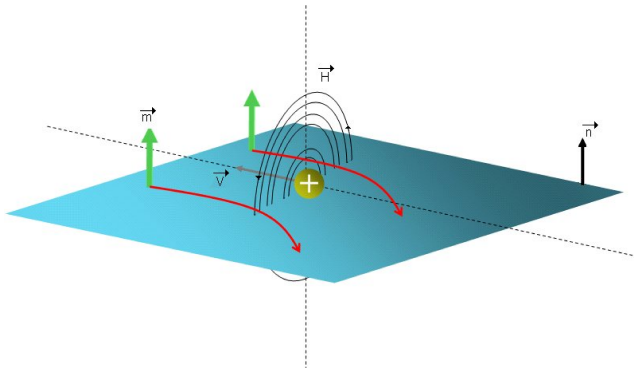

Figure 3.8: Scattering geometry in the Mott spin detector.

In the case of a spin "up" electron that passes to the right of the atom, the magnetic field and the magnetic moment are parallel and the force $\boldsymbol{F} = \boldsymbol{\nabla}(\boldsymbol{m}.\boldsymbol{H})$ pushes the electron towards increasing fields, i.e. towards the left. If the spin "up" electron passes to the left of the atom, the magnetic field and the magnetic moment are antiparallel and the force pushes the electron towards weaker fields, i.e. again towards the left. Thus, a spin "up" electron is scattered towards the left side with higher probability than towards the right side. The opposite is valid for a spin "down" electron. Thus, by counting the number of electrons $N_{r,l}$ scattered to the right and to the left, respectively, one will obtain the asymmetry term $A = \frac{N_r - N_l}{N_r + N_l}$, which is proportional to the component P_y of the electron beam polarization $\boldsymbol{P}$ in the direction $\boldsymbol{n}$ normal to the scattering plane.

In practice, however, even if $P_y = 0$, the asymmetry is not zero. An experimental set-up as shown in figure 3.7 usually possesses an instrumental asymmetry which results from the different efficiencies of the detectors on the left and on the right and from a possible misalignment of the incident electron beam. In order to eliminate this artificial asymmetry, we measure not only the scattered intensities when the incident polarization is $\boldsymbol{P}$ but also when it is $-\boldsymbol{P}$. In this way we obtain four intensities. For a polarization $\boldsymbol{P}$ we have:

$$N_l^+ = nNE_1\Omega_1 I(\theta)[1 + PS(\theta)] \quad (3.1)$$

$$N_r^+ = nNE_2\Omega_2 I(\theta)[1 - PS(\theta)], \quad (3.2)$$

with n the number of incident particles, N the number of target atoms per unit area, $\Omega_{1,2}$ and $E_{1,2}$ the solid angles and the detector efficiencies for the left and right detectors, respectively, θ is the angle of deviation of the electrons due to the gold foil, I the mean probability distribution of the process, and S the Sherman function of the spin detector.

For a polarization $-\boldsymbol{P}$ we have:

$$N_l^- = n'N'E_1\Omega_1 I(\theta)[1 - PS(\theta)] \quad (3.3)$$

$$N_r^- = n'N'E_2\Omega_2 I(\theta)[1 + PS(\theta)], \quad (3.4)$$

where the primes indicate that the number of incident electrons and the effective target thickness can be different.

By defining $N^+ = \sqrt{N_l^+ N_r^-}$ and $N^- = \sqrt{N_l^+ N_r^-}$, one obtains the real asymmetry $A = \frac{N^+ - N^-}{N^+ + N^-} = PS$ independent of the detector efficiencies $\Omega_{1,2}$. In our experiment S is about 0.2 .

3.4 Measurements

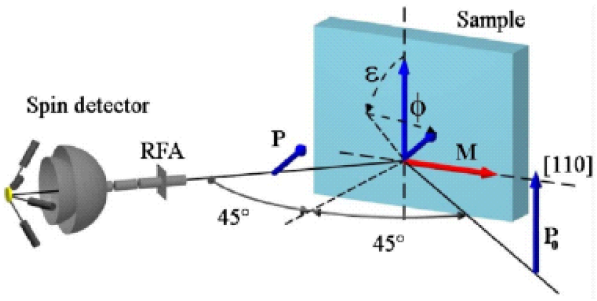

Figure 3.9: Scheme of the experiment, which consists of a polarized electron beam, an in-plane remanently magnetized ferromagnetic film, a retarding field energy analyzer, and a spin detector.

The incident spin-polarized electron beam hits the sample under an angle of 45 ° with respect to the normal of the sample surface. The reflected electrons are then energy-analyzed by a retarding field energy analyzer. Since the analysis of secondary electrons, which do not show a spin motion, is not useful in our experiment, the analyzer is set to let pass only elastically scattered

electrons. The elastic electrons are then accelerated by applying a potential of 100 kV to measure their polarization in the Mott spin detector .

To distinguish the precession of the polarization from the rotation both the directions of the initial spin polarization $\boldsymbol{P_0}$ and of the magnetization $\boldsymbol{M}$ are interchanged during the measurements. In this way we get four polarizations corresponding to the four possible combinations of the directions of polarization and magnetization. In reversing the polarization, only the angle of precession changes sign, while reversing the magnetization changes sign both of ε and ϕ. Hence it is possible to obtain separately the contribution of each spin motion. This technique also helps in eliminating the effects of the spin-orbit interaction.

How to inverse the initial spin polarization? The GaAs crystal is subjected to a laser beam whose wavelength is in the infrared range. The circular polarization is obtained by a Pockels cell. This is a device consisting of an electro-optical crystal through which a light beam can propagate. The phase delay in the crystal can be modulated by applying a variable electrical voltage. The Pockels cell thus acts as a voltage-controlled wave-plate. This cell has the ability to change between right and left circular polarizations simply by reversing the voltage applied to it. This gives us the possibility to quickly and easily reverse the initial polarization of the electrons.

How to inverse the direction of the magnetization? Coils which are placed on both sides of the sample, are used to invert the magnetization by a magnetic field pulse that is created by sending a current pulse across the coils. We note that a constant magnetic field can not be applied because the electrons would be too strongly deviated.

How to measure the angle of precession and rotation? We note that the actual geometry of our measurements (cf. Fig. 3.1) is different from that presented in the previous chapter "Electron-spin motion" (cf. Fig. 2.6). In the measurements the initial spin polarization vector is along the z-direction and the magnetization vector is in the xy-plane under an angle of 45 ° with respect to the x-axis. This is the reason for the appearance of a factor $1/\sqrt{2}$ in the following equations. The polarization in the four measured configurations

$\boldsymbol{P}(\pm\boldsymbol{P_0}, \pm\boldsymbol{M})$ are thus as follows:

$$\boldsymbol{P}^{(+\boldsymbol{P_0},+\boldsymbol{M})} = \begin{pmatrix} \frac{1}{\sqrt{2}}(-A + P_0\sqrt{1-A^2}\sin\varepsilon) \\ \frac{1}{\sqrt{2}}(A + P_0\sqrt{1-A^2}\sin\varepsilon) \\ P_0\sqrt{1-A^2}\cos\varepsilon \end{pmatrix} \tag{3.5}$$

$$\tag{3.6}$$

$$\boldsymbol{P}^{(-\boldsymbol{P_0},+\boldsymbol{M})} = \begin{pmatrix} \frac{1}{\sqrt{2}}(-A - P_0\sqrt{1-A^2}\sin\varepsilon) \\ \frac{1}{\sqrt{2}}(A - P_0\sqrt{1-A^2}\sin\varepsilon) \\ -P_0\sqrt{1-A^2}\cos\varepsilon \end{pmatrix} \tag{3.7}$$

$$\tag{3.8}$$

$$\boldsymbol{P}^{(+\boldsymbol{P_0},-\boldsymbol{M})} = \begin{pmatrix} \frac{1}{\sqrt{2}}(A - P_0\sqrt{1-A^2}\sin\varepsilon) \\ \frac{1}{\sqrt{2}}(-A - P_0\sqrt{1-A^2}\sin\varepsilon) \\ P_0\sqrt{1-A^2}\cos\varepsilon \end{pmatrix} \tag{3.9}$$

$$\tag{3.10}$$

$$\boldsymbol{P}^{(-\boldsymbol{P_0},-\boldsymbol{M})} = \begin{pmatrix} \frac{1}{\sqrt{2}}(A + P_0\sqrt{1-A^2}\sin\varepsilon) \\ \frac{1}{\sqrt{2}}(-A + P_0\sqrt{1-A^2}\sin\varepsilon) \\ -P_0\sqrt{1-A^2}\cos\varepsilon \end{pmatrix}. \tag{3.11}$$

$$\tag{3.12}$$

Thus, we have:

$$A = \frac{1}{2\sqrt{2}}(P_y^{(+\boldsymbol{P_0},+\boldsymbol{M})} + P_y^{(-\boldsymbol{P_0},+\boldsymbol{M})} - P_y^{(+\boldsymbol{P_0},-\boldsymbol{M})} - P_y^{(-\boldsymbol{P_0},-\boldsymbol{M})}), \tag{3.13}$$

and

$$\begin{cases} P_0\sqrt{1-A^2}\sin\varepsilon = \frac{1}{2\sqrt{2}}(P_y^{(+\boldsymbol{P_0},+\boldsymbol{M})} + P_y^{(-\boldsymbol{P_0},-\boldsymbol{M})} - P_y^{(-\boldsymbol{P_0},+\boldsymbol{M})} - P_y^{(+\boldsymbol{P_0},-\boldsymbol{M})}) \\ P_0\sqrt{1-A^2}\cos\varepsilon = \frac{1}{4}(P_z^{(+\boldsymbol{P_0},+\boldsymbol{M})} + P_z^{(+\boldsymbol{P_0},-\boldsymbol{M})} - P_z^{(-\boldsymbol{P_0},+\boldsymbol{M})} - P_z^{(-\boldsymbol{P_0},-\boldsymbol{M})}) \end{cases}. \tag{3.14}$$

From the coupled Eqns.3.14 we deduce the precession angle ε, and the initial polarization P_0 and from Eqn.3.13 we obtain A from which we can determine the rotation angle $\phi = \arctan\left(\frac{A}{P_0\sqrt{1-A^2}}\right)$.

Part II

Calculation of the electron-spin motion

Chapter 4

Computational Methods

Contents

This chapter describes the theoretical part of this thesis, i.e. the methods and approximations used in order to calculate the electron-spin motion. It is divided into three parts: the first part is dedicated to the density functional theory, whereas the second part describes the linear augmented plane wave method and the linear muffin-tin orbital method used to compute the band structure calculations. Finally, the third part presents the theory of spin-polarized low-energy electron diffraction (SPLEED) and describes how the SPLEED calculation is used to obtain the electron-spin motion.

4.1 Density Functional Theory

In order to calculate the electronic and magnetic properties of solids one must in principle solve the Schrödinger equation for many interacting particles, which is not a trivial task. In the last century, many approximations have been proposed to tackle this problem. One of the most important approximations is the Born-Oppenheimer approximation [33], which fixes the atomic nuclei and considers them as point charges, allowing only for the electrons to move. Such assumption is valid, since the nuclei are heavier than the electron who move much faster. The problem is now reduced to the interaction between the electrons and the nuclei, which is easy to solve, and to the interaction between the electrons themselves. As the solution of the latter problem is impossible to obtain, additional approximations become necessary.

Many attempts were made to estimate the electron-electron interaction, one of which is the Hartree-Fock approximation [34, 35]. The corner stone of this method is the mean-field theory (MFT). The main idea of MFT is to replace all interactions by one body with an average or effective interaction. This reduces the many-electron problem to an effective one-electron problem. The Hartree-Fock method is also called the self-consistent field method (SCF), since the approximation is parameter free, and the equation is solved by means of successive iterations. The main downfall of the Hartree-Fock approximation is the neglect of the electron-electron correlations, which can lead to large deviations from the experimental observations.

In the 1960's Hohenberg, Kohn, and Sham [36, 37] set the root to an alternative method of the Hartree-Fock approximation, known as the Density Functional theory (DFT). The basic ideas of DFT are contained in the two papers of Hohenberg, Kohn, and Sham and are referred to as the Hohenberg, Kohn, and Sham theorems. Instead of dealing with the many-body problem, as in Hartree-Fock approximation, the DFT deals with a formulation of the problem that involves the density of the electrons $n(r)$. For a spin-polarized system, $n(\boldsymbol{r}) = n^{\uparrow}(\boldsymbol{r}) + n^{\downarrow}(\boldsymbol{r})$ and one also has to introduce the so called magnetization density $m(\boldsymbol{r}) = n^{\uparrow}(\boldsymbol{r}) - n^{\downarrow}(\boldsymbol{r})$. This alternative method dealing with the electronic density instead of many-body Schrödinger equations, had quite good success in describing the electronic and magnetic properties of materials. In the next sections the formalism of the DFT will be explained in more detail.

4.1.1 Hohenberg-Kohn Theorem

As mentioned in the previous section, the basic idea of the DFT are contained in the original papers of Hohenberg, and Kohn. In the first paper Hohenberg and Kohn stated:

Theorem 1 *For any system of interacting particles in an external field $v_{ext}(\boldsymbol{r})$, the total energy of a system is a unique functional of the ground state electron density $n_0(\boldsymbol{r})$.*

In order to prove this theorem, consider a Hamiltonian, $H = T + V + W$, where T is the kinetic energy of the system, V the interaction of the electrons with the external potential, and W the electron-electron interaction. The solution of this Hamiltonian is:

$$H\Psi = E_0\Psi, \tag{4.1}$$

where Ψ is the ground state many-body wave function. In this case the electron density can be written as:

$$n(\boldsymbol{r}) = \langle\Psi|\sum_{i=1}^{N}\delta(\boldsymbol{r}-\boldsymbol{r_i})|\Psi\rangle, \tag{4.2}$$

and the interaction V :

$$V = \int n(\boldsymbol{r})v_{ext}(\boldsymbol{r})d^3r. \tag{4.3}$$

For a second external potential $v'_{ext}(\boldsymbol{r})$, the Hamiltonian can be written also as:

$$H'\Psi' = {E_0}'\Psi', \tag{4.4}$$

with Ψ' is the ground state many body wave function in the external potential v'_{ext}. From the variational principle one gets:

$$E_0 = \langle\Psi|H|\Psi\rangle < \langle\Psi'|H|\Psi'\rangle. \tag{4.5}$$

Adding and subtracting v'_{ext} on th right hand side of the previous equation one obtain:

$$\begin{aligned}\langle\Psi'|H|\Psi'\rangle &= \langle\Psi'|H+V'-V'|\Psi'\rangle = \langle\Psi'|H'+V-V'|\Psi'\rangle &(4.6)\\ &= E'_0 + \int n'(\boldsymbol{r})(v_{ext}(\boldsymbol{r}) - v'_{ext}(\boldsymbol{r}))d^3\boldsymbol{r}. &(4.7)\end{aligned}$$

Combining the expression in Eqns. 4.5 and 4.6 gives:

$$E_0 < E_0' + \int n'(\boldsymbol{r})(v_{ext}(\boldsymbol{r}) - v'_{ext}(\boldsymbol{r}))d^3r. \tag{4.8}$$

A similar argument, starts from the expression

$$E_0' = \langle \Psi' | H' | \Psi' \rangle < \langle \Psi | H' | \Psi \rangle, \tag{4.9}$$

and results in

$$E_0' < E_0 + \int n(\boldsymbol{r})(v'_{ext}(\boldsymbol{r}) - v_{ext}(\boldsymbol{r}))d^3\boldsymbol{r}. \tag{4.10}$$

Adding Eqn. 4.10 and 4.8 and assuming that we have the same electron density $n(\boldsymbol{r}) = n'(\boldsymbol{r})$, we get:

$$E_0' + E_0 < E_0' + E_0, \tag{4.11}$$

which is obviously wrong. Hence $n'(\boldsymbol{r}) \neq n(\boldsymbol{r})$, so the two different external potentials, $v_{ext}(\boldsymbol{r})$ and $v'_{ext}(\boldsymbol{r})$ give rise to different electron densities $n(\boldsymbol{r})$ and $n'(\boldsymbol{r})$, respectively. Thus, for a given external potential the electronic structure and the magnetic properties of a solid can be determined by the ground state electron density. This means that one can express the energy E, kinetic energy T, electron-electron interaction W, and the potential V as functionals of the electron density, as follows:

$$E[n(\boldsymbol{r})] = T[n(\boldsymbol{r})] + V[n(\boldsymbol{r})] + W[n(\boldsymbol{r})]. \tag{4.12}$$

The second ansatz or theorem as stated by Hohenberg and Kohn:

Theorem 2 *The exact ground state energy of the system is the global minimum value of the $E[n(\boldsymbol{r})]$, and the density $n(\boldsymbol{r})$ that minimizes the functional is the exact ground state density $n_0(\boldsymbol{r})$.*

Starting from the first theorem with an external potential V, one can prove the second theorem as follows:

$$E[n(\boldsymbol{r})] = \langle \Psi[n(\boldsymbol{r})] | T + W + V | \Psi[n(\boldsymbol{r})] \rangle. \tag{4.13}$$

If the ground state electron density is denoted by $n_0(\boldsymbol{r})$, then the ground state of the system, which specifies the energy, can be represented by $E[n_0(\boldsymbol{r})]$, and $\Psi[n_0(\boldsymbol{r})]$. Using again the variational principle one obtains:

$$\langle \Psi[n_0(\boldsymbol{r})] | T + W + V | \Psi[n_0(\boldsymbol{r})] \rangle < \langle \Psi[n(\boldsymbol{r})] | T + W + V | \Psi[n(\boldsymbol{r})] \rangle, \tag{4.14}$$

which can be written as

$$E[n_0(\boldsymbol{r})] < E[n(\boldsymbol{r})]. \tag{4.15}$$

This means that if the functional $E[n(\boldsymbol{r})]$ was known, then one can minimize it with respect to the electron density to obtain the ground state energy. For spin-polarized systems, similar arguments can be used to show that the ground state energy is a unique functional of the electron density $n(\boldsymbol{r})$ and the magnetization density $m(\boldsymbol{r})$. In this case an external magnetic field term $\boldsymbol{B}(\boldsymbol{r})$ should be included in the Hamiltonian, such that $H = T + W + U$ where $U = \int [v_{ext}(\boldsymbol{r})n(\boldsymbol{r}) - \boldsymbol{B}(\boldsymbol{r}).\boldsymbol{m}(\boldsymbol{r})]d^3r$.

4.1.2 Kohn-Sham equation

In 1965, Kohn and Sham proposed to replace the original many-body problem by an auxiliary independent particle problem. This Kohn-Sham ansatz is the milestone of most approximations used in calculating the properties of condensed matter and molecular systems, known as *ab initio* or first-principle calculation. Following their proposition, the many-body equation is replaced by a set of effective one-particle equations

$$\left[\frac{-\nabla^2}{2} + V_{eff}(\boldsymbol{r})\right]\psi_i(\boldsymbol{r}) = \varepsilon_i\psi_i(\boldsymbol{r}), \tag{4.16}$$

where the effective potential V_{eff} is given by

$$V_{eff}(\boldsymbol{r}) = V_{ext}(\boldsymbol{r}) + V_H(\boldsymbol{r}) + V_{xc}(\boldsymbol{r}). \tag{4.17}$$

The individual terms on the right hand side of Eqn. 4.17 are the following:

$$\text{The external potential} \;:\; V_{ext}(\boldsymbol{r}) = \sum_i \frac{e^2 Z_i}{|\boldsymbol{r} - \boldsymbol{R}_i|},$$

$$\text{The Hartree potential} \;:\; V_H(\boldsymbol{r}) = \int \tfrac{n(\boldsymbol{r}')}{|\boldsymbol{r}-\boldsymbol{r}'|} d^3r',$$

$$\text{The exchange correlation potential} \;:\; V_{xc}(\boldsymbol{r}) = \tfrac{\delta}{\delta n(\boldsymbol{r})} \int n(\boldsymbol{r})\varepsilon_{xc}(n(\boldsymbol{r}))d\boldsymbol{r}.$$

The Hartree potential is the electrostatic part of the electron-electron interaction. The external potential is due to the fixed nuclei of charge $Z_i e$. The last term V_{xc} includes all the effects of the many-body problem of the true

electronic system. Here ε_{xc} is the exchange and correlations energy density. For non magnetic systems the density can be written as:

$$n(\boldsymbol{r}) = \sum_{i=1}^{N} 2|\psi_i(\boldsymbol{r})|^2. \tag{4.18}$$

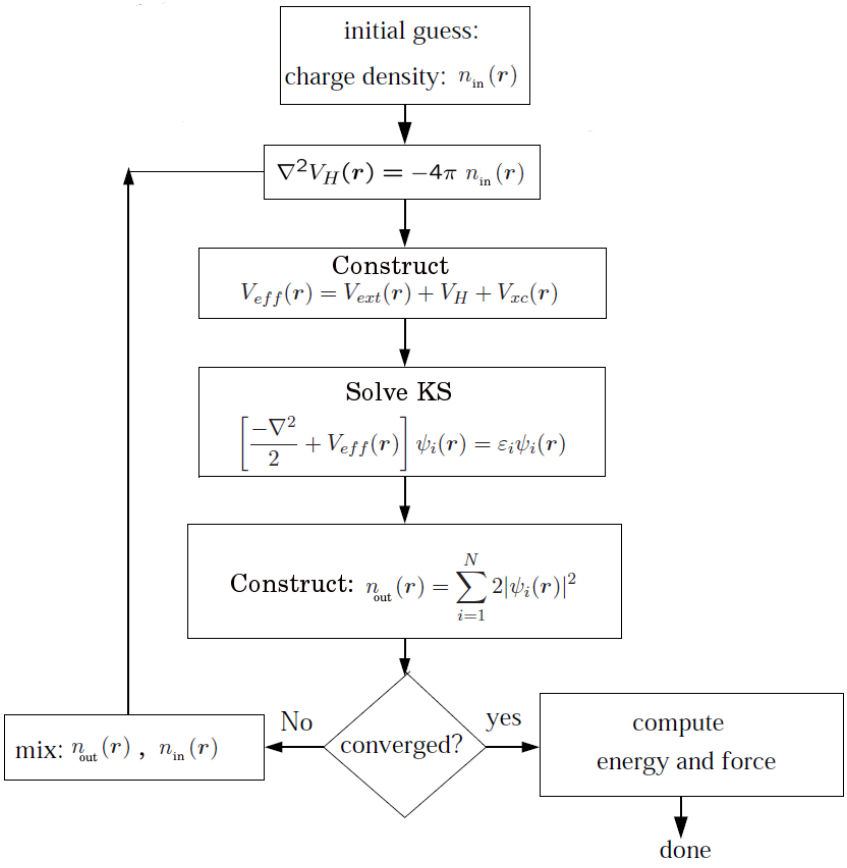

Figure 4.1: A Schematics of electronic structure calculation.

The set of equations (4.16-4.18) are called the Kohn-Sham equations. In order to solve these equations, one should perform a self-consistent calculation where a starting density is guessed (usually one starts from atomic densities), and from this density an effective potential is calculated. Introducing the effective potential in Eqn. 4.16, one obtains a new electron density which is used to calculate a new effective potential from Eqn. 4.17, and the same procedure is repeated until no further change of the electron density is observed. Then the total energy functional $E[n(\boldsymbol{r})]$, which can be expressed in terms of the

one particle energies ε_i (the Kohn-Sham eigenvalues) is calculated as follows:

$$E[n(\boldsymbol{r})] = T_0[n(\boldsymbol{r})] + V_{ext}(\boldsymbol{r}) + V_H + E_{xc}[n(\boldsymbol{r})], \tag{4.19}$$

where the independent-electron kinetic energy $T_0[n(\boldsymbol{r})]$ can be expressed in terms of the one electron energies ε_i as:

$$T[n(\boldsymbol{r})] = \sum_i \varepsilon_i - \int V_{eff}(\boldsymbol{r}) n(\boldsymbol{r}) d^3r. \tag{4.20}$$

Hence, the total energy can be rewritten as:

$$E[n(\boldsymbol{r})] = \sum_i \varepsilon_i - \frac{1}{2} V_H - V_{xc} + E_{xc}[n(\boldsymbol{r})]. \tag{4.21}$$

Unfortunately, due to the complexity of the electron-electron interaction, the exact form of the exchange-correlation potential V_{xc} and functional E_{xc} are unknown. Further approximations are required to obtain an explicit expression for $E[n(\boldsymbol{r})]$ in order to solve the electronic structure problem. The widely used approximations are the local density approximation and the generalized gradient approximation. They are discussed in the next section.

4.1.3 Local density approximation

Kohn and Sham proposed an approximation to express the exchange and correlation terms of the total energy functional. They argued that the complexity of the electron-electron interaction and the effect of exchange and correlation are local in general. Thus using a local density approximation (LDA) would be accurate enough to obtain a reasonable electronic structure of solids. In this approximation the exchange-correlation energy is assumed to be as in an homogeneous uniform electron gas:

$$E_{xc}[n(\boldsymbol{r})] = \int \varepsilon_{xc}^{hom}[n(\boldsymbol{r})] n(\boldsymbol{r}) d^3r, \tag{4.22}$$

where ε_{xc}^{hom} is the exchange-correlation energy density of a uniform electron gas. The exchange-correlation can be decomposed into an exchange and correlation term:

$$\varepsilon_{xc}^{hom} = \varepsilon_x^{hom} + \varepsilon_c^{hom}, \tag{4.23}$$

while the exchange term for a homogeneous electron gas is known analytically, and is expressed as:

$$E_x^{LDA}[n(\boldsymbol{r})] = -\frac{3}{4}\left(\frac{3}{\pi}\right)^{\frac{1}{3}} \int n(\boldsymbol{r})^{\frac{4}{3}} d^3\boldsymbol{r}. \tag{4.24}$$

However, an analytical expression for the correlation energy of the homogeneous electron gas is not known. Accurate quantum Monte Carlo simulations [38], using various approaches for the homogeneous electron gas provided values for the correlation energy with great accuracy. The exchange-correlation potential corresponding to the exchange-correlation energy within the local density approximation is given by:

$$V_{xc}^{LDA}(\boldsymbol{r}) = \frac{\delta E_{xc}^{LDA}}{\delta n(\boldsymbol{r})} = \varepsilon_{xc}[n(\boldsymbol{r})] + n(\boldsymbol{r})\frac{\partial \varepsilon_{xc}[n(\boldsymbol{r})]}{\partial n(\boldsymbol{r})}. \tag{4.25}$$

To account for the exchange and correlation energy of a spin-polarized system, one should distinguish between two electrons of same energy but of different spin. In such a system the local density approximation is replaced by the Local Spin Density Approximation (LSDA). The exchange-correlation energy becomes:

$$E_{xc}^{LSDA}[n^{\uparrow}, n^{\downarrow}] = \int n(\boldsymbol{r})\ \varepsilon_{xc}(n^{\uparrow}, n^{\downarrow}) d^3\boldsymbol{r}. \tag{4.26}$$

For the exchange energy, the exact expression is given in terms of the unpolarized exchange functional:

$$E_x[n^{\uparrow}, n^{\downarrow}] = \frac{1}{2}\left(E_x[2n^{\uparrow}] + E_x[2n^{\downarrow}]\right). \tag{4.27}$$

As for the spin-dependent correlation energy, the density is approximated by introducing the relative spin polarization:

$$\zeta(\boldsymbol{r}) = \frac{n^{\uparrow}(\boldsymbol{r}) - n^{\downarrow}(\boldsymbol{r})}{n^{\uparrow}(\boldsymbol{r}) + n^{\downarrow}(\boldsymbol{r})}. \tag{4.28}$$

For $\zeta = 0$, the system is unpolarized or paramagnetic, i.e. the spin-up and spin-down densities are equal. Although simple, the LDA results give a realistic description of the atomic structure, the elastic and vibrational properties for a wide range of systems. However, the LDA suffers from the unphysical self-interaction, resulting in some spurious interactions which are negligible in the homogeneous electron gas but can become large in confined systems. Hence, the LDA sometimes fails to give a reliable band structure for some systems where the electronic charge density is localized.

4.1.4 Generalized Gradient approximation

Beside their proposition of using LDA to account for the exchange and correlation functional, Kohn and Sham also suggested to develop the LDA into a gradient expansion approximation (GEA). However the gradients in real materials are so large that the expansion fails and breaks down leading in some situations to results worse than those obtained within LDA. This led to improve the GEA into generalized gradient approximations (GGA) by modifying the behavior at large gradients, in order to obtain a realistic description for the exchange-correlation problem. The exchange-correlation energy within GGA is written as following:

$$E_{xc}^{GGA}[n^{\uparrow}, n^{\downarrow}] = \int n(\boldsymbol{r}) f_{xc}(n^{\uparrow}, n^{\downarrow}, |\nabla n^{\uparrow}|, |\nabla n^{\downarrow}|) d^3r, \tag{4.29}$$

where $f_{xc}(n^{\uparrow}, n^{\downarrow}, |\nabla n^{\uparrow}|, |\nabla n^{\downarrow}|)$ is a function of the local density and its gradient. Many forms of f_{xc} have been proposed. The three widely used forms were developed by Becke (B88) [39], Perdew and Wang (PW91) [40] and Perdew, Burke, and Enzehof (PBE) [41]. Despite the fact that GGA leads to a better description of the charge density, incomplete cancellation of the self-interaction term remains a problem in particular for strongly correlated systems. A third generation gives a better description for the exchange-correlation energy, by adding two extra terms that are functionals of the the orbital occupation and independent of the charge density. This method, known as LDA(GGA)+U [42], is efficient to remove the self-interaction of the localized orbitals, resulting in a better description of the electronic structure of correlated systems.

4.2 Augmented functions for ab-initio calculations

Several approaches have been developed to solve the Kohn-Sham equations 4.16 and obtain the eigenvalues and eigenfunctions. These methods are at the heart of modern electronic structure calculations. One very common and simple method is to use plane waves as a basis set to represent the wave functions. However, large number of wave vectors are needed to represent the wave functions accurately, especially near the core region where the electron wave functions vary quickly. To overcome this problem, Slater [43, 44, 45] introduced a method based on expanding the wave function by using plane waves in the region between the atomic spheres and spherical symmetric functions within the atomic spheres. In this way, less basis functions are needed. This technique is called the augmented plane wave (APW) method, which separates the space into spherical regions around the nuclei and interstitial regions between these spheres. This approach is known as the "muffin-tin" approximation, which is also used in different methods like the linear muffin-tin orbital method (LMTO) [46], and various Green's function methods. One application is found in the variational theory developed by Korringa (1947) [47] and by Kohn and Rostocker (1954) [48] known as the KKR method.

In order to calculate the electron-spin motion we have used a layer-KKR (LKKR) method exploiting the self-consistent potential obtained from the LMTO as an input. Due to the limited wave function basis-set of the LMTO, the accuracy of the obtained potentials has been examined by comparing them to the ones obtained from the full-potential LAPW calculation. In the following sections we give an overview of the used methods, starting from the FLAPW, passing by the LMTO, and ending with the LKKR method.

4.2.1 The FLAPW Method

Before introducing the formalism of the full potential linearized augmented plane wave (FLAPW), it is more convenient to develop the concepts of augmented plane wave and linearized APW methods in the following two sub-subsections.

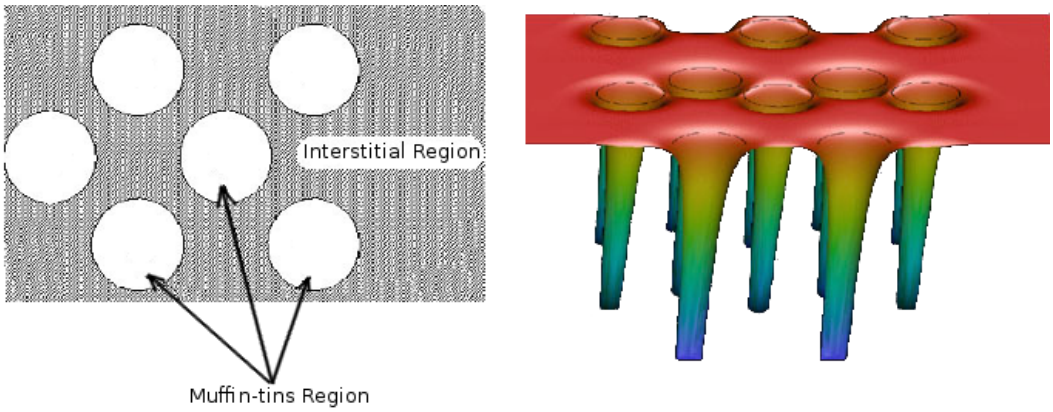

Figure 4.2: Schematics of the muffin-tin potentials.

4.2.1.1 The APW concept

As mentioned before, the space in the APW method is divided into muffin-tins and interstitial region. Inside the muffin-tins the potential is approximated to be spherically symmetric, and the interstitial potential is usually set to a constant. Hence the APW basis functions can be written as:[1]

$$\varphi_{\boldsymbol{G}}(\boldsymbol{k},\boldsymbol{r}) = \begin{cases} e^{i(\boldsymbol{G}+\boldsymbol{k})\boldsymbol{r}} & \text{interstitial region} \\ \sum_{lm} A_L^{\mu\boldsymbol{G}}(\boldsymbol{k}) u_l(r_\mu|E_l) Y_L(\hat{r}_\mu) & \text{muffin-tin } \mu, \end{cases} \tag{4.30}$$

where $\boldsymbol{k}$ is the Bloch wavevector, $\boldsymbol{G}$ a reciprocal lattice vector, E_l the energy parameter, L abbreviates the quantum numbers l and m, and u_l is the regular solution of the radial Schrödinger equation

$$\left\{ -\frac{\hbar^2}{2m}\frac{\partial^2}{\partial r^2} + \frac{\hbar^2}{2m}\frac{l(l+1)}{r^2} + V(r) - E_l \right\} r u_l(r) = 0. \tag{4.31}$$

Here $V(r)$ is the spherical component of the potential, the $A_L^{\mu\boldsymbol{G}}$ coefficients are determined by matching the wave functions at the muffin-tin spheres boundary so that the wave functions and their derivatives are continuous. Using the APW basis function the eigenvalue problem can be rewritten as:

$$(H(\boldsymbol{k}) - \varepsilon_{\nu\boldsymbol{k}} S(\boldsymbol{k})) C_{\nu\boldsymbol{k}} = 0, \tag{4.32}$$

where S is the overlap matrix. Within the APW, the E_l parameters are mapped to the real band energies $\varepsilon_{\nu\boldsymbol{k}}$. Thus, the u_l solutions become the

[1] For simplicity, we consider only one atom per unit cell. The generalization to many atoms per unit cell is trivial.

functions of these band energies. This makes Eq. 4.32 nonlinear in energy and it can no longer be determined by a simple diagonalization. One way to account for this problem is to fix the energies E_l and vary $\boldsymbol{k}$ to find the solutions $u_l(\varepsilon_{\nu\boldsymbol{k}})$. However, this method is computationally much more demanding. In addition to this problem, there is another limitation of the APW known as the asymptote problem which causes numerical difficulties if u_l becomes very small at the muffin-tins boundary.

4.2.1.2 The LAPW concept

To overcome the problems of the APW method resulting from the energy dependence of the Hamiltonian, a linearized version of the APW (LAPW) was introduced by Andersen [10], Koelling, and Arbman [49] in the middle of the seventies. The basic idea of their LAPW is to expand the u_l functions into a Taylor-series around the E_l energy parameters as:

$$u_l(\varepsilon, \boldsymbol{r}) = u_l(E_l, \boldsymbol{r}) + \dot{u}_l(E_l, \boldsymbol{r})(\varepsilon - E_l) + O[(\varepsilon - E_l)^2], \tag{4.33}$$

where $\dot{u}_l$ is the energy derivative of u_l, $\partial u_l(e, \boldsymbol{r})/\partial\varepsilon$, and $O[(\varepsilon - E_l)^2]$ are terms which are quadratic in energy. Therefore, according to the variational principle, the error in the calculated band energies is of the order $(\varepsilon - E_l)^4$. For this reason the linearization works very well even for broad energy regions. After linearizing, the basis function can be written as following:

$$\varphi_{\boldsymbol{G}}(\boldsymbol{k}, \boldsymbol{r}) = \begin{cases} e^{i(\boldsymbol{G}+\boldsymbol{k})\boldsymbol{r}} & \text{interstitial region} \\ \sum_{lm}(A_{lm}^{\mu\boldsymbol{G}}(\boldsymbol{k})u_l(r) + B_{lm}^{\mu\boldsymbol{G}}(\boldsymbol{k})\dot{u}_l(r))Y_L(\hat{r}_\mu) & \text{muffin-tin } \mu, \end{cases} \tag{4.34}$$

with $A_{lm}^{\mu\boldsymbol{G}}$ and $B_{lm}^{\mu\boldsymbol{G}}$ coefficients are determined, as in the APW, from the continuity condition at the sphere boundaries and from the normalization of u_l:

$$\langle u_l | u_l \rangle = \int_0^{R_{MT}} u_l^2(r) r^2 dr = 1, \tag{4.35}$$

where R_{MT} is the muffin-tin radius. Taking the derivative of (4.35) with respect to the energy, it can be easily shown that u_l and $\dot{u}_l$ are orthogonal, where $\dot{u}_l$ is calculated from a Schrödinger-like equation, that is obtained by taking the energy derivative of Eqn. 4.31

$$\left\{ -\frac{\hbar^2}{2m}\frac{\partial^2}{\partial r^2} + \frac{\hbar^2}{2m}\frac{l(l+1)}{r^2} + V(r) - E_l \right\} r\dot{u}_l(r) = u_l(r). \tag{4.36}$$

The solution of this equation has to be made orthogonal to u_l, since any linear combination of $\dot{u}_l$ and u_l can solve Eqn. 4.36. Nevertheless, one should be careful as the LAPW functions in general are not orthogonal to the core states, which may cause problems in the case of high-lying core states. A detailed discussion of these problems and their solutions can be found in the book of Singh [50]. However, the LAPW is able to overcome the limitations of the APW method. For example, the band energies can now be determined by a single diagonalization of the Hamiltonian matrix, which results in a faster computation. In addition, the asymptote problem found in APW, if u_l is zero at the sphere boundary, no longer exists because its radial derivative and $\dot{u}_l$ are in general nonzero. Another advantage of the LAPW method is that it can be extended to non-spherical muffin-tin potentials with little difficulty, because the basis offers enough variational freedom. This leads then to the full-potential linearized augmented plane wave method (FLAPW).

4.2.1.3 The FLAPW concept

The full-potential LAPW (FLAPW [51]) combines the choice of the LAPW basis set with the treatment of the full-potential and charge density without any shape approximation in the interstitial region and inside the muffin-tins. Hence, the potential in the unit cell $V(\boldsymbol{r})$ becomes:

$$V(\boldsymbol{r}) = \begin{cases} \sum_{\boldsymbol{G}} V_I^{\boldsymbol{G}} e^{i(\boldsymbol{G}.\boldsymbol{r})} & \text{interstitial region} \\ \\ \sum_L V_{MT}^L(r) Y_L(\hat{r}_\mu) & \text{muffin-tin } \mu, \end{cases} \tag{4.37}$$

where $\boldsymbol{G}$ are the reciprocal lattice vectors. The charge density is represented in the same way as the potential:

$$\rho(\boldsymbol{r}) = \begin{cases} \sum_{\boldsymbol{G}} \rho_I^{\boldsymbol{G}} e^{i(\boldsymbol{G}.\boldsymbol{r})} & \text{interstitial region} \\ \\ \sum_L \rho_{MT}^L(r) Y_L(\hat{r}_\mu) & \text{muffin-tin } \mu. \end{cases} \tag{4.38}$$

Construction of the potential

The total potential within the FLAPW consists of two parts, the exchange correlation potential and the Coulomb potential. The latter one is also com-

posed of two parts, the Hartree potential $V_H(\boldsymbol{r})$ and the external potential of the nuclei $V_{ext}(\boldsymbol{r})$:

$$V_c(\boldsymbol{r}) = V_H(\boldsymbol{r}) + V_{ext}(\boldsymbol{r}), \tag{4.39}$$

Once an initial charge density $n^0(\boldsymbol{r})$ and the atomic positions are given, the Hartree potential can be determined from the charge density via the Poisson equation:

$$\Delta V_H(\boldsymbol{r}) = en(\boldsymbol{r}). \tag{4.40}$$

In real space the solution of the equation is given by

$$V_H(\boldsymbol{r}) = \int \frac{n(\boldsymbol{r})}{|\boldsymbol{r} - \boldsymbol{r}'|} d^3r'. \tag{4.41}$$

Indeed, the Poisson equation is diagonal in reciprocal space

$$V_H(\boldsymbol{G}) = \frac{en(\boldsymbol{G})}{\boldsymbol{G}^2}, \tag{4.42}$$

and therefore, solving the Poisson equation in reciprocal space may appear convenient, due to the representation of the charge density and the potential in the interstitial region. However, in the muffin-tin region the charge density changes on a very small scale due to the localized core and valence states. Consequently, the plane wave expansion of n converges slowly, and a direct use of equation (4.42) is computationally prohibitive. To overcome this difficulty, a pseudocharge method developed by Weinert [52] is used to calculate the interstitial and vacuum Hartree potential. The basic idea is to divide the solution of the Poisson equation into two steps. In the first step the muffin-tin charge is replaced by a convergent pseudocharge density, that leads to the same potential outside the muffin-tins. Then the interstitial potential is calculated in reciprocal space. In the second step the muffin-tin potential is calculated from the Dirichlet boundary value problem, defined by the real muffin-tin charge and the interstitial potential on the sphere boundaries.

While the calculation of the Coulomb potential is conducted in reciprocal space, the calculation of the exchange-correlation potential and energy density (V_{xc}^{σ} , $\varepsilon_{xc}^{\sigma}$) has to be done in real space (since the two terms are non-linear function of the spin-dependent charge density). Once V_{xc}^{σ} and $\varepsilon_{xc}^{\sigma}$ are calculated in real space, they are back-transformed to the reciprocal space where V_{xc}^{σ} is added to the Coulomb potential to calculate the spin-dependent potential $(V_{eff}^{\uparrow}, V_{eff}^{\downarrow})$ and $\varepsilon_{xc}^{\sigma}$ is used to determine the total energy.

Construction of the Hamiltonian matrix

The FLAPW Hamiltonian and the overlap matrix elements consist of two contributions. One comes from the interstitial region, and the other from the muffin-tin region:

$$H = H_I + H_{MT} \text{ and } S = S_I + S_{MT}. \tag{4.43}$$

Once the Hamiltonian and the overlap matrix elements are determined in the whole space (where both contributions are calculated separately), the eigenvalue problem will be solved for each $\boldsymbol{k}$ point of the Brillouin zone.

Construction of the electron density

When the diagonalization of the Hamiltonian is achieved, the resulting eigenfunctions can be used to determine the charge density. It is given by an integral over the Brillouin zone:

$$n(\boldsymbol{r}) = \frac{2}{V_{BZ}} \int_{BZ} \sum_{\nu} |\psi_\nu(\boldsymbol{k}, \boldsymbol{r})|^2 f_\nu(\boldsymbol{k}) d^3k. \tag{4.44}$$

where $f_\nu(\boldsymbol{k})$ is the Fermi distribution for band ν and wave vector $\boldsymbol{k}$. In the spin dependent case, a spin-index σ is included in the summation. This integration is transformed into a weighted sum over the $\boldsymbol{k}$ points, where their weights depend on the integration method used. However the weights do not depend only on the $\boldsymbol{k}$ points, but also on the band energies. Each band contributes to the electron density only if its energy is below the Fermi level:

$$n(\boldsymbol{r}) = \sum_{\boldsymbol{k}} \sum_{\nu} |\psi_\nu(\boldsymbol{k}, \boldsymbol{r})|^2 w(\boldsymbol{k}, \varepsilon_\nu - E_F). \tag{4.45}$$

where w is the weight of the $\boldsymbol{k}$ point. The eigenfunctions in the FLAPW method are presented in terms of the coefficients of the augmented plane waves:

$$\psi_\nu(\boldsymbol{k}, \boldsymbol{r}) = \sum_{\boldsymbol{G}} C_\nu^{\boldsymbol{G}}(\boldsymbol{k}) \varphi_{\boldsymbol{G}}(\boldsymbol{k}, \boldsymbol{r}). \tag{4.46}$$

Inside the muffin-tin spheres each plane wave is coupled to a sum of spherical harmonics and radial functions. Hence, in a sphere μ the eigenfunctions are given by:

$$\psi_\nu(\boldsymbol{k},\boldsymbol{r}) = \sum_{\boldsymbol{G}} C_\nu^{\boldsymbol{G}}(\boldsymbol{k}) \sum_{lm} \left[A_{lm}^{\mu\boldsymbol{G}}(\boldsymbol{k}) u_l(r) + B_{lm}^{\mu\boldsymbol{G}}(\boldsymbol{k}) \dot{u}_l(r) \right] Y_L(\hat{r}_\mu). \tag{4.47}$$

By performing a contraction over the plane waves, the previous equation becomes:

$$\psi_\nu(\boldsymbol{k},\boldsymbol{r}) = \sum_{lm} \left[A_{lm}^{\mu}(\boldsymbol{k}) u_l(r) + B_{lm}^{\mu}(\boldsymbol{k}) \dot{u}_l(r) \right] Y_L(\hat{r}_\mu), \tag{4.48}$$

where

$$A_{lm}^{\mu}(\boldsymbol{k}) = \sum_{\boldsymbol{G}} C_\nu^{\boldsymbol{G}}(\boldsymbol{k}) A_{lm}^{\mu\boldsymbol{G}}(\boldsymbol{k}) \quad \text{and} \quad B_{lm}^{\mu}(\boldsymbol{k}) = \sum_{\boldsymbol{G}} C_\nu^{\boldsymbol{G}}(\boldsymbol{k}) G_{lm}^{\mu\boldsymbol{G}}(\boldsymbol{k}). \tag{4.49}$$

The contributions of the muffin-tins and the interstitial regions to the electron density are calculated separately.

Calculation of film within the FLAPW

The capability to treat surfaces is very important and crucial nowadays with the growing number of experiments employed in this area. However, surfaces are difficult to manage since they break the translational symmetry. Thus, making some adjustment to the basis set turns out to be necessary. In the case of a film of thickness D, the space is divided into three distinct regions: the interstitial region, the muffin-tins, and the vacuum region. Here the interstitial region is spreading from $-D/2$ to $D/2$ in the z-direction, which is normal to the surface of the film. However, the representation of the wave functions remains exactly the same inside the muffin-tin spheres as in the bulk case. Although the unit cell now extends from $-\infty$ to ∞ along the z-direction due to the lost periodicity in this direction, the wave functions can still be expanded in terms of plane waves. Indeed, the wave vectors perpendicular to the film are not defined in terms of D, but in terms of $\tilde{D}$, which is chosen to be larger than D to have greater variational freedom. Thus, the plane waves can be written as:

$$\varphi_{\boldsymbol{G}_{||}G_\perp}(\boldsymbol{k}_{||},\boldsymbol{r}) = e^{i(\boldsymbol{G}_{||}+\boldsymbol{k}_{||})\cdot\boldsymbol{r}_{||}} e^{iG_\perp z}, \tag{4.50}$$

with

$$G_\perp = \frac{2\pi n}{\tilde{D}}, \tag{4.51}$$

where $\boldsymbol{G}_{||}$ and $\boldsymbol{k}_{||}$ are the 2-dimensional wave and Bloch vectors, $\boldsymbol{r}_{||}$ is the parallel component of $\boldsymbol{r}$ and $G_\perp$ is the wavevector perpendicular to the film. The basis functions in the vacuum region are constructed in the same manner as the functions in the muffin-tins. They consist of plane waves parallel to the film, and a z-dependent function $u_{\boldsymbol{G}_{||}}(\boldsymbol{k}_{||}, z)$, which solves the following 1-dimensional Schrödinger equation:

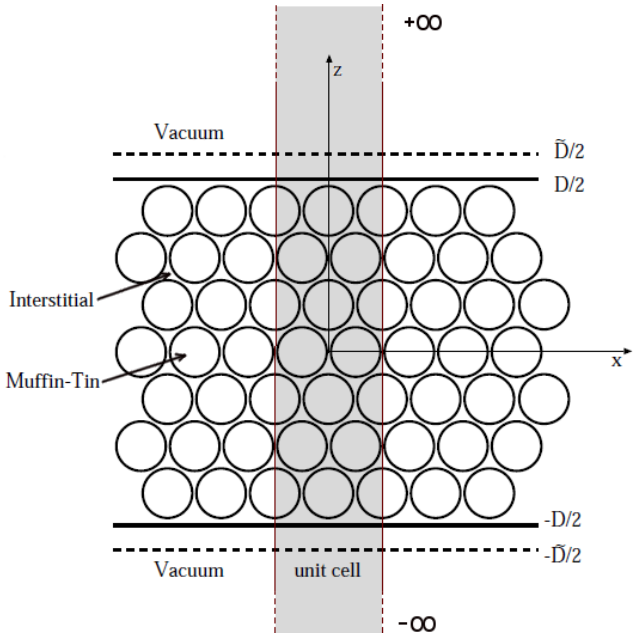

Figure 4.3: The unit cell in film calculations contains two semi-infinite vacuum regions

$$\left\{-\frac{\hbar^2}{2m}\frac{\partial^2}{\partial z} + V_0(z) - E_{vac} + \frac{\hbar^2}{2m}(\boldsymbol{G}_{||} + \boldsymbol{k}_{||})^2\right\} u_{\boldsymbol{G}_{||}}(\boldsymbol{k}_{||}, z) = 0. \tag{4.52}$$

Here, E_{vac} is the vacuum energy parameter and $V_0(z)$ is the planar-averaged part of the vacuum potential. As in the case of $\dot{u}$ in the muffin-tins, the functions $\dot{u}_{\boldsymbol{G}_{||}}(\boldsymbol{k}_{||}, z)$ are calculated from a Schrödinger-like equation, which is obtained by deriving equation (4.52) with respect to the energy

$$\left\{-\frac{\hbar^2}{2m}\frac{\partial^2}{\partial z} + V_0(z) - E_{vac} + \frac{\hbar^2}{2m}(\boldsymbol{G}_{||} + \boldsymbol{k}_{||})^2\right\} \dot{u}_{\boldsymbol{G}_{||}}(\boldsymbol{k}_{||}, z) = u_{\boldsymbol{G}_{||}}(\boldsymbol{k}_{||}, z). \tag{4.53}$$

The resulting basis function has the following form:

$$\varphi_{\boldsymbol{G}_{||}G_{\perp}}(\boldsymbol{k}_{||},\boldsymbol{r}) = \left\{A_{\boldsymbol{G}_{||}G_{\perp}}(\boldsymbol{k}_{||})u_{\boldsymbol{G}_{||}}(\boldsymbol{k}_{||},z) + B_{\boldsymbol{G}_{||}G_{\perp}}(\boldsymbol{k}_{||})\dot{u}_{\boldsymbol{G}_{||}}(\boldsymbol{k}_{||},z)\right\} e^{i(\boldsymbol{G}_{||}+\boldsymbol{k}_{||})\cdot\boldsymbol{r}_{||}}. \tag{4.54}$$

The coefficients $A_{\boldsymbol{G}_{||}G_{\perp}}(\boldsymbol{k}_{||})$ and $B_{\boldsymbol{G}_{||}G_{\perp}}(\boldsymbol{k}_{||})$ are determined in the same manner as in the muffin-tins by requiring that the functions are continuous and differentiable at the vacuum boundary. To increase the variational freedom in the vacuum basis functions, one might use instead of the energy parameter E_{vac} a whole series of $G_{\perp}$-dependent energy parameters (i.e $E^{i}_{vac} = E^{G_{\perp}}_{vac} = E_{vac} - \frac{\hbar^2}{2m}G^2_{\perp}$) [53]. Nevertheless, this is not necessary if the energy spectrum of the electrons in the vacuum region is small.

In summary, the basis set used for thin film calculations within the FLAPW method is

$$\varphi_{\boldsymbol{G}_{||}G_{\perp}}(\boldsymbol{k}_{||},\boldsymbol{r}) = \begin{cases} e^{i(\boldsymbol{G}_{||}+\boldsymbol{k}_{||})\boldsymbol{r}_{||}}e^{iG\perp z} & \text{interstitial} \\ \left\{A_{\boldsymbol{G}_{||}G_{\perp}}(\boldsymbol{k}_{||})u_{\boldsymbol{G}_{||}}(\boldsymbol{k}_{||},z)+ \right. & \\ \left. B_{\boldsymbol{G}_{||}G_{\perp}}(\boldsymbol{k}_{||})\dot{u}_{\boldsymbol{G}_{||}}(\boldsymbol{k}_{||},z)\right\} e^{i(\boldsymbol{G}_{||}+\boldsymbol{k}_{||})\cdot\boldsymbol{r}_{||}} & \text{vacuum} \\ \sum_{lm} A^{\mu\boldsymbol{G}}_{L}(\boldsymbol{k})u_l(r^{\mu})Y_L(\hat{r}) + B^{\mu\boldsymbol{G}}_{L}(\boldsymbol{k})\dot{u}_l(r^{\mu})Y_L(\hat{r}) & \text{MT } \mu \end{cases} \tag{4.55}$$

Furthermore, the charge density and potential are expanded in the same way. For the Hamiltonian and the overlap matrix, an additional term has to be included due to the vacuum contribution:

$$H = H_I + H_{MT} + H_V \qquad \text{and} \qquad S = S_I + S_{MT} + S_V. \tag{4.56}$$

4.2.2 The TB-LMTO method

Although the FLAPW method describes well the band structure of crystals, it requires a high computational effort. However, the linear muffin-tin orbital method, introduced by Andersen [54] in 1971 based on localized augmented orbitals, is characterized by its minimal basis set which provides high computational efficiency and gives as accurate results as the FLAPW. In the MTO the crystal potential, similar to the FLAPW, vary rapidly inside the atomic

sphere and is almost flat in the interstitial region. The potential inside the muffin-tin is approximated to be spherically symmetric and constant in the interstitial region as following:

$$V_{MT}(\boldsymbol{r}) = \begin{cases} 0 & \text{interstitial region} \\ v(\boldsymbol{r}) - V_{MTZ} & \text{muffin-tin } \mu, \end{cases} \tag{4.57}$$

where $v(\boldsymbol{r})$ is the spherically symmetric part of the crystal potential and the V_{MTZ} is the potential inside the muffin-tin. The solution of the Schrödinger equation inside the sphere is a product of spherical harmonics and radial wave function, and out side the spheres, i.e. in the interstitial region, is the Laplace equation. The MTO basis function as defined by Andersen is

$$\varphi_L(\varepsilon, \kappa, \boldsymbol{r}) = i^l Y_L(\hat{r}) \begin{cases} \kappa n_l(\kappa \boldsymbol{r}) & \text{interstitial region} \\ \\ u_l(\varepsilon, \boldsymbol{r}) + \kappa \cot(n_l) j(\kappa \boldsymbol{r}) & \text{muffin-tin } \mu, \end{cases} \tag{4.58}$$

where j_l and n_l are spherical Bessel and Neumann functions, respectively and the l and m quantum numbers have been combined into one subscript L. Y_L is the spherical harmonic, u_l is the radial amplitude, and κ^2 is the kinetic energy in the interstitial region and defined by :

$$\kappa = \sqrt{\varepsilon - V_{MTZ}}. \tag{4.59}$$

The atomic sphere approximation (ASA) chooses the muffin-tin radius in such a way that the total volume of the MT spheres is equal to the volume of the system. This means that the MT spheres have a slight overlap. In the interstitial region, the APW basis function are plane waves whereas the MTOs have more restricted form as they are solutions of the Laplace equation, i.e. they have zero kinetic energy. As $\kappa \to 0$ the regular and irregular solutions of the Laplace equation are respectively:

$$J_L(\boldsymbol{r}) = j_l(r) Y_L(\hat{r}) \qquad j_l(r) = \tfrac{1}{2(2l+1)} \left(\tfrac{r}{S}\right)^l, \tag{4.60}$$

$$N_L(r) = n_l(\boldsymbol{r}) Y_L(\hat{r}) \qquad n_l(r) = \left(\tfrac{r}{S}\right)^{-l-1}. \tag{4.61}$$

The solutions J_L and N_L centered at the origin of each atomic sphere are related to each other, where the irregular solution centered at R can be expanded into regular solutions centered at $R' \neq R$:

$$N_L(\boldsymbol{r_R}) = -\sum_{L'} S_{\boldsymbol{R}L,\boldsymbol{R'}L'} J_{L'}(\boldsymbol{r_{R'}}), \tag{4.62}$$

where $\boldsymbol{r_R} \equiv \boldsymbol{r} - \boldsymbol{R}$ and $S_{\boldsymbol{R}L,\boldsymbol{R'}L'}$ are the canonical structure constants, being symmetric ($S_{\boldsymbol{R}L,\boldsymbol{R'}L'} = S_{\boldsymbol{R'}L',\boldsymbol{R}L}$). The general form of the structure constants has an inverse power law dependence on the distance $|\boldsymbol{R} - \boldsymbol{R'}|$ such that:

$$S_{\boldsymbol{R}L,\boldsymbol{R'}L'} = g_{L',L} \sum_{|\boldsymbol{R}-\boldsymbol{R'}|} e^{i\boldsymbol{k}|\boldsymbol{R}-\boldsymbol{R'}|} \left[\frac{S}{|\boldsymbol{R}-\boldsymbol{R'}|}\right]^{l+l'+1} \left[\sqrt{4\pi} i^{l+l'} Y_{L'+L}(\widehat{|\boldsymbol{R}-\boldsymbol{R'}|})\right]^*, \tag{4.63}$$

where $g_{L',L}$ can be expressed in terms of the Gaunt coefficients [55]. The MTO basis can be written now as:

$$\varphi_L(\varepsilon, 0, \boldsymbol{r}) = i^l Y_L(\hat{r}) u_l(\varepsilon, S) \frac{l - D_l(\varepsilon)}{2l+1} \begin{cases} \left(\frac{S}{r}\right)^{l+1} & r > S \\ \frac{2l+1}{l-D_l(\varepsilon)} \frac{u_l(\varepsilon,r)}{u_l(\varepsilon,S)} - \frac{P_l(\varepsilon)}{2(2l+1)} \left(\frac{r}{s}\right)^l & r \leq S, \end{cases} \tag{4.64}$$

with the potential function $P_l(\varepsilon)$ defined as:

$$P_l(\varepsilon) = 2(2l+1)\frac{D_l(\varepsilon) + l + 1}{D_l(\varepsilon) - l}. \tag{4.65}$$

Here $D_l(\varepsilon)$ is a dimensionless logarithmic derivative of $u_l(\varepsilon, \boldsymbol{r})$ evaluated at the boundary $r = S$ of each MT sphere. Expanding the wave function for $r > S$ from sites $R' \neq 0$ on the central site as

$$\sum_{r_R} e^{i\boldsymbol{k}.\boldsymbol{r_R}} \left(\frac{r_R}{S}\right)^{-l-1} i^l Y_L(\hat{r}_R) = -\sum_{L'} \left(\frac{r_{R'}}{S}\right)^{l'} \frac{1}{2(2l'+1)} i^{l'} Y_{L'}(\hat{r}_{R'}) S_{\boldsymbol{R'}L',\boldsymbol{R}L}(\boldsymbol{k}), \tag{4.66}$$

where $r_R \equiv |\boldsymbol{r} - \boldsymbol{R}|$ and $S_{\boldsymbol{R'}L',\boldsymbol{R}L}(\boldsymbol{k})$ are the structure constants in reciprocal space, one might write the total wave function in the sphere at the origin as the sum of the wave functions from the sphere it self ("head function" for $r \leq S$) and the "tails" coming from the other atomic spheres (for $r > S$). The solution of the Schrödinger equation of the crystal can now be found for an eigenstate as a linear combination of the Bloch MTOs

$$\Psi_{\boldsymbol{k}}(\varepsilon, \boldsymbol{r}) = \sum_{L,R} \varphi_{L,\boldsymbol{k}}(\varepsilon, 0, \boldsymbol{r_R}) C_{R,L}(\boldsymbol{k}). \tag{4.67}$$

$\Psi_{\boldsymbol{k}}(\varepsilon, \boldsymbol{r})$ is an eigenfunction only if the "tail cancellation" condition is fulfilled, such that:

$$\sum_{\boldsymbol{R}',L'} [P_{\boldsymbol{R}L}(\varepsilon)\delta_{\boldsymbol{R}\boldsymbol{R}'}\delta_{LL'} - S_{\boldsymbol{R}'L',\boldsymbol{R}L}(\boldsymbol{k})]C_{\boldsymbol{R}',L'}(\boldsymbol{k}) = 0. \tag{4.68}$$

The structure constants $S_{\boldsymbol{R}'L',\boldsymbol{R}L}(\boldsymbol{k})$ contain all information about the crystal structure, whereas the potential function $P_{\boldsymbol{R}L}(\varepsilon)$ contains all information about the atomic potential. Thus, this equation can be used to determine the electronic band structure $\varepsilon(\boldsymbol{k})$. However, the energy dependence of the potential function complicates the problem and makes the MTO not efficient. Similar to the solution used to overcome the energy dependence of APW, one uses a linearized version of the MTO. The basic idea is to expand the function into Taylor-series around an energy parameter. The LMTO is an extremely fast method, in contrast to the LAPW method which needs higher order of l. While the LMTO is an accurate minimal basis technique, the interstitial region is not treated accurately for open structures. A correction term is usually used by adding "empty spheres" which can be done for static symmetric structures, but often fails when the structure is relaxed or deformed.

A tight-binding LMTO (TB-LMTO) [56] can be constructed by screening the structure constants and by taking in the construction of the basis set into account only the first and second nearest neighbours. The screened potential function and the screened structure constant matrix are related to the bare counterparts by means of a screening transformation

$$S^{\alpha} = S^{0}(1 - \alpha S^{0})^{-1} \tag{4.69}$$

$$P^{\alpha} = P^{0}(1 - \alpha P^{0})^{-1}, \tag{4.70}$$

where α is the screening parameter. This transformation does not affect the form of the tail cancellation condition. Since the transformation is exact, the TB-LMTO would reproduce the same result found in the long range method. However, the tight-binding version is computationally faster than the long ranged LMTO method.

4.3 Theory of spin-polarized Low-Energy Electron Diffraction

In 1927 Davisson and Germer [57] performed the first low-energy electron diffraction experiment and confirmed the wave-particle duality introduced by de Broglie. In these early works, the importance of low-energy electron diffraction as a tool for determining the surface structures has been recognized. However, the use of low-energy electron diffraction (LEED) as a tool for surfaces analysis was not popular until the early 1960's [58]. The LEED technique is characterized by its surface sensitivity due to the strong interaction between the low-energy electrons and the solid. A LEED experiment provides information on the atomic positions and the symmetry of the surface structure. Additional information about the spin-orbit coupling and the exchange energy in the case of ferromagnetic materials can be obtained by using a spin-polarized beam of electrons. This technique, known as spin-polarized LEED (SPLEED), is a powerful technique to study ferromagnetic materials which can be more sensitive to the details of the surface structure than the ordinary LEED. Pioneering works were made theoretically by Feder [59, 60, 61] and experimentally by Kirschner [62].

A first approach for a theoretical description of LEED is the kinematical theory, which assumes that the interaction of the LEED electrons with the solid is weak. This assumption is reasonable for electrons with high energies, whereas for very low-energy electron diffraction (VLEED) the results are far from being realistic. In order to describe well the interaction between the VLEED electrons and the solid, multiple scattering events should be taken into account. The main task of multiple scattering theory (MST) is to determine the scattering properties of the solid. This is done by consecutive calculation of the scattering properties of single site, single layer, multi layers, and finally the entire solid. In the early 1970's, Pendry used a layer formulation of the Korringa Kohn Rostoker (LKKR) method for a multiple scattering theory of low-energy electron diffraction [63, 64]. In the following, a theoretical description of LEED based on the MST in the LKKR formalism is presented.

4.3.1 Dynamical theory

The origin of LEED dynamical calculation (multiple scattering) can be traced back to the band structure theory of Korringa [47], Kohn, and Rostoker [48] who formulated it for a three dimensional systems. A two dimensional version of the KKR is more appropriate to treat surfaces in terms of layers. Before treating the interlayer scattering by means of a layer-KKR method, it is useful first to introduce the scattering properties of a beam of electrons from a single site.

4.3.1.1 Single site scattering

The first step in MST calculation is to determine the scattering properties of a single site. As in LMTO and APW methods, the potential in the LKKR is spherically symmetric in the muffin-tin region, and constant in the interstitial region:

$$V(\boldsymbol{r}) = \begin{cases} 0 & \text{interstitial region} \\ v(\boldsymbol{r}_\mu) & \text{muffin-tin } \mu. \end{cases} \tag{4.71}$$

Usually, the spheres of different sites do not overlap.

For the relativistic case, the Dirac equation for a single site is

$$\left[c\alpha.\boldsymbol{p} + \beta mc^2 + V(\boldsymbol{r}) + \beta\sigma.\boldsymbol{B}(\boldsymbol{r})\right]\Psi(\boldsymbol{r}) = E\Psi(\boldsymbol{r}) \tag{4.72}$$

where α, β, and Ψ are defined in the first chapter, and $B(\boldsymbol{r})$ is an effective magnetic field. The scattering solution is:

$$\langle \boldsymbol{r}|\Psi\rangle = \frac{1}{r}\sum_{\Lambda}\begin{pmatrix} f_\Lambda(r)\langle\hat{\boldsymbol{r}}|\chi_\Lambda\rangle \\ ig_\Lambda(r)\langle\hat{\boldsymbol{r}}|\chi_{\bar{\Lambda}}\rangle \end{pmatrix} = \sum_{\Lambda}\begin{pmatrix} \Psi_\Lambda(r)\langle\hat{\boldsymbol{r}}|\chi_\Lambda\rangle \\ i\Phi_\Lambda(r)\langle\hat{\boldsymbol{r}}|\chi_{\bar{\Lambda}}\rangle \end{pmatrix}. \tag{4.73}$$

Here $\Psi_\Lambda(r) = f_\Lambda(r)/r$ and $\Phi_\Lambda(r) = g_\Lambda(r)/r$. The relativistic analog χ^μ_κ to the spherical harmonic is obtained by coupling l and s

$$\chi^\mu_\kappa = \sum_{\sigma=\pm 1/2} C(l \pm \frac{1}{2}; \mu-\sigma, \sigma) Y_l^{\mu-\sigma}\chi^\sigma, \tag{4.74}$$

where the C are the Clebsch-Gordan coefficients, μ is a half-integer number that runs from $-l-\frac{1}{2}$ to $l+\frac{1}{2}$, and χ^μ_κ are the eigenfunctions of $\boldsymbol{\sigma.l}+1$ with eigenvalues $\kappa = (j+\frac{1}{2})^2 - l(l+1)$. For $j = l+\frac{1}{2}$ ($j = l-\frac{1}{2}$) one has $\kappa = -l-1$ ($\kappa = l$). The index Λ in Eqn. 4.73 combines the relativistic

angular-momentum quantum numbers μ and κ, $\Lambda = (\kappa, \mu)$ and $\overline{\Lambda} = (-\kappa, \mu)$. By taking the spin quantization axis along the z-direction and introducing the wave function into the Dirac equation, one obtains a set of coupled equations for f_Λ and g_Λ

$$c\partial_r f_\Lambda = -c\frac{\kappa}{r} f_\Lambda + (E + c^2 - v) g_\Lambda + \boldsymbol{B} \sum_{\Lambda'} \langle \chi_{\overline{\Lambda}} | \sigma_z | \chi_{\overline{\Lambda'}} \rangle g_{\Lambda'}, \tag{4.75}$$

$$c\partial_r g_\Lambda = c\frac{\kappa}{r} g_\Lambda - (E + c^2 - v) g_\Lambda + \boldsymbol{B} \sum_{\Lambda'} \langle \chi_{\Lambda} | \sigma_z | \chi_{\Lambda'} \rangle f_{\Lambda'}. \tag{4.76}$$

In the case where $\boldsymbol{B} = \boldsymbol{0}$ (nonmagnetic), the solutions become independent of the magnetic quantum number μ. The matrix elements σ_z can be obtained from the definition of χ_Λ. Once the value of σ_z is inserted in Eqns. 4.75 and 4.76, terms that couple the angular momentum l and $l+2$ are obtained. However, those terms can be neglected due to the missing singularity of the effective magnetic field at the origin. This provides a system of four coupled differential equations of first order in the partial waves with angular momentum κ and $-\kappa - 1$. There are two types of solutions to the coupled differential equations, namely regular and irregular solutions. For $r \to \infty$ the asymptotic behavior of the two solutions is:

$$\langle \boldsymbol{r} | \Psi_\Lambda^{reg} \rangle \to \sum_{\Lambda'} \begin{pmatrix} [j_l(kr)\delta_{\Lambda'\Lambda} + h_{l'}^+(kr) t_{\Lambda'\Lambda}] \langle \hat{\boldsymbol{r}} | \chi_{\Lambda'} \rangle \\ iS_{\kappa'} \frac{ck}{E+c^2} [j_{\overline{l}}(kr)\delta_{\Lambda'\Lambda} + h_{\overline{l'}}^+(kr) t_{\Lambda'\Lambda}] \langle \hat{\boldsymbol{r}} | \chi_{\overline{\Lambda'}} \rangle \end{pmatrix} \tag{4.77}$$

$$\langle \boldsymbol{r} | \Psi_\Lambda^{irr} \rangle \to \sum_{\Lambda'} \begin{pmatrix} h_{l'}^+(kr)\delta_{\Lambda'\Lambda} \langle \hat{\boldsymbol{r}} | \chi_{\Lambda'} \rangle \\ iS_{\kappa'} \frac{ck}{E+c^2} [h_{\overline{l'}}^+(kr)\delta_{\Lambda'\Lambda}] \langle \hat{\boldsymbol{r}} | \chi_{\overline{\Lambda'}} \rangle \end{pmatrix}, \tag{4.78}$$

where j_l and $h_l^\pm$ are defined as the spherical Bessel and Hankel functions[2], respectively. The total wave function can be written as:

$$\langle \boldsymbol{r} | \Psi \rangle = \sum_\Lambda \left(A_\Lambda \langle \boldsymbol{r} | J_\Lambda \rangle + B_\Lambda \langle \boldsymbol{r} | H_\Lambda^{(+)} \rangle \right). \tag{4.79}$$

with

$$\langle \boldsymbol{r} | J_\Lambda \rangle = \begin{pmatrix} j_l(kr) \langle \hat{\boldsymbol{r}} | \chi_\Lambda \rangle \\ iS_\kappa \frac{ck}{E+c^2} j_{\overline{l}}(kr) \langle \hat{\boldsymbol{r}} | \chi_{\overline{\Lambda}} \rangle \end{pmatrix} \tag{4.80}$$

$$\langle \boldsymbol{r} | H_\Lambda^{(\pm)} \rangle = \begin{pmatrix} h_l^\pm(kr) \langle \hat{\boldsymbol{r}} | \chi_\Lambda \rangle \\ iS_\kappa \frac{ck}{E+c^2} h_{\overline{l}}^\pm(kr) \langle \hat{\boldsymbol{r}} | \chi_{\overline{\Lambda}} \rangle \end{pmatrix}. \tag{4.81}$$

[2]The $\pm$ signs refer to $h_\alpha^\pm = \frac{j_{-\alpha} - e^{\mp \alpha \pi i} j_\alpha}{\pm i \sin(\alpha\pi)}$.

The coefficients A_Λ (incoming) and B_Λ (outgoing) are related by the single-site t matrix as follows:

$$B_\Lambda = \sum_{\Lambda'} t_{\Lambda\Lambda'} A_{\Lambda'}. \tag{4.82}$$

The single-site matrix can be obtained by first solving numerically the coupled differential Eqns. 4.75-4.76 inside the muffin-tin and then matching the general solution at the sphere boundary with a linear combination of outside solutions (Eqns. 4.80-4.81) with specified A_Λ to determine the scattered B_Λ. For a spherical potential, the elements of t that belong to the partial wave coupled by the radial Dirac equation are nonzero. Once the elastic single-site scattering problem is solved in terms of the t matrix, the problem of many-site scattering can be treated by adding up the single-site events. The total wave field incident on a site i, consists of the "direct" term ψ_i^0, incident on a system of N atomic sites, and the sum of the wave field scattered from the other sites j. Thus the total wave field can be written as

$$\psi_i = \psi_i^0 + \sum_{j \neq i}^{N} G_{ij} t_j \psi_j, \tag{4.83}$$

where G_{ij} is the Green function of one electron propagating from site j to site i. The total scattered wave field is given by

$$\psi_i^{sc} = t\psi_i = t_i (1 - \sum_j G_{ij} t_j)^{-1} \psi^0 = \tau_i \psi^0 \tag{4.84}$$

Eqn. 4.84 relates the incident field ψ^0 to the scattered one by the scattering path operator τ. The incoming and outgoing plane-wave spinors for a N atom system are related via the matrix T which can be obtained from the scattering path operator τ.

4.3.1.2 Scattering by a single layer

The term that describes the scattering properties of a single layer is the essential object in layer-KKR. This term can be calculated starting from the single-site t matrix. For each incident beam that is characterized by the reciprocal lattice vector $\boldsymbol{g}$, one can define the wave vector $\boldsymbol{k}_g^{\pm}$

$$\boldsymbol{k}_g^{\pm} = \begin{pmatrix} \boldsymbol{k}_{\parallel} + \boldsymbol{g} \\ \pm\sqrt{k^2 - (\boldsymbol{k}_{\parallel} + \boldsymbol{g})^2} \end{pmatrix}, \tag{4.85}$$

where the $+(-)$ refers to plane waves propagating in the $+z$ $(-z)$ direction. In this case the incident (scattered) wave field $\Psi^{in}(\boldsymbol{r})$ ($\Psi^{sc}(\boldsymbol{r})$ can be written as

$$\Psi^{in}(\boldsymbol{r}) = \sum_{g\sigma} [u^{+}_{g\sigma} e^{i\boldsymbol{k}_g^{+}\cdot\boldsymbol{r}} + u^{-}_{g\sigma} e^{i\boldsymbol{k}_g^{-}\cdot\boldsymbol{r}}]\chi^{\sigma} \tag{4.86}$$

$$\Psi^{sc}(\boldsymbol{r}) = \sum_{g\sigma} [v^{+}_{g\sigma} e^{i\boldsymbol{k}_g^{+}\cdot\boldsymbol{r}} + v^{-}_{g\sigma} e^{i\boldsymbol{k}_g^{-}\cdot\boldsymbol{r}}]\chi^{\sigma}. \tag{4.87}$$

The relation between the incident ($u^{\pm}_{g\sigma}$) and the scattered ($v^{\pm}_{g\sigma}$) wave field coefficients can be expressed in terms of the scattering matrix T of the layer as following:

$$\begin{pmatrix} \boldsymbol{v}^{+} \\ \boldsymbol{v}^{-} \end{pmatrix} = \begin{pmatrix} \boldsymbol{T}^{++} & \boldsymbol{T}^{+-} \\ \boldsymbol{T}^{-+} & \boldsymbol{T}^{--} \end{pmatrix} \begin{pmatrix} \boldsymbol{u}^{+} \\ \boldsymbol{u}^{-} \end{pmatrix}. \tag{4.88}$$

Here the T matrix corresponds to the single-site matrix but for an entire layer, with the blocks of the T matrix are given by

$$T^{ss'} = \delta_{ss'} + a^{s} t (1 - X)^{-1} b^{s'}, \tag{4.89}$$

where a^s (b^s) transforms from angular momentum into a plane wave representation (vice versa) , and X is called the "multiple-scattering matrix" defined as

$$X_{\Lambda''\Lambda} = \sum_{\Lambda'} t_{\Lambda''\Lambda'} \sum_{j} e^{i\boldsymbol{K}_{\parallel}\cdot\boldsymbol{R}_j} G_{\Lambda'\Lambda}(-\boldsymbol{R}_j), \tag{4.90}$$

where $\boldsymbol{R}_j$ is the j-th atomic position, and $G_{\Lambda'\Lambda}$ is the relativistic layer structure constant [65].

4.3.1.3 Scattering by a stack of layer

Using the layer scattering matrices and introducing the plane wave propagator $\boldsymbol{P}^{\pm}_{g\sigma,g'\sigma'}$, the total scattering by two layers $T_{1,2}$ can be calculated

$$T_{1,2}^{++} = T_2^{++}(1 - P^+T_1^{+-}P^-T_2^{-+})^{-1}P^+T_1^{++} \quad (4.91)$$
$$T_{1,2}^{--} = T_2^{--}(1 - P^-T_1^{-+}P^+T_2^{+-})^{-1}P^-T_1^{--} \quad (4.92)$$
$$T_{1,2}^{-+} = T_1^{-+} + T_1^{--}P^-T_2^{-+}(1 - P^+T_1^{+-}P^-T_2^{-+})^{-1}P^+T_1^{++} \quad (4.93)$$
$$T_{1,2}^{+-} = T_2^{+-} + T_2^{++}P^+T_1^{+-}(1 - P^-T_2^{-+}P^+T_1^{+-})^{-1}P^-T_2^{--}. \quad (4.94)$$

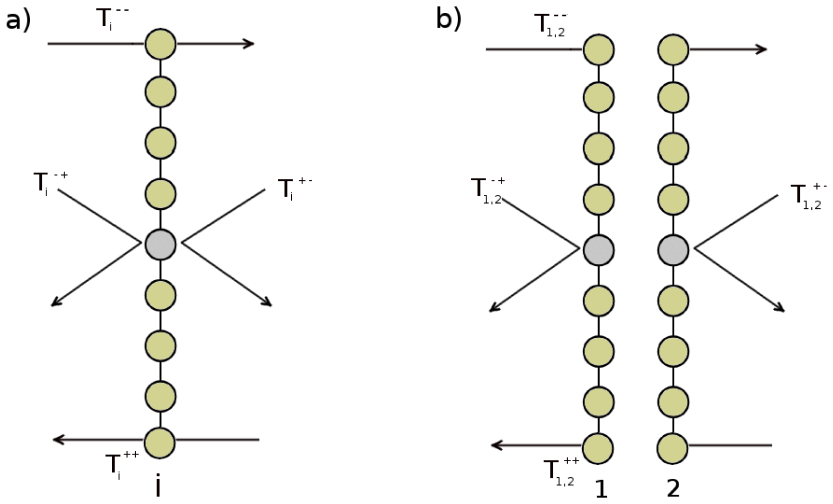

Figure 4.4: Schematic illustration of the four reflection matrices from a single layer.

The elements of the diagonal matrix $P^{\pm}$ are defined by

$$\boldsymbol{P}^{\pm}_{g\sigma,g'\sigma'} = e^{i\boldsymbol{K}_g^{\pm}.\boldsymbol{d}}\delta_{gg'}\delta_{\sigma\sigma'}, \quad (4.95)$$

where $\boldsymbol{d}$ is the translational vector from layer 1 to layer 2. The relation between $T_{1,2}^{++}$ and $T_{1,2}^{--}$, as well as the relation between $T_{1,2}^{-+}$ and $T_{1,2}^{+-}$, is symmetric, i.e. one expression can be obtained from the other by interchanging $+ \leftrightarrow -$ and $1 \leftrightarrow 2$. Once the scattering matrices of a double layer are calculated, the T matrix of a doubled double layer (a stack of four layers) can be easily obtained. Applying this procedure for n iterations, one obtains the T matrix of a stack of 2^n layers. The reflection matrix is given by T^{-+} of the 2^n-layer stack. Before obtaining the total reflection matrix, one has to consider the surface region of the solid by treating the surface barrier as an additional layer. The T matrices of the surface region are:

$$T^{++}_{g\sigma g'\sigma'} = \frac{2k_{\perp g}}{k_{\perp g} + k^{in}_{\perp g}}\delta_{gg'}\delta_{\sigma\sigma'} \tag{4.96}$$

$$T^{--}_{g\sigma g'\sigma'} = \frac{2k^{in}_{\perp g}}{k_{\perp g} + k^{in}_{\perp g}}\delta_{gg'}\delta_{\sigma\sigma'} \tag{4.97}$$

$$T^{+-}_{g\sigma g'\sigma'} = \frac{k^{in}_{\perp g} - k_{\perp g}}{k_{\perp g} + k^{in}_{\perp g}}\delta_{gg'}\delta_{\sigma\sigma'} \tag{4.98}$$

$$T^{-+}_{g\sigma g'\sigma'} = \frac{k_{\perp g} - k^{in}_{\perp g}}{k_{\perp g} + k^{in}_{\perp g}}\delta_{gg'}\delta_{\sigma\sigma'}, \tag{4.99}$$

with

$$k_{\perp g} = \sqrt{2E - (\boldsymbol{k}_{\parallel} + \boldsymbol{g})^2} \tag{4.100}$$

$$k^{in}_{\perp g} = \sqrt{2(E + V_0) - (\boldsymbol{k}_{\parallel} + \boldsymbol{g})^2}, \tag{4.101}$$

where V_0 is the energy shift of the muffin-tin potential inside the solid relative to the vacuum level, usually called the inner potential. In VLEED calculations, the fine structure features are determined more precisely by image-asymptotic potential and can therefore be described by a one dimensional surface barrier model. Using Bloch theorem, the band structure of the bulk $k_{\perp}(E, \boldsymbol{k}_{\parallel})$ can be calculated starting from the T matrix of a stack of layer. Bloch theorem also provides an accurate method of treating diffraction by a semi-infinite stack of identical layers. Considering u^{+}_{g} and v^{-}_{g} to be the incident and the reflected plane-wave spinors amplitudes[3], respectively, the bulk reflection matrix R^b is written as

$$v^{-}_{g\sigma} = \sum_{g'\sigma'} R^{b}_{gg'\sigma\sigma'} u^{+}_{g'\sigma'}. \tag{4.102}$$

Once the bulk reflection matrix and the scattering matrix of i layers are calculated, the reflection matrix of the stack of all the layers with index greater than or equal to i is given by

$$R^{-+}_{i} = T^{-+}_{i} + T^{--}_{i} P^{-} R^{-+}_{i+1} (1 - P^{+} T^{+-}_{i} P^{-} R^{-+}_{i+1})^{-1} P^{+} T^{++}_{i}, \tag{4.103}$$

[3]For an infinitely thick slab, u^{-} equals to zero because the incoming waves from the $-z$ direction vanish.

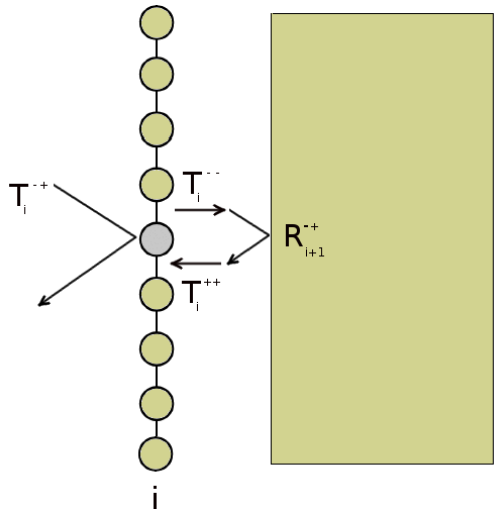

Figure 4.5: Schematic illustration of reflection from a stack of layers.

where $T_i^{\pm\pm}$ are the scattering matrices of layer i, and R_{i+1}^{-+} are the reflection matrices of the stack of layers with index greater than i. The first term of Eq. 4.103 corresponds to the reflection at layer i, whereas the second term corresponds to the multiple scattering between layer i and the stack of layers on the right hand side of layer i. Starting from R^b and $T_n^{\pm\pm}$, one obtains the first non-bulk-like layer n with a reflection matrix R_n^{-+}. Then from R_n^{-+} and $T_{n-1}^{\pm\pm}$, one can calculate R_{n-1}^{-+}, and so forth. Finally, the total reflection matrix R^{tot} of the semi infinite system is obtained.

4.3.2 Spin-polarized LEED and spin motion

Spin-polarized low-energy electrons can be scattered not only by the Coulomb potential of the surface atoms but also by the exchange potential associated with the magnetic structure. This technique is found to be useful for studying ferromagnetic materials [62]. Once the total reflection matrix R^{tot} of the system is computed, the reflected intensity I_g and the outgoing polarization vector $\boldsymbol{P}_g^{out}$ are calculated in terms of the incoming electron spin polarization $\boldsymbol{P}_g^{in}$. We recall that the density matrix of the incoming electrons ϱ^{in} is related to the spin polarization by

$$\varrho^{in} = \frac{1}{2}(1 + \boldsymbol{P}^{in}).\sigma, \tag{4.104}$$

The density matrix of the outgoing electrons ϱ_g^{out} is related to ϱ_g^{in} via

$$\varrho_g^{out} = \varrho_g \varrho^{in} \varrho_g^{\dagger}, \tag{4.105}$$

with

$$\varrho_{g\sigma\sigma'} = R^{tot}_{g\sigma,0\sigma'} \left(\frac{E_{\perp g}}{E_{\perp 0}} \right), \tag{4.106}$$

where $E_{\perp g}$ is the effective energy given by $E_{\perp g} = 2E - (k_{\parallel} + g)^2$. The outgoing spin polarization and the reflected intensities are expressed in terms of ϱ_g^{out} as following:

$$I_g = tr(\varrho_g^{out}) \qquad P_g^{out} = \frac{tr(\sigma \varrho_g^{out})}{I_g}. \tag{4.107}$$

The obtained spin polarization can be used now to calculate the spin motion angles ε and φ. Taking the initial polarization along the y-direction and the magnetization perpendicular to it along the x-direction, the two spin motion angles can be written as a function of the P^{out} components

$$\varepsilon = -\arctan\left(\frac{P_z}{P_y} \right) \tag{4.108}$$

$$\phi = \arctan\left(\frac{P_x}{\sqrt{P_y^2 + P_z^2}} \right), \tag{4.109}$$

where P_x, P_y, and P_z are the x,y, and z components of the outgoing spin polarization.

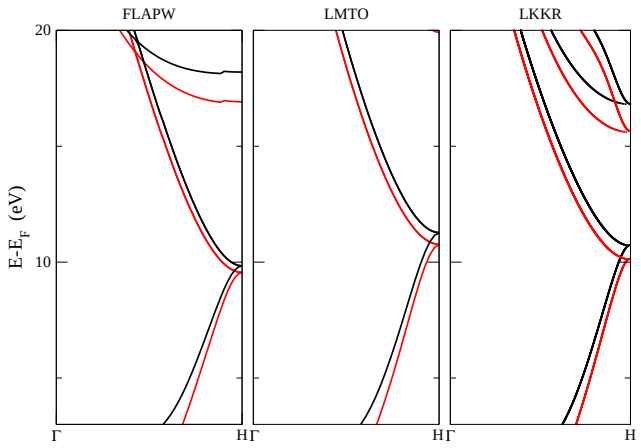

Figure 4.6: Electronic band structure of Fe calculated by three different methods, along the high symmetry direction ΓH.

In summary, the electronic band structure is calculated using the linear muffin-tin orbital method (LMTO) [66], which provides the converged potential to compute the spin-polarized low-energy electron diffraction (SPLEED) by means of the layer Korringa-Kohn-Rostoker method [11]. The calculated polarization of the scattered electrons is then used to obtain the electron-spin motion angles. The relaxation of the films was performed using the full potential linearized augmented plane wave (FLAPW) method [67]. In order to check the validity of the SPLEED calculation, a comparison between the electronic band structure calculated by the three different methods is performed. The band structure of bulk Fe calculated along the high symmetry direction ΓH shows a similar behavior in the low energy region. We focus on the very low energy region (0 to 15 eV) for two reasons. One is related to the limited wave function basis-set of the LMTO, where the error increases as the energy increases above the vacuum level (cf. Fig. 4.6). Second, the results obtained from the experiment show significant structures only in the low-energy region.

Part III

Spin motion results

Chapter 5

Giant spin precession due to lattice relaxation

Contents

In order to study the influence of the lattice relaxation on the electron-spin motion one needs a suitable approach to vary the lattice parameter of a ferromagnetic crystal. This is possible in the calculations where there is a wide range of possibilities that can be realistic or not. However, experimentally this is not an easy task. There is yet no tool which allows to choose the lattice parameter of any crystal. The only possible way is to look into the literature for a reported lattice relaxation due to some external agents. A possible lattice relaxation of the ferromagnetic films in some cases can be induced by choosing a proper substrate, where the difference in the lattice parameter between the film and the substrate can make the film lattice parameter vary over a wide range during its growth. Due to the simplicity of this approach, the idea of investigating the electron-spin motion during the growth of a ferromagnetic film is tempting. Therefore, in this chapter we present experimental and theoretical results on the electron-spin motions of Fe films during its growth on Ag(001). Further theoretical results on other transition metals are also presented.

5.1 Fe on Ag

The choice of the Fe/Ag(001) system is mainly motivated by the fact that the small lattice mismatch (i.e -0.9%) between the body-centered cubic (bcc) Fe lattice and the face-centered cubic (fcc) lattice of Ag leads to a good epitaxy of Fe on Ag (001). For the following studies Fe films deposited at room temperature on Ag(001) have been chosen; a system which has been extensively investigated in the past [68, 69, 70, 71].

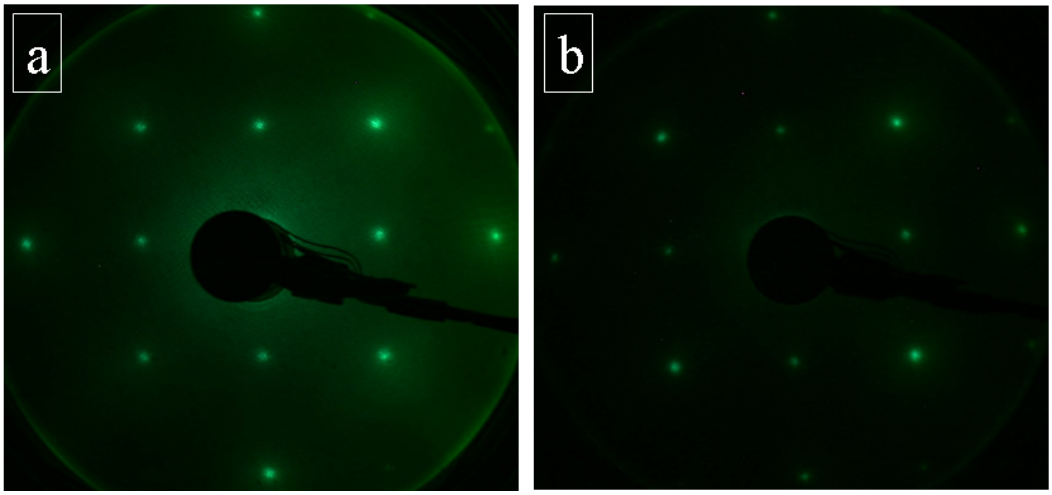

Figure 5.1: LEED diffraction patterns of a single crystal of Ag (001) at 120 eV electron energy, (b) of 35 ML Fe on Ag (001) at 100 eV. The axis [110] of the Ag(001) crystal is horizontal.

In the experiment the monocrystalline Fe(001) films were prepared by evaporating Fe from an iron rod. Prior to the deposition, the Ag crystal was etched by Argon ion bombardment and then annealed at a temperature of 800 K to improve the quality of the Ag surface. For experimental needs the Ag crystal was oriented so that the direction [110] is in the plane defined by the incident and the reflected electrons. In this configuration the magnetization easy axis of the Fe film is in the plane of the scattered electrons. Figure 5.1 (a) shows the LEED diffraction patterns from the Ag(001) substrate at 120 eV electron energy, and (b) shows the LEED pattern for a 35 monolayer (ML) (1 ML = 0.143 nm) Fe film on Ag(001) at 100 eV. We note that the diffraction pattern of the bcc-Fe(001) resembles that of the fcc-Ag(001) surface. This is only possible if the Fe structure is rotated by an angle of 45 ° with respect to the [100] of the Ag substrate.

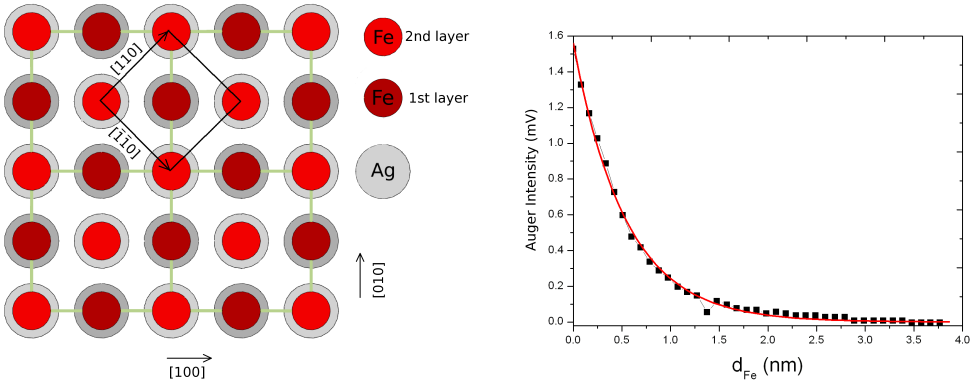

Figure 5.2: (Left) Atomic arrangement of the first two Fe layers deposited on Ag (001). The unit cell of Fe is rotated by 45° with respect to the unit cell of Ag. (Right) Auger peak intensity of Ag at 351 eV depending on the thickness of Fe deposited on single crystal Ag(001). The deposition rate is around 0.1 nm/min.

In the first layer of the Fe film grown on top of Ag(001), Fe atoms occupy the empty sites between the Ag surface atoms along the [100] and [010] direction (cf. Fig. 5.2 (left)). The arrangement of the second atomic layer of Fe is identical to that of the Ag surface. This atomic arrangement of Fe leads to a surface structure identical to that of Ag atoms, and thus a similar diffraction pattern is obtained.

Figure. 5.2 (right) shows the Ag Auger peak intensity as function of Fe film thickness for an energy of 351 eV. The deposition was done in steps of 30 s at a speed of 0.1 nm/min. After each step an Auger spectrum was measured. As each measurement took few minutes, the average speed of deposition was much slower than 0.1 nm/min. By analyzing the decay in Fig. 5.2 (left), we find an attenuation length of the electrons in Fe of 0.6 nm, which agrees well with the mean free path of electrons at this energy in Fe calculated by Tanuma *et al* [79], and is therefore consistent with a layer-by-layer growth of Fe on Ag(001).

5.2 Experimental results

Figure 5.3 shows that the evaporation rate has also a great influence on the behavior of the spin precession as a function of Fe thickness. The same sensitivity is also found for the rotation angle ϕ. While "fast evaporation" (i.e. 0.2 nm/min) leads to modest ε-values of about 10 ° for thick films, one obtains

much larger values of up to 60° by "slow evaporation" (i.e. 0.02 nm/min).

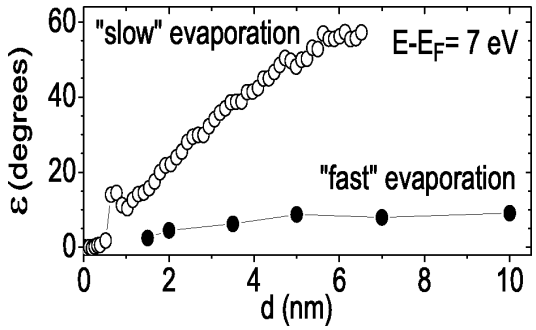

Figure 5.3: Precession angle ε as function of the Fe film thickness for two different evaporation rates at a primary electron energy of 7 eV energy.

In the following we will explain this and other results as consequences of lattice relaxations which take place during the growth of Fe on Ag. In fact, thin films grown on a substrate are generally subject to strain arising from different lattice parameters of the film material and the substrate. In the present case of Fe on Ag(001) the lattice misfit is $-0.9\,\%$. It has been shown that strain causes two relaxation mechanisms in thin films during their growth. In a limited thickness range up to a critical thickness d_c, the bulk of the film has the same lattice parameter as the substrate. In this pseudomorphic growth regime (cf. Fig.5.4 (left)), relaxation occurs only at the incomplete surface layer. The surface lattice can relieve the strain by a relaxation of the atomic positions at island edges. Experiments by Massies *et al.* [72] with semiconducting InGaAs films on GaAs and by Fassbender *et al.* [73] with metallic Co films on Cu(001) have shown that at the island edges of the incompletely filled top layer, the in-plane atomic spacing is different from that of completed layers. This results in an oscillatory variation of the average in-plane lattice parameter at the surface as a function of film thickness. Previous spin-polarized electron reflection experiments done by Logane Tati Bismaths [74, 75] on Fe films on Ag(001) showed oscillations of the electron-spin precession as a function of the Fe thickness with monolayer periodicity. These oscillation are attributed to periodic variations of the surface-lattice parameter of Fe during growth. Beside oscillations of the electron-spin motion with ML periodicity, oscillations due to quantum interference have also been observed.

On the other hand, for film thicknesses above the critical thickness, the

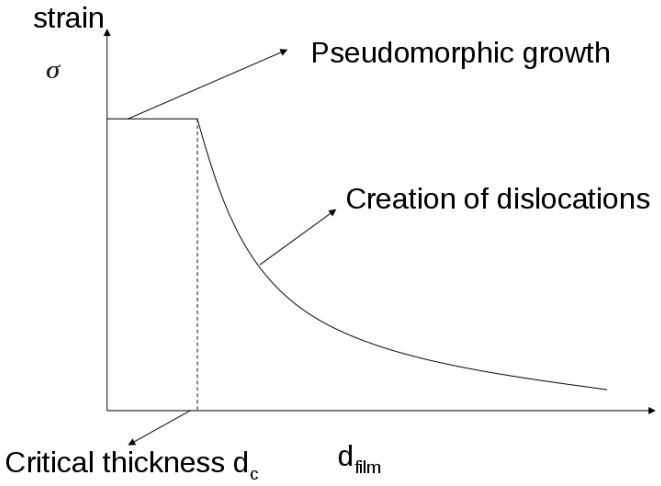

Figure 5.4: Schematic of the strain σ as function of the film thickness d_{film}.

misfit-induced strain is relieved by the creation of interfacial dislocations [9]. Obviously, the dislocated film is more stable than the coherently strained film: the energy gained from the relief of misfit strain is greater than the energy expended by the creation of dislocations. In the simplest model, the equilibrium model [76], the thickness dependence of the misfit-induced strain is $\tau(d) = \eta d_c/d$ for $d > d_c$ with d the film thickness and η the misfit between substrate and film. However, many experimental data do not follow this behavior. In fact, Freund [77] has shown that the interaction between a moving dislocation and an orthogonal dislocation partially blocks the relaxation process. This has for instance be demonstrated for the system MgO/Fe(001) [78]. Another important point is that the strain relaxation above the critical thickness strongly depends on the growth temperature and increases drastically with increasing temperature.

The strong difference between the two data sets in Fig. 5.3 might therefore be explained by the fact that dislocations have to overcome energy barriers related to their mobility with the help of thermal fluctuations, so that a characteristic time for their creation is needed. This time has to be compared with other characteristic times of the experiment, such as the time to grow one ML, i.e., the inverse of the growth rate. Thus, one expects a more effi-

cient strain relaxation with film thickness if the growth rate is sufficiently low. By closer inspection of the thickness dependence for the "slow" evaporation

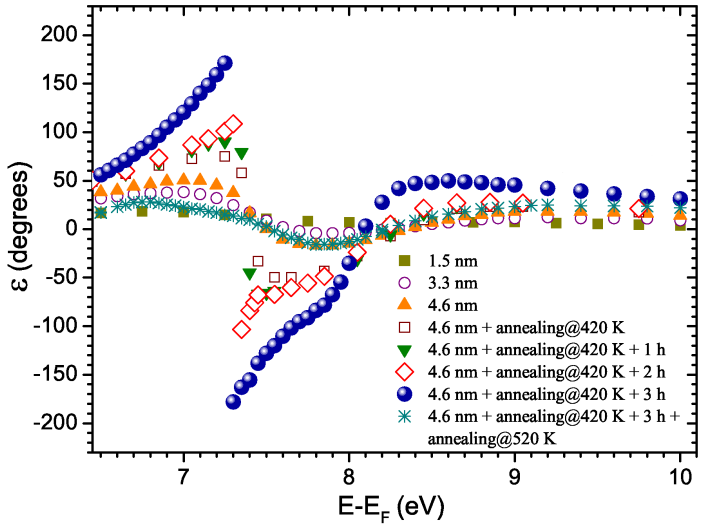

Figure 5.5: Precession angle ε versus primary electron energy $E - E_F$ for different Fe samples. The inset shows ε versus Fe film thickness at a primary electron energy of 7 eV.

rate one remarks that it is linear over a large thickness range. This might be astonishing if we suppose an equilibrium strain relaxation as its origin, which would lead to a much stronger and non-linear relaxation with thickness [76]. However, as expla ined above, an equilibrium relaxation is not necessarily expected, and the much weaker linear behavior can be explained by a blocking of both nucleation and propagation of dislocations [77].

Figure 5.5 shows ε for different Fe samples. In a first step the thickness of the Fe film, deposited at the "slow" rate at room temperature, has been varied. Around 7.4 eV a "plus/minus"-structure is observed which becomes more pronounced with increasing thickness. As it is seen in Fig. 5.3, ε saturates for thicknesses above 5 nm. Supposing that the strain relaxation is responsible for the increase of ε as a function of the Fe thickness, one might expect a further increase by annealing the Fe film, as strain relaxation is known to be promoted by higher temperatures. Annealing the 4.6 nm Fe film at 420 K for 10 min leads in fact to a drastic increase of the "plus/minus"-structure's amplitude. Further measurements show that this feature is not yet stable but

its amplitude increases further with time. This finding points clearly to the presence of a very slow relaxation process. After about 3 h the ε-structure stabilized and exhibited the maximum value of 180 °. It is noted that a further increase of ε above 180 ° is indistinguishable from a rise of ε from −180 ° towards less negative values. It is emphasized that a thick Fe film annealed at 420 K for a longer time (30 min) shows directly the 180 °-structure without the need for additional waiting. Finally, the Fe sample showing the 180 °-structure has been annealed at 520 K for 30 min, leading to surface diffusion of Ag, as evidenced by Auger spectroscopy. This results in a strong decrease of the ε-structure's amplitude.

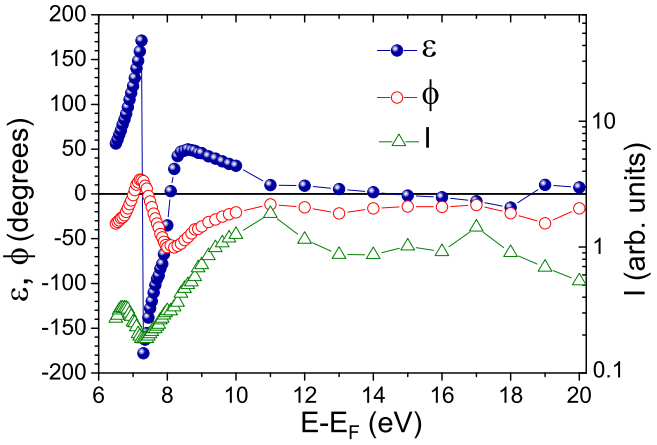

Figure 5.6: Spin-integrated electron reflectivity I, precession angle ε and rotation angle ϕ as a function of the primary electron energy $E - E_F$ for a 4.6 nm thick Fe film after annealing at 420 K.

Figure 5.6 shows the spin-motion angles ε and ϕ as well as the reflected intensity I of a 4.6 nm Fe film after annealing at 420 K over a wider energy range. We note that the strong ε-structure at 7.4 eV is accompanied by a pronounced minimum in the reflected electron intensity. Although small compared to the low-energy structure, ε exhibits for most electron energies above 10 eV quite significant values. The rotation angle ϕ shows also a very strong structure in the energy range $7 - 8$ eV with a minimum value of −60 °. We emphasize that the maximum and minimum possible values are 90 ° and −90 °, respectively, which correspond to situations in which the electron-spin polarization is either parallel or antiparallel to the magnetization.

5.3 Theoretical results

In order to confirm our hypothesis that the relaxation of the Fe lattice during growth is responsible for the ultimate electron-spin precession upon reflection, we conducted *ab initio* calculations of the electronic band structure of Fe films. The electronic band structure is obtained using the linear muffin-tin orbital method and the spin precession by the Korringa-Kohn-Rostoker (KKR) method. In order to make a comparison with our experimental data, the geometry for the spin precession calculations was chosen identical to the experimental one. First, we inspected the spin-dependent band structure of Fe for various lattice relaxations in order to evidence features that may change pronouncedly as a function of relaxation. However, no significant changes in the band structure are found in the energy range of the giant spin precession. One should note that the spin-down and the spin-up reflection phases, the difference of which determines the precession angle, do not appear in the electronic band structure. It is only in the reflection process and thus in the KKR calculations in which the phases appear. The spin motion calculation

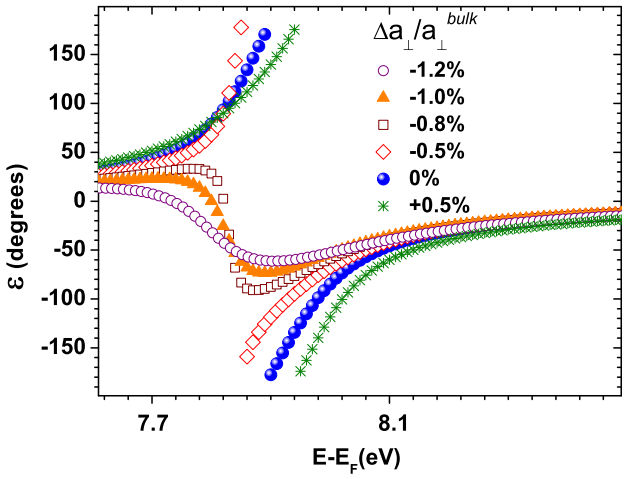

Figure 5.7: The calculated ε as function of the electron energy for different degrees of strains for bcc-Fe(001).The corresponding calculated vacuum level is at 2.8 eV.

was performed for different degrees of strain. To make our calculation more realistic an additional surface relaxation was taken into account by relaxing the last two Fe layers using the FLAPW method. In the case of non-strained

Fe lattice, the lattice structure was taken as body centered cubic with a lattice parameter of 0.2866 nm.

Figure 5.7 shows the ε for different degrees of relaxations. In the following, we assumed that the volume of a lattice unit is always conserved. In fact, LEED experiments on a similar system, Fe/GaAs(001), show such behavior [80]. Consequently, if the in-plane lattice parameter $a_{\parallel}$ of Fe is for instance expanded by 1 %, the out-of-plane lattice parameter $a_{\perp}$ decreases by about 2 %. The calculation shows that for large Fe lattice strain the plus/minus-structure is relatively small but becomes more pronounced with decreasing strain. In particular, a very strong increase is found between $\Delta a_{\perp}/a_{\perp}^{\mathrm{bulk}} = -0.8\,\%$ and $-0.5\,\%$, with $\Delta a_{\perp} = a_{\perp}^{\mathrm{film}} - a_{\perp}^{\mathrm{bulk}}$ being the difference between the out-of-plane lattice parameter in the film and in the bulk. For values in the range of $[-0.5\,\%, 0.7\,\%]$, the precession angle reaches the ultimate limit of 180 °.

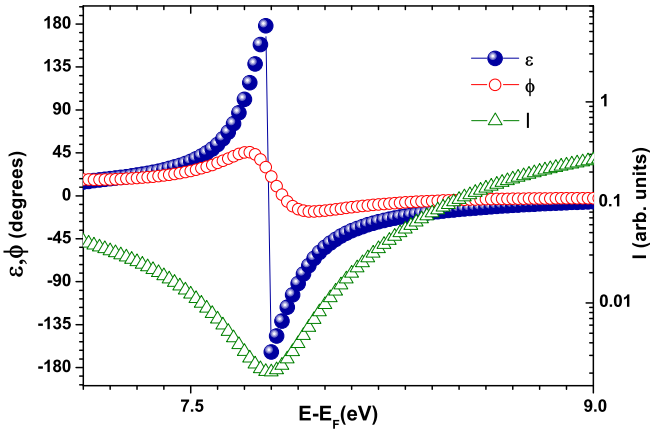

Figure 5.8: Calculated precession angle ε, rotation angle ϕ, and reflected intensity I versus electron energy for completely relaxed (not strained) Fe film.

For a completely relaxed (not strained) Fe film (cf. Fig. 5.8), i. e. $\Delta a_{\perp}/a_{\perp}^{\mathrm{bulk}} = 0$, the ±180 °-structure in ε is accompanied by a strong structure in ϕ and a pronounced minimum in the reflected intensity, as in the experiment. Inspection of the rotational angle reveals that ϕ is also sensitive to lattice relaxation. In the case of bcc-Fe(001) (cf. Fig. 5.10 (middle)), it varies from a large negative peak structure that reaches −60 ° for a +0.5 % relax-

ation, to its ultimate value of $+90\,^\circ$ for $-0.8\,\%$ strain. Increasing the strain furthermore, the rotational angle ϕ decreases again to reach $+60\,^\circ$ for $-1.2\,\%$ strain.

We notice that the ε-, the ϕ-, and the I-structures are considerably sharper than in the experiment. Since this finding cannot be explained by the energy resolution of the experimental set-up ($\sim 0.3\,\mathrm{eV}$), we can only speculate on the reason for this difference. In summary, the KKR calculations clearly reproduce the experimental trends, especially the structure around 7.8 eV for bcc-Fe(001) coincides with its experimental counterpart at 7.4 eV.

In order to see whether the appearance of a giant spin precession structure is a more general phenomena and not restricted to Fe films, calculations with other ferromagnetic materials were performed. Indeed, for fcc-Co(001), bcc-Co(001), and bcc-Ni(001) we predict similar structures around 3.4 , 7.6 , and 16.7 eV, respectively. In contrast, for fcc-Fe(001) and fcc-Ni(001) we could not identify such a structure in our calculations in the investigated energy range.

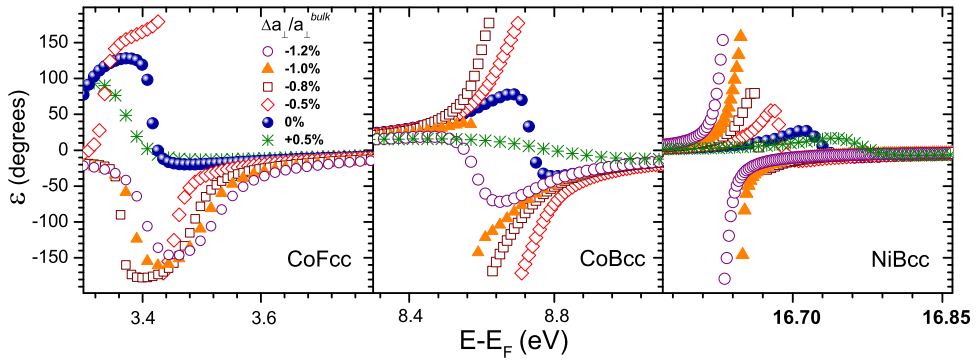

Figure 5.9: Calculated ε as function of the electron energy for different degrees of strains for fcc-Co(001) (left), bcc-Co(001)(middle), and bcc-Ni(001) (right). The corresponding calculated vacuum levels are at 3.3 , 3.4 , and 5.5 eV, respectively.

In bcc-Co(001) and bcc-Ni(001), the $180\,^\circ$-structure appears for relaxations in the range of $[-0.8\,\%, -0.5\,\%]$ and $[-1.5\,\%, -1\,\%]$, respectively. In bcc-Co(001), the $\pm$ structure's amplitude starts to increase with increasing the strain and reaches its maximum value of $180\,^\circ$ for relaxations in the range of

$[-0.8\,\%, -0.5\,\%]$. For larger degrees of strain, above $-0.8\,\%$, the amplitude becomes relatively small and comparable to the non-strained case. In fcc-Co(001) a $\pm 180\,^{\circ}$-structure appears around $-0.5\,\%$ relaxation. Interestingly, it develops into a $-180\,^{\circ}$-peak for a stronger strained lattice before its amplitude decreases again. Thus, in any case, the $180\,^{\circ}$-structure is extremely sensitive to the lattice relaxation.

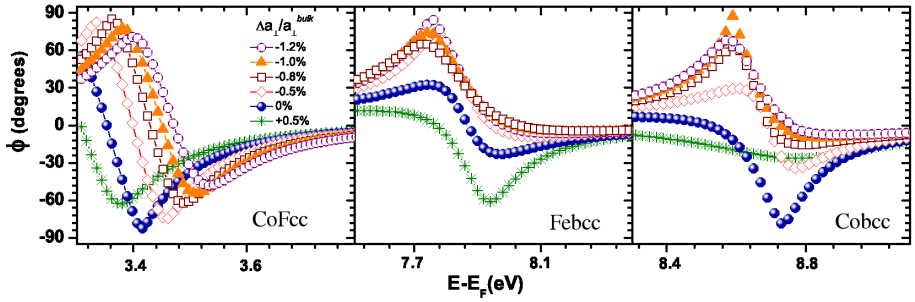

Figure 5.10: Calculated ϕ as function of the electron energy for different degrees of strains for fcc-Co(001) (left), bcc-Fe(001)(middle), and bcc-Co(001) (right).

For the rotational angle a similar behavior of ϕ as in the case of bcc-Fe(001) is also found in the case of bcc-Co(001), fcc-Co(001), and bcc-Ni(001) where ϕ varies between $\pm 90\,^{\circ}$ in the energy range where the $\pm 180\,^{\circ}$-structure in ε appears.

5.3.1 Ramsauer-Townsend effect

How can one understand in simple terms without going into the details of the KKR calculations that a giant spin precession appears around a particular electron energy and is accompanied by an intensity minimum? To obtain a strong ε-structure it is clear that each spin-dependent phase $\theta^{\uparrow,\downarrow}$ has to exhibit a strong variation. This behavior of each phase is reminiscent of the so-called Ramsauer-Townsend effect. In the 1920s Ramsauer and Townsend observed that for very slow electrons (0.7 eV kinetic energy) scattered from Ar-atoms, the observed scattering was much weaker than expected from gas kinetic theory [81, 82]. It was Bohr who suggested that one is dealing here with a resonance phenomenon which combines weak scattering with a strong

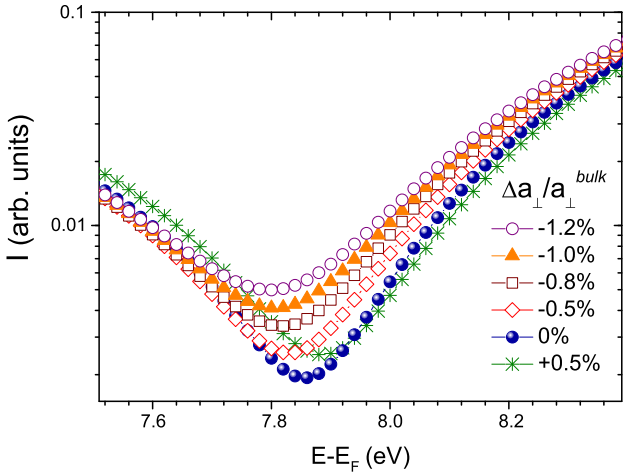

Figure 5.11: Calculated intensity I as function of the energy for different degrees of relaxation for bcc-Fe(001) case.

change of the scattering phase. In fact, in order to get a minimum scattering intensity the wave function of the electrons within the scattering potential has to fulfill certain boundary conditions which in turn lead to a certain resonance condition for the electron energy. For example, considering a simple square potential well of width a and depth U, the resonance condition reads:

$$ka = \frac{2n+1}{2}\pi \tag{5.1}$$

with

$$k \sim \sqrt{E_{kin} + U} \tag{5.2}$$

the electron momentum inside the potential well, E_{kin} the kinetic energy of the electrons outside the potential well and n an integer. On the other hand, the scattering phase is known to change quite strongly around the resonance energy, because the phase matching condition between scattered and unscattered wave is not anymore fulfilled for off-resonance energies. As the resonance phenomenon appears for the majority-spin and the minority-spin wave at different energies separated by the exchange splitting the precession angle $\varepsilon = \theta^{\downarrow} - \theta^{\uparrow}$ must necessarily exhibit a strong change as a function of electron energy. In fact, calculations made in the atomic limit for Fe do indeed predict a Ramsauer-Townsend effect for a scattering angle of 90° in the same energy

range as in our experiments [83]. We emphasize, however, that the situation in a crystal, which is the case here, is much more complex and requires a multiple-scattering approach to obtain realistic results. This is the mean reason for a full KKR calculation of the spin motion.

The strong sensitivity of the giant spin precession structure on little changes of the lattice parameter becomes plausible when we observe the behavior of both ε and I. Both experiment and theory show that the strength of the ε-structure is related to the strength of the intensity minimum, i.e., the more pronounced the intensity minimum the more pronounced the ε-structure (cf. Figs. 5.11 and 5.7). It is now important to understand that for small intensities $I^{\uparrow,\downarrow}$ ($=|r^{\uparrow,\downarrow}|^2$) a given change of $r^{\uparrow,\downarrow}$ leads to a much stronger variation of $\theta^{\uparrow,\downarrow}$ and thus in ε, than in the case where the intensities are larger.

5.4 Conclusion

Spin-polarized electron-reflection experiments on carefully prepared Fe films on Ag(001) show that the spin precession angle in reflection can reach its maximum possible value, namely 180 °. This marks the ultimate limit of spin manipulation in reflection. Our *ab initio* calculations strongly support our hypothesis that the relaxation of the Fe lattice during growth is responsible for this effect. Further studies have to be performed in order to show how the appearance of the strong ε-structure and its energy position could be modified in a ferromagnetic film by the choice of the substrate, its orientation or by alloying.

Chapter 6

Out-of-plane relaxation of the Fe surface due to MgO

Contents

6.1 Introduction

In the previous chapter we investigated the effect of bulk lattice relaxation on the spin-motion angles. A second type of lattice relaxation can be observed at the surface, where the surface atomic plane is rigidly displaced with respect to its bulk position and thus leading to an out-of-plane relaxation. The effect of the latter, viz. "Out-of-plane relaxation of Fe(001) covered by MgO" on the electron-spin motion, is discussed in this chapter.

The interface system MgO/Fe(001) has attracted great interest in the past for the very large tunnel magnetoresistance values, which have been predicted and observed in epitaxial Fe/MgO/Fe(001) magnetic tunnel junctions [84, 85]. In order to supply input for a correct modeling of these tunnel junctions, it is of great importance to explore the properties of the MgO/Fe interface. Only the knowledge of its electronic properties, in particular the spin-dependent reflection properties, will allow one to get a deeper insight into the microscopic mechanisms determining the tunnel magnetoresistance. A point of

crucial importance is thus the question how MgO influences the Fe surface and its spin-dependent properties. However, this is a quite controversial issue in the literature. While in some experiments no significant oxidation of the Fe interface layer was found [86, 87, 88], other experiments concluded on the formation of an FeO layer at the interface [4, 12, 89, 90, 92, 91]. Some of these latter studies point towards the more subtle point that the oxidation of the Fe surface takes place at the very onset of the MgO deposition when total MgO coverage is much lower than one monolayer [12, 92]. This, in fact, even more specifies the problem of whether the spin-dependent reflection properties of the Fe surface are already modified by the very first MgO coverage.

6.2 MgO on Fe

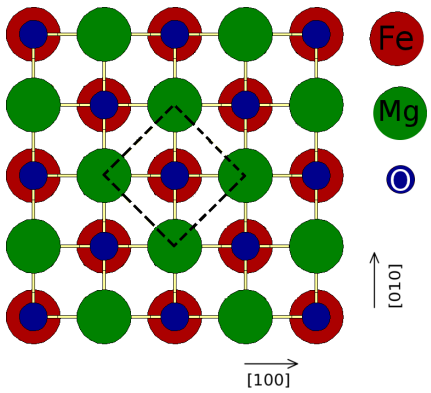

Figure 6.1: Atomic arrangement of the first MgO layer deposited on Fe(001). The unit cell of MgO is rotated 45° with respect to the unit cell of Fe..

MgO is an insulator that crystallizes in a cubic cell with a rock-salt structure and a lattice parameter of 0.421 nm. The crystal structure can be described by two face-centered cubic structures shifted by $(1/2, 0, 0)$ with respect to each other. The growth of Fe (001) on Ag is discussed in detail in Chapter 4. We present here the study of the growth mode of MgO/Fe(001).

MgO was deposited at room temperature at a rate of about 0.1 ML/min from pieces of stoichiometric MgO single crystals by electron-beam bombardment. All thicknesses are determined by a quartz microbalance. The oscillatory behavior of the reflection high-energy electron diffraction (RHEED) specular intensity as a function of MgO coverage (cf. Fig. 6.2 (left)) shows

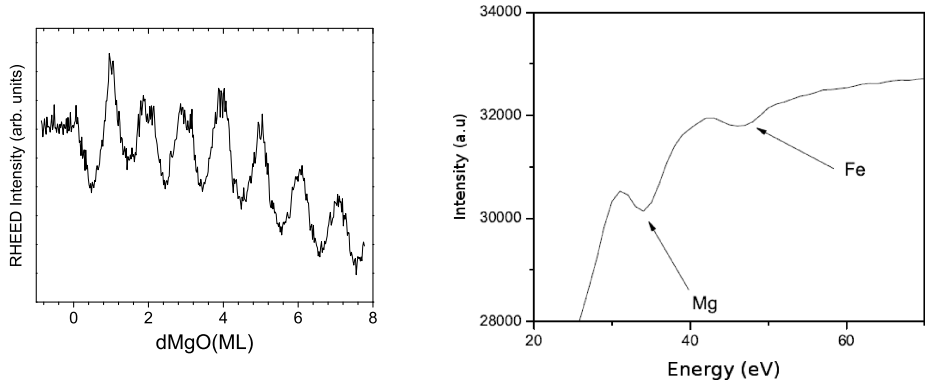

Figure 6.2: (Left) The RHEED intensity as function of the MgO coverage. (Right) Auger spectrum acquired on an energy range from 20 to 70 eV for 5 nm of Fe. Note the presence of two peaks corresponding to Mg and Fe.

that MgO grows on Fe(001) in a layer-by-layer fashion at least up to a thickness of 7 ML. Earlier STM work showed that MgO films of a few MLs are uniform in thickness with a quite small rms roughness [93]. We note that MgO films being thermally evaporated under ultra-high vacuum conditions from stoichiometric MgO are known to be nearly stoichiometric or slightly oxygen deficient [94].

Figure 6.2 (right) shows the results of Auger spectroscopic analysis of MgO/Fe(001) samples. At low energies there is a peak of Fe at 47 eV and a peak of Mg at 35 eV. Metallic magnesium normally exhibits a peak around 45 eV. However, the oxygen environment in MgO causes the peak to shift to 35 eV [95]. It is therefore impossible to identify a possible oxygen deficiency since no metallic Mg peak is detected. Therefore, all Mg atoms seems to be in an oxide environment.

6.3 Experimental results

Figure 6.3 (left) shows the spin-averaged electron reflectivity (R) as a function of the MgO thickness at a primary electron energy ($E - E_F$) of 7 eV. Two intensity maxima with ML-periodicity (1 ML = 0.22 nm) can be identified and attributed to periodic variations of the film morphology alternating between filled and incompletely filled atomic layers. For larger thicknesses, however, no further oscillations can be identified. It is evident that the two ML peaks

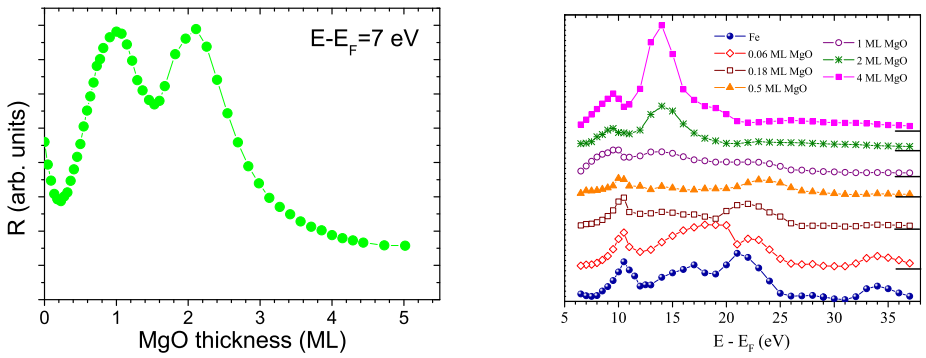

Figure 6.3: (Left) Spin-averaged electron reflectivity R as a function of MgO coverage at a primary electron energy ($E - E_F$) of 7 eV. (Right) Spin-averaged reflected intensity R as a function of the primary electron energy for different MgO coverages. The Fe film thickness is 4 nm.

are superimposed by a much broader structure having its center of gravity at around 1.6 ML. This structure is most likely due to the creation of a standing electron wave between the MgO surface and the MgO/Fe interface. In fact, such quantum-interference structures have already been observed in the same system [96]. They are usually explained by the phase accumulation model [97], in which constructive interference, i.e. a maximum in reflectivity, requires (for a given electron energy) the thickness of the film to fulfill a certain quantization condition.

Figure 6.3 (right) shows R as a function of electron energy for different MgO coverages. For high coverages, R is strongly enhanced in the energy region between 12 and 16 eV. This indicates the existence of a gap in the electronic band structure of MgO in this energy range. The fact that this maximum in R can already be identified at the same energy position for a coverage of 1 ML, suggests that the electronic band structure of MgO in the considered energy regime approaches already its bulk form for coverages as small as 1 ML.

Figure 6.4 (left) shows ε and ϕ as a function of MgO coverage for $E-E_F$ of 7 eV. Already 0.15 ML of MgO are sufficient to halve ε and even change sign of ϕ. Interestingly, ϕ approaches zero less rapid than ε. For coverages above 0.5 ML both quantities are 90° out-of-phase, i.e. ϕ exhibits its strongest change when ε is in its minimum and vice versa. We attribute the structures at 0.9

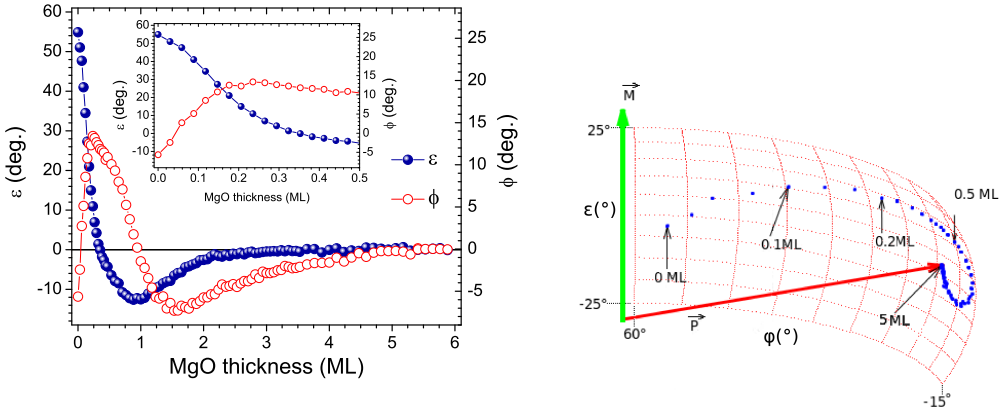

Figure 6.4: (Left) Precession angle ε and rotation angle ϕ as a function of MgO coverage. The inset highlights the low-coverage regime. The primary electron energy is $E-E_F = 7\,\text{eV}$. The Fe film thickness is 6 nm. (Right) The spin polarization direction as function of MgO thickness with primary electron energy of $E - E_F = 7\,\text{eV}$

ML for ε and at 1.5 ML for ϕ to the appearance of a quantum interference in the MgO film by Wu *et al.* [96]. In these experiments, a spin-polarized low-energy electron microscope has been used to evidence oscillations of the electron reflection spin-asymmetry both as a function of MgO coverage and as a function of electron energy for a given MgO thickness. However, the regime of very low MgO coverages has not been studied. As we find a drastic effect on the spin-polarization direction of the reflected electrons for very small coverages (cf. Fig. 6.4 (right)), i.e. ε and ϕ are very sensitive to small coverages of MgO, we focus therefore on the range below 1 ML.

Figure 6.5 shows ε (top) and ϕ (bottom) as a function of $E - E_F$ for different MgO coverages. For small coverages (up to 0.18 ML) we find different behaviors depending on the energy range. While a strong reduction of ε with MgO coverage is found in the energy range from 7 to 9 eV and from 32 to 38 eV, a relatively strong increase is observed between 13 and 17 eV. For all other energies the changes are relatively small. In the case of ϕ the situation is quite similar with the exception that between 27 and 31 eV ϕ is strongly reduced, while ε does not change significantly. Finally, for MgO coverages larger than 4 ML both spin-motion angles are practically zero for all energies (see insets in Fig. 6.5). This is due to a small electron inelastic mean free path of about 2-3 ML of MgO in this energy range.

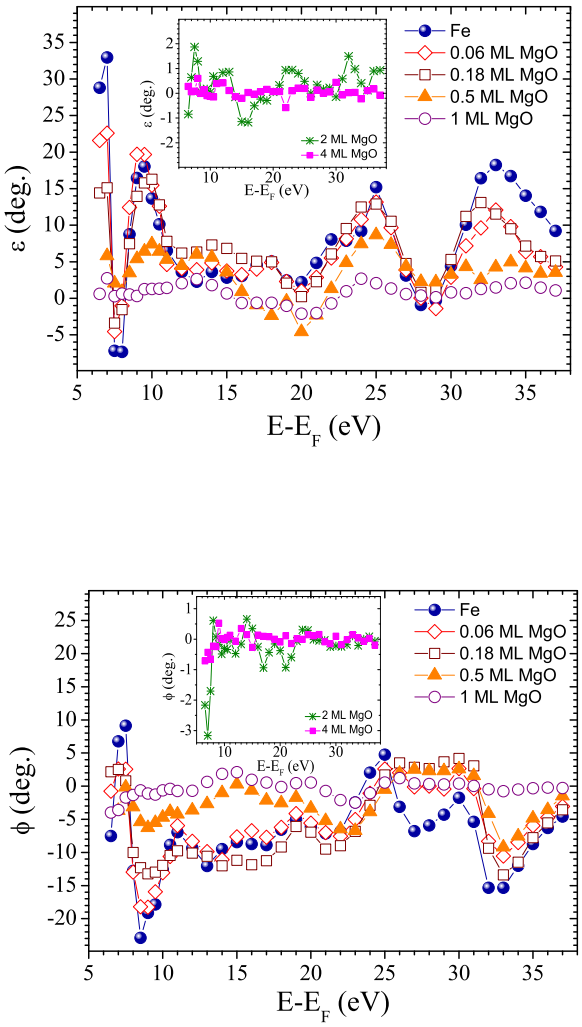

Figure 6.5: Precession angle ε (Top) and rotation angle ϕ (Bottom) as a function of the primary electron energy for different MgO coverages

6.4 Discussion

A possible origin of the strong sensivity of the spin motion angles is a change of the surface magnetism during MgO deposition. Many studies of ferromagnetic thin films show the existence of magnetically "dead layers", on which the magnetic moment is zero or at least reduced relative to the bulk value [99, 100]. Such layers exist usually at the interface and their existence is generally due to the formation of an alloy or the presence of adsorbates modifying

the magnetic properties of the ferromagnetic material.

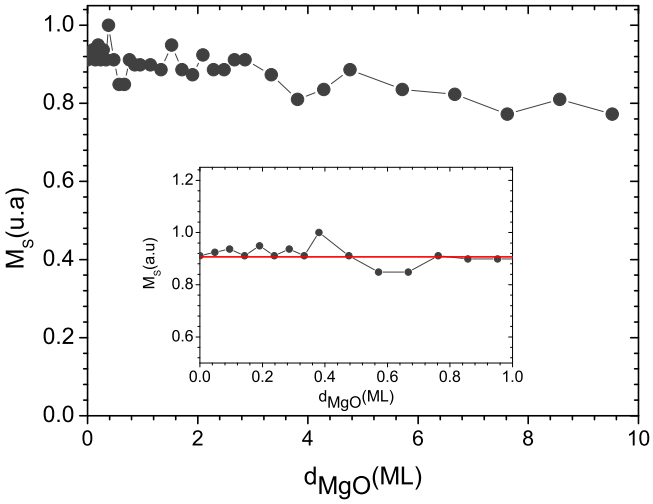

Figure 6.6: The magnetization saturation M_S as function of the MgO coverages deposited on 6 ML Fe. For high-coverages M_S is reduced due to the attenuation of light in MgO.

In order to exclude a possible change of the surface magnetism during MgO deposition or the existence of a dead layer, a thin Fe film of 6 ML thickness has been prepared and measured by the magneto-optical Kerr effect as a function of MgO coverage (cf. Fig. 6.6). In particular, in the sub-monolayer coverage regime Kerr measurements show no significant changes of the saturation magnetization (see inset Fig. 6.6). If there were one or more magnetically dead layers we would notice a drastic decrease in the signal. Moreover, both experiments [88] and calculations [101] have shown that the Fe magnetic moment at the MgO/Fe interface is rather enhanced (by about 35 %) than reduced. Our own calculations, showing a magnetic moment of $3\,\mu_B$ at the interface, i.e. an enhancement of 36 %, are in very good agreement with these findings. Thus the behavior of ε and ϕ in the sub-monolayer regime can not be explained by a change of the magnetic properties of Fe.

Since a strong modification of the magnetization is excluded, we assume that the origin of this strong sensitivity of the spin-motion angles on the MgO coverage is an out-of-plane relaxation (expansion) of the Fe surface layer induced by MgO which is much stronger than the out-of-plane relaxation (compression) of about -1 % which exists already for the uncovered Fe surface [102]. This in turn would result in a change of the Fe electronic structure

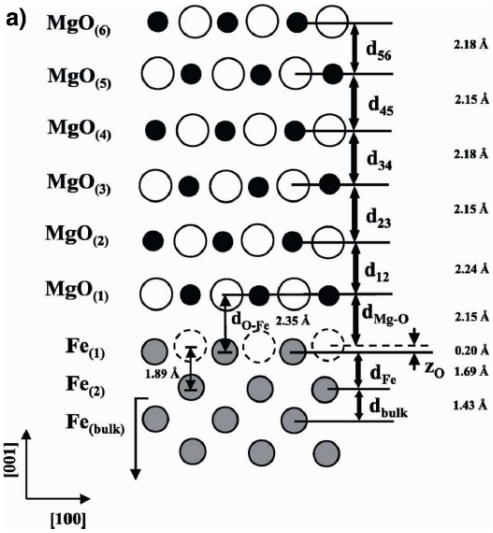

b)

	d_{Fe}	$d_{O\text{-}Fe}$	$d_{Mg\text{-}O}$	z_O	d_{12}	d_{23}	d_{34}	d_{45}	d_{56}
Coverage									
0.35 ML	1.57	2.21	1.95	0.25					
0.98 ML	1.63	2.43	2.09	0.23	1.90				
2.12 ML	1.66	2.35	2.14	0.17	2.26	2.09			
3.22 ML	1.69	2.35	2.15	0.20	2.18	2.15	2.18		
4.65 ML	1.69	2.35	2.15	0.20	2.24	2.15	2.18	2.15	2.18

Figure 6.7: a) Modeling the growth of MgO/Fe(001). The MgO deposition induces the formation of a Fe-O layer at the interface, which leads to the out-of-plane relaxation of the first Fe layer. b) interplane distance as a function of the MgO thickness. 0.35 ML of MgO is sufficient to induce 10 % out-of-plane relaxation of the first Fe layer. From [12]

leading to a change of the spin-dependent reflection properties. In fact, surface x-ray diffraction experiments found that the first Fe interlayer distance is expanded up to 18 % relative to the bulk value (0.143 nm) due to MgO coverage [12]. Most importantly, already a sub-monolayer coverage of 0.35 ML induces a significant relaxation of 10 % (cf. Fig. 6.7). Furthermore, the same experiments gave also clear evidence for the presence of a sub-stoichiometric Fe-O layer between the Fe substrate and the MgO layers and it is this Fe-O layer which is believed to be responsible for the strong expansion of the first Fe interlayer distance. This leads us to question whether oxygen coverage of the Fe surface alone would lead to a similar behavior of the spin-motion. Indeed, measurements at an electron energy of 7 eV, for which in the case of MgO strong changes are seen, show that both spin-motion angles exhibit also a strong decrease with oxygen coverage (cf. Fig. 6.8). Already $\sim$ 0.1 ML of oxygen is sufficient to halve both ε and ϕ. This strongly suggests that the O-Fe bonds within the surface layer, which also lead to an out-of-plane relaxation of the Fe surface layer [103], determine the spin-dependent reflection properties. We emphasize that for such small oxygen coverage the magnetization of Fe(001) films is not influenced [80]

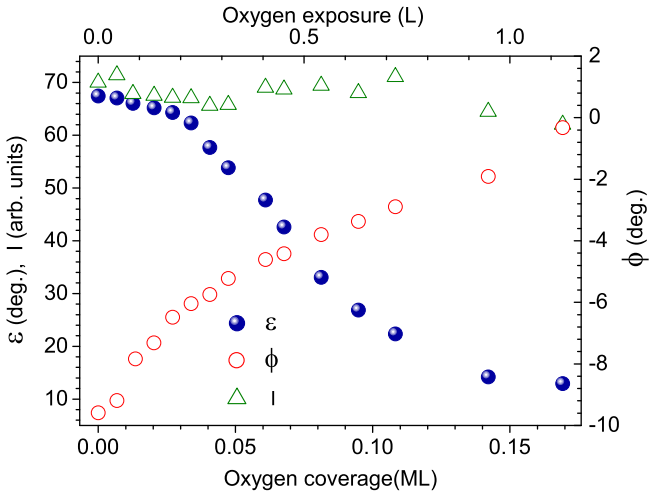

Figure 6.8: Precession angle ε and rotation angle ϕ as a function of the oxygen coverage (bottom scale) and the exposure in Langmuir (L ; 1 L = 10^{-6} Torr.s) (top scale). The data of Sakisaka *et al.* [104], which provide a relation between the exposure and the coverage, were used to translate exposures into coverages. The primary electron energy is $E - E_F = 7\,\text{eV}$. The Fe film thickness is 40 ML.

6.5 Theoretical confirmation

From the preceding we have learned that the electron spin-motion angles depend strongly on MgO coverage and might be explained by the out-of-plane relaxation of the Fe surface layer. To prove this assumption we performed calculations for uncovered Fe in which the out-of-plane lattice constant of the surface layer has been varied. We emphasize that the calculations were focused on the most prominent spectroscopic structure in the energy range from 7 to 9 eV. For higher energies no comparison is made with theory because due to the limited wave function basis-set of the linear muffin-tin orbital (LMTO) method the determination of the electronic structure at higher energies is not very reliable. We emphasize, however, that the LMTO method was used only to provide the self-consistent potential of the relaxed Fe surface. The relaxation is done using the full-potential linear augmented plane wave (FLAPW) method. We have checked that the electronic band structure produced by the LMTO method is to a high accuracy similar to that produced by the FLAPW method. We have then taken the converged potentials and used them to compute the spin motion upon reflection using the Green's function formalism within the

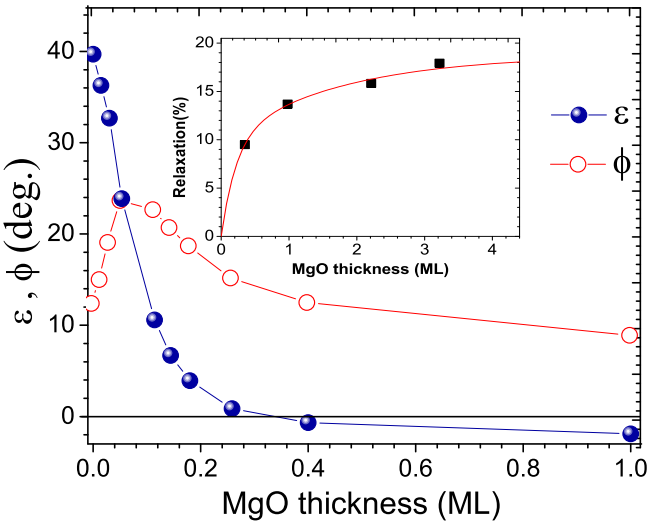

Figure 6.9: Calculated ε and ϕ as a function of MgO coverage for $E - E_F = 7\,\text{eV}$. The inset shows the relation (line) between the degree of relaxation and the MgO thickness, obtained by fitting an exponential to the experimental data (dots) of Meyerheim *et al.*[12]

Korringa-Kohn-Rostoker (KKR) method.

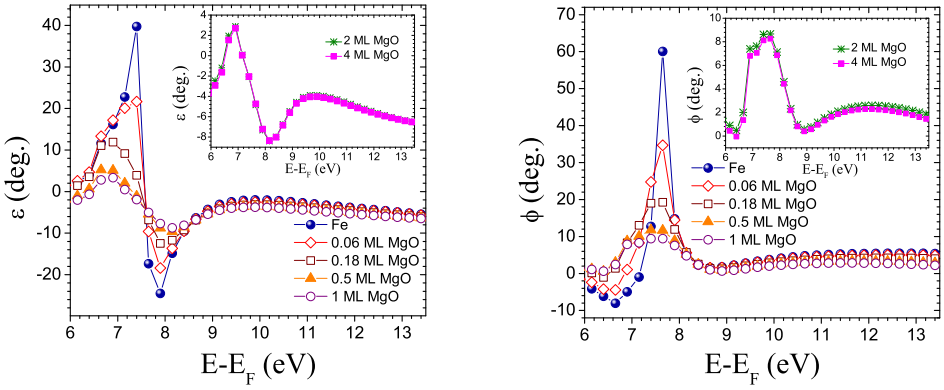

Figure 6.10: Calculated Precession angle ε (Left) and rotation angle ϕ (Right) as a function of the primary electron energy for different MgO coverages

To compare the calculations with the experimental data as a function of MgO coverage, the x-ray data of Meyerheim *et al.* [12], which provide a relation between the MgO thickness and the strength of the out-of-plane relaxation (see inset in Fig. 6.9), were used to translate the values of the

out-of-plane relaxation in our calculations into MgO thickness values. Figure 6.9 shows the calculated spin-motion angles as a function of MgO coverage and figure 6.10 show them as a function of primary electron energy for different MgO thicknesses. By comparing Fig. 6.9 and 6.10 with the experimental data in Fig. 6.4 and 6.5 we note a qualitative agreement with experiment. This leads us to the conclusion that the change of the Fe interlayer distance is indeed responsible for the behavior of the electron-spin motion upon reflection. We emphasize that a better agreement cannot be expected, since there is no scattering at MgO in the model calculations. The effect of MgO is taken into account only via the relaxation of the surface Fe layer. Consequently, also the effect of quantum-well states in the MgO layer as well as that of the inelastic mean free path of the electrons in MgO are ignored in the calculations. Our next attempt was to investigate whether this behavior

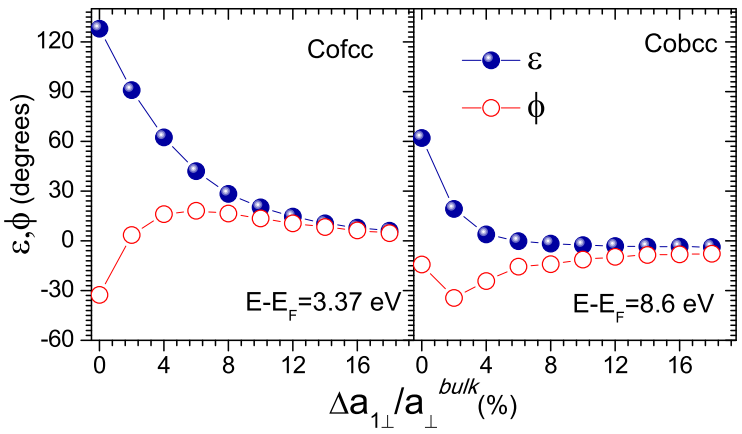

Figure 6.11: Calculated ε and ϕ as function of the out-of-plane relaxation.(left) is in the case of fcc-Co(001) at $E - E_F = 3.37\,eV$ primary electron energy. (right) in the case of bcc-Co(001) at $E - E_F = 8.6\,eV$.

is only observed for Fe films or whether it could be found also for other ferromagnetic materials. SPLEED calculations were performed on fcc-Co(001) and bcc-Co(001) by varying the interlayer distance of the Co surface. In both cases, the electron-spin motion was found to be very sensitive to the out-of-plane relaxation, where already a 2 % change can lead to a strong change in ε and ϕ (cf. Fig.6.11).

6.6 Conclusion

In conclusion, the interface system MgO/Fe(001) was studied by spin-polarized electron reflection experiments as a function of the MgO coverage, as well as a function of the primary electron energy. A very strong sensitivity of the spin-motion angles ε and ϕ on the MgO coverage was observed for certain energy ranges. Magneto-optical Kerr effect experiments did not show any strong change of the Fe surface magnetism during MgO deposition, and therefore no such effect is at the origin of these strong variations of the spin-motion angles. Indeed, the qualitative agreement of our *ab initio* calculations with the experimental data suggests strongly that the out-of-plane relaxation of the Fe surface layer, induced by MgO, is responsible for this behavior and predict similar behavior in fcc-Co(001) and bcc-Co(001). The present findings underline the importance of details of the interfacial structure for the spin-dependent reflection properties.

Part IV

Transport results

Chapter 7

Transport properties and interface relaxation

Contents

7.1 Introduction

From the previous part we learned that the spin-dependent reflection is very sensitive to the MgO/Fe(001) interface relaxation. These results make us wonder how the out-of-plane relaxation effects the spin-dependent transmission in the Fe/MgO/Fe magnetic tunnel junction (MTJ). In this chapter we will try to answer this question. In the beginning, a small section introduces the history of Fe/MgO MTJ and highlights the importance of the system. Then we present a brief section about the *ab initio* calculation used in this work. Finally, we present and discuss our results.

7.2 Fe/MgO/Fe magnetic tunnel junction

TMR may be regarded as the new candidate for mesoscopic scale magnetic sensors and magnetic random-access memory (MRAM) elements, where TMR based spintronic devices have many advantages over GMR devices for two reasons. First, they are easier to fabricate. Second, they can provide much larger signal. Indeed, recently significant TMR values have been observed, up to 600 % at room temperature and more than 1000 % at 5 K in junctions of CoFeB/MgO/CoFeB [29]. The tunnel barriers of MgO attracted attentions since 2001, when Butler and Mathon [3, 84] predicted independently that the TMR can reach several thousand percent in Fe/MgO/Fe. However, experimentally the highest value observed in such system is around 200 % at room temperature [14]. This disagreement between theory and experiment stimulated many researchers to investigate the reason behind it. In the following investigation of the electronic structure of MgO and Fe is given to understand the origin of high tunneling magneto-resistance (TMR).

7.2.1 Relevance of Fe/MgO system

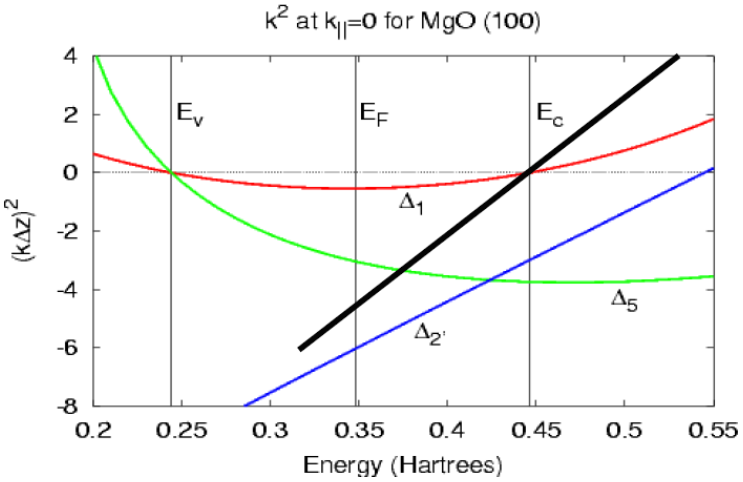

Figure 7.1: The electronic states of different symmetries decay with different rates within the MgO barrier in $k_{\|} = 0$ direction. Δ_1 state has the smallest decay rate compared to the other symmetries and is therefore supposed to carry the tunneling current in the barrier.

A good approach to understand the spin-dependent transport in tunnel junctions is provided by theoretical studies, which claim that the spin de-

pendence of the tunneling current can be deduced from the symmetry of the electronic states of the bulk ferromagnetic electrode and the complex band structure of the insulator. Therefore, by identifying the evanescent states of Fe that decay most slowly within the barrier, one can predict the sign and magnitude of the spin polarization of the tunneling current. This will help to understand the high TMR ratio in Fe/MgO/Fe. In order to identify those ferromagnetic states, which are mainly involved in the tunneling process within the barrier, one has to find the wavevector k in the electronic band structure at which the exponential decay of the electronic states inside the barrier will be the slowest.

It was found that the exponential decay is minimal for the direction $k_{\|} = 0$ [84]. Therefore, one has to identify the states in the ferromagnetic electrodes which exist at $k_{\|} = 0$, because these states will couple to states in the MgO barrier with a minimal decay rate. The symmetry of the incident electronic states of the ferromagnetic electrode is conserved during tunneling through the barrier as evanescent states. At the Fermi level for the majority electrons we have the following states: Δ_1 (spd-like character), Δ_5 (pd) and Δ_2' (d). For the minority electron we have: Δ_2, Δ_5 and Δ_2'. Due to the exchange splitting, there is no Δ_1 state for the minority spin. Therefore, one can conclude that the Fe behaves as a half-metal system in terms of the Δ_1 symmetry.

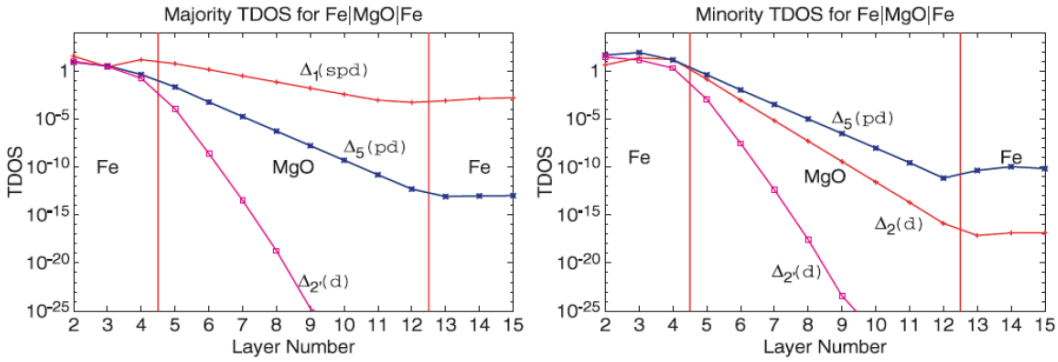

Figure 7.2: Tunneling DOS for $k_{\|} = 0$ in a Fe/MgO/Fe(001) junction, in which the magnetization of the ferromagnetic electrodes is aligned parallel. The Δ_1 majority state has the slowest decay inside the MgO barrier and thus contributes dominantly to the tunnel current. From [105]

The decay rates for all the states are given by the complex energy bands of Figure 7.1. k^2 represents the Bloch state quasi-momentum in the complex

MgO band structure, which is plotted as a function of the energy for states traveling along the [100] direction. The negative values of k^2 determine the strength of the exponential decay rate for the tunneling states. E_v and E_c labels the top of the MgO valence band and the bottom of the conduction band, respectively. Whereas the valence band is a combination of Δ_1 and Δ_5 states, the conduction band is a pure Δ_1 state. Fig. 7.1 shows that incident wave functions of different symmetries will decay at different rates within MgO barrier. In particular, incident states with Δ_1 symmetry are transmitted with much higher probability than other symmetries. Thus MgO can act as a symmetry filter if it is epitaxial on an electrode and the two-dimensional symmetry is maintained at the interface.

As mentioned above, bcc-Fe(100) has a high symmetry Δ_1 state at $k_{\|} = 0$ for the majority states, but not for the minority states. This is due to the strong exchange splitting between the $\Delta_1^{\uparrow}$ and $\Delta_1^{\downarrow}$ bands. Therefore it is possible to use Fe with MgO to take advantage of MgO symmetry filtering effect to make a spin-filter device. Figure 7.2 helps understanding why Δ_1 majority conductance is larger compared to all other symmetries in a Fe/MgO/Fe tunnel junction. From symmetry arguments [3, 84], one expects to have a large value of TMR for epitaxial Fe/MgO/Fe junction.

7.2.2 Effect of interface oxidation on transport properties

Transport calculations for well ordered interfaces on Fe/MgO/Fe, predict TMR ratios that exceed thousand percent. Although experimental TMR ratios for Fe/MgO/Fe have increased over the years there is still a disagreement between theoretical and experimental values. The experimental TMR ratios are limited to values at least one order of magnitude smaller than their theoretical counterparts. In the past few years many experimental and theoretical efforts were aimed at understanding this limitation. Real MTJs actually deviate from ideal ones considered in theoretical models: the structural defects are suspected to reduce the filtering efficiency and therefore the magnetoresistive response. This reduction is usually ascribed to the presence of an FeO layer at the Fe/MgO interface.

In the last few years, many transport calculations [1, 106, 107] and experimental [91, 92] suggest that oxygen concentrations at the interface re-

duces considerably the tunnel magnetoresistance of Fe/MgO/Fe junctions. In particular, the formation of FeO layer reduces the tunneling current of the majority spins and this reduction is mainly ascribed to the modification of the interface bonding. However, recent experiments [108, 109] showed that Fe-O bonds reduce the TMR slightly and not dramatically as shown by theory. This clearly means that any oxygen contamination during the process of Fe/MgO/Fe growth is not as harmful to the TMR amplitude as suggested by the calculations. The effect of interfacial oxidation on the transport properties remains controversial due to the disagreement between theory and experiment. Therefore, the limitation of the experimental TMR values in Fe/MgO/Fe system cannot be strictly attributed only to interfacial oxygen contamination.

In summary the interface oxidation is not directly responsible for the low TMR value found in the experiment. However, we should keep in mind that small amounts of interface oxidation can lead to strong interlayer expansion between the last Fe layers. Indeed spin-polarized electron reflection experiments showed that a 0.1 ML coverages of O is sufficient to have a drastic effect on the spin motion angles. As a consequence, the out-of-plane relaxation induced by the Fe-O layer is a plausible candidate to explain the low TMR values obtained in experiments. To verify this hypothesis we performed *ab initio* calculation of the transport properties as function of the out-of-plane relaxation.

7.3 Transmission calculation

The calculation was done for the equilibrium configuration i.e. in the linear response theory regime of vanishing bias. The Landauer formalism is used to compute the electrical conductance. The details of the method can be found in reference [110]. Landauer associated the conductance of a MTJ with the quantum mechanical transmission probabilities of the one electron wave function as it approaches an arbitrary scattering potential. The Landauer formalism is based upon several assumptions such as:

1. The electrodes are connected to semi-infinite electron reservoirs that can donate (accept) arbitrary number of electrons without any change to its internal state.

2. The electrodes must be both in thermal equilibrium.

3. The electrons in the total system (reservoirs + junctions) are considered to be non-interacting electrons.

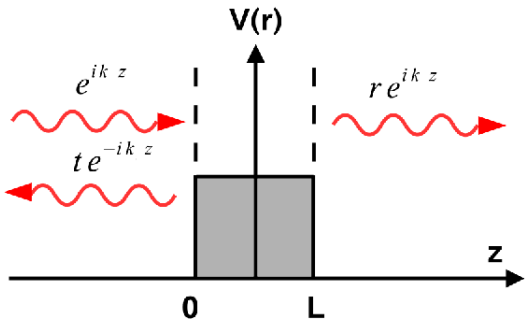

Figure 7.3: Schematic representation of incoming and outgoing wave functions scattered by a potential $V(r)$.

Let us consider the case of periodic one dimensional wire. In this case the problem can be formulated in terms of incoming $|\Phi_{in}\rangle$ and outgoing $|\Phi_{out}\rangle$. The electron wave functions propagating along the one dimensional wire (scattering channel) are scattered by a potential connecting the two leads. Due to the periodic nature of the wire, these wave functions have the form of Bloch waves and in absence of a scattering potential, each one contributes by $G_0 = 2e^2/\hbar$ to the total conductance. Thus the scattering channel can be defined as the asymptotic part of the wave function deep inside the leads. In the case of multi-dimensional system, several possible Bloch waves with the same energy can propagate through the leads. Once the i-th channel in the left hand-side reaches the scattering region it can be transmitted to any channel into the right hand-side lead or back scattered into any channels of the left hand-side lead.

Figure 7.3 provides a simple example of the transport problem formulated in terms of in-scattering and out-scattering channels: free electrons with energy E are injected from the left and are scattered by a step potential

$$V(z) = \begin{cases} V & , \quad 0 < z < L \\ 0 & , \quad \text{elsewhere} \end{cases} . \tag{7.1}$$

An incoming electron with wave-vector k_z is partially backscattered with wave-vector $-k_z$ and partially transmitted. The total wave function for this problem reads

$$|\Phi_{total}\rangle = |\Phi_{in}\rangle + |\Phi_{sc}\rangle + |\Phi_{out}\rangle, \tag{7.2}$$

with

$$\langle z|\Phi_{total}\rangle = \begin{cases} \langle z|\Phi_{in}\rangle & = e^{ik_z z} + re^{-ik_z z} & 0 \leq z \\ \langle z|\Phi_{sc}\rangle & = Ae^{\kappa_z z} + Be^{-i\kappa_z z} & 0 \leq z \leq L \\ \langle z|\Phi_{out}\rangle & = te^{ik_z z} & z > L, \end{cases} \tag{7.3}$$

where the wave-vector k_z is given by

$$k_z = \frac{\sqrt{2mE}}{\hbar}, \tag{7.4}$$

whereas

$$\kappa_z = \frac{\sqrt{2m(V-E)}}{\hbar}, \tag{7.5}$$

can be real (evanescent) or imaginary (propagating) depending on whether $V > E$ or $V < E$, respectively. The coefficients A, B, t and r are determined by imposing the continuity of the total wave function and its derivative at the boundaries of the step potential.

Alternatively the scattering process can be described in terms of the scattering matrix, S, which relates the wave function of the incoming and outgoing electrons with respect to the step potential

$$|\Phi_{in}\rangle = S|\Phi_{out}\rangle \tag{7.6}$$

where

$$S = \begin{pmatrix} r & t' \\ t & r' \end{pmatrix}, \tag{7.7}$$

and t and r are the transmission and reflection coefficients, respectively, for incoming waves from the left whereas t' and r' are the counter parts for incoming waves from the right. In the more general multi-channel problem r, t, r' and t' are matrices. The total conductance is defined by Landauer as

$$G = \frac{e^2}{h} \sum_{\sigma} \sum_{ij}{}' T_{ij}^{\sigma} = \frac{G_0}{2} \sum_{\sigma} Tr[t_\sigma t_\sigma^\dagger], \tag{7.8}$$

where $\sum_{ij}'$ indicates that the sum is performed over all channels at the Fermi energy (E_F) (the open channels) and we have introduced the spin index σ. We can clearly see that the conductance is written in terms of the conductance quantum G_0. Most importantly we note that the conductance has been directly associated with the coefficients of the out-scattered wave functions of our simple problem. Hence the energy-dependent transmission probability is

$$T^\sigma(E) = Tr[t_\sigma(E) t_\sigma^\dagger(E)]. \tag{7.9}$$

Finally, if we define R_{ij} as the total probability for the i-th channel to be reflected into the j-th channel, we obtain from the particle conservation requirement the following relations:

$$\sum_j (R_{ij} + T_{ij}) = 1 \text{ and } \sum_{ij} (R_{ij} + T_{ij}) = M, \tag{7.10}$$

where M is the number of channels at the Fermi level.

As mentioned earlier, the Landauer formalism is based upon a series of approximations which makes it incompatible with actual experimental results. However, the non-interacting electrons approximation can be removed using non-equilibrium Green's function (NEGF) technique. The transmission values of Fe/MgO/Fe tunnel junctions were calculated within an *ab-initio* electronic transport code based on a combination of density functional theory (DFT) and non-equilibrium Green's function transport methods (NEGF) SMEAGOL (spin and molecular electronics in atomically-generated orbital landscapes) [111, 112, 113]. The Kohn-Sham equations are solved in the NEGF scheme and the electric conductance is then obtained from the Landauer formula.

7.4 Transport results

Recent experiments [114] reported the observation of an interface asymmetry in Fe/MgO/Fe(001) tunnel junctions due to a formation of an Fe-O layer at only one interface. Based on this information the transmission coefficients were calculated within GGA (generalized gradient approximation) for four types of crystal structures. The first one has ideal Fe/MgO interfaces without oxidation. The in-plane lattice constant was fixed to the experimental value for bulk bcc-Fe, $a = 2.866\,\text{Å}$. However, the Fe-Fe interlayer distances next to the interfaces are varied from bulk Fe of $1.433\,\text{Å}$ up to $1.7\,\text{Å}$. The remaining Fe layers are separated as in Fe bulk. The distance between the interface Fe layer and the O in the the first MgO layer is fixed to $2.35\,\text{Å}$. The first and the second MgO layers are separated by $2.24\,\text{Å}$, whereas the distance between the second and third MgO layer is $2.15\,\text{Å}$, which is close to the bulk value of MgO.

In the second junction both interfaces consist of an FeO layer. The system remains symmetric and in the following this label will be used to distinguish between the three geometries, despite the fact that the ideal junction geom-

etry is symmetric, too. The oxygen atoms are placed close to the octahedral vacancy position shifted outward by 0.2 Å, so that the distance between these atoms and the next Mg atoms is 2.15 Å. In this study, the in-plane periodicity was kept, and all oxygen sites were occupied. Partial occupancy of the FeO layer by the oxygen atoms is not discussed here. The Fe-FeO interlayer distances next to the interfaces are also varied as in the first situation.

The third crystal structure under consideration is an asymmetric structure which contains both the ideal and the FeO interface. The fourth and the final crystal structure is also asymmetric but with no direct presence of Fe-O layer. The presence of Fe-O layer was modeled by the out-of-plane relaxation at one interface and not both. Thus only at one interface the interlayer distance is varied whereas the second is kept constant at the bulk Fe value.

The reason for performing the calculation for oxidized and non-oxidizes Fe layers is to highlight the effect of relaxation and to compare the results in both cases. In the following the obtained results are presented and divided into two main situations, symmetric and asymmetric.

7.4.1 Symmetric case

At zero bias the conductances G were obtained from the transmission coefficients calculated at the Fermi energy $T(E_F)$. Thus $G = e^2/hT(E_F)$ where e is the electron charge, and h Planck's constant. The transmission coefficient $T(E_F)$ were calculated within the GGA and by varying the Fe-Fe interlayer distances near the interface. The interlayer distances were varied from the bulk value of 1.433 Å (0 %) to 1.7 Å (18 %) in steps of 2 % .

Figure 7.4 shows $G^{P/AP}_{maj/min}$ as a function of the interlayer expansion. In the case of the ideal interface Fe/MgO/Fe (Fig 7.4 (left)), G^{P}_{maj} increases linearly with increasing relaxation whereas G^{AP}_{maj} [1] decreases also linearly. In other words, the tunneling probability for the majority electrons in the case of parallel alignment increases with relaxation while in the anti-parallel alignment it decreases. One might note that G^{P}_{maj} behavior is similar to G^{AP}_{maj} except for a jump around $\Delta a_{1\perp}/a^{bulk}_{\perp} = 6\,\%$, where $\Delta a_{1\perp} = a_{1\perp} - a^{bulk}_{\perp}$ with $a_{1\perp}$ the Fe-Fe interlayer distance near the interface and $a^{bulk}_{\perp}$ the Fe bulk lattice parameter (equal to 1.433 Å). In the case of an oxidized interface,

[1] Because of the assumed symmetry, the majority and minority channel conductances are the same for the anti-parallel alignment.

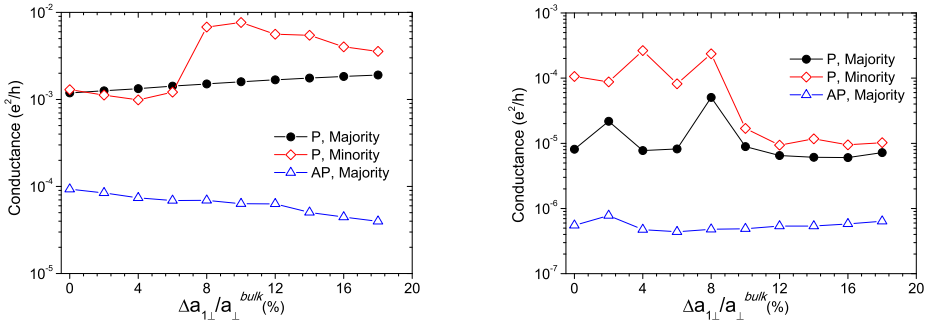

Figure 7.4: The spin-dependent conductance for symmetric Fe/MgO/Fe MTJ as function of the out-of-plane relaxation for the parallel configuration (P) and anti-parallel configuration (AP). The left curves are for the case of non-oxidized interfaces and the right for the oxidized ones.

Fe/FeO/MgO/FeO/Fe structure (Fig 7.4(right)), the spin-dependent transmission in general is lower than in the ideal case as expected. Similar to the ideal case, the G^P_{min} is the channel with the larger contribution. For larger relaxation, above $\Delta a_{1\perp}/a^{bulk}_{\perp} = 10\,\%$, G^P_{maj}, G^P_{min} and G^{AP}_{maj} are parallel and linearly increase with increasing Fe-FeO interlayer-distances. However, for smaller relaxation, the behavior of G^P_{maj} and G^P_{min} is more complex with abrupt changes around 2 %, 6 % and 8 % of interlayer relaxation. However, G^{AP}_{maj} shows a less abrupt change in the lower relaxation regime.

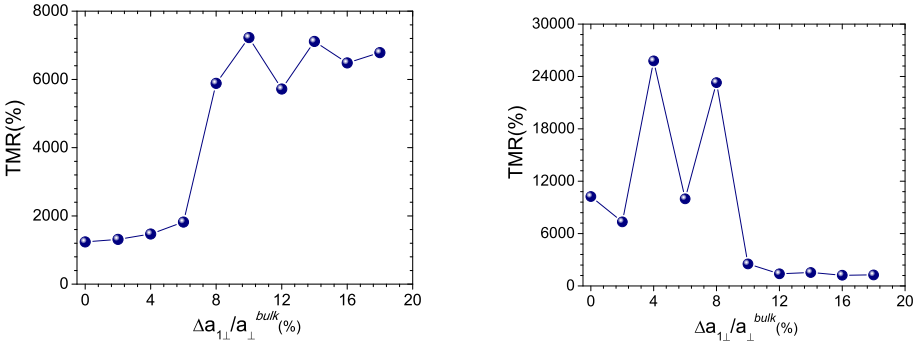

Figure 7.5: Dependence of the TMR of symmetric Fe/MgO/Fe MTJ over the out-of-plane relaxation for two different interfaces, non-oxidized (left), oxidized (right).

The calculated conductances where used to determine the TMR magnitude as a function of the interlayer expansion. The magnitude of the TMR is defined

as following:

$$TMR = \frac{G^p - G^{ap}}{G^{ap}}, \tag{7.11}$$

where $G^p = G^P_{maj} + G^P_{min}$ and $G^{ap} = G^{AP}_{maj} + G^{AP}_{min}$ are the total conductance for parallel and anti-parallel configurations, respectively.

Figure 7.5 shows the calculated TMR magnitudes for Fe/MgO/Fe (left) and Fe/FeO/MgO/FeO/Fe (right) symmetric MTJs. The TMR curves apparently follow the behavior of the minority transmission probabilities shown previously. For Fe/MgO/Fe, the TMR has a value of 1300 % for non-relaxed interfaces, and increases up to 2000 % for 6 % expansion. However, following G^P_{min}, the TMR jumps to 6000 % at 8 %. In the Fe/FeO/MgO/FeO/Fe case the situation is quite the opposite. The TMR magnitude is very large for small relaxation and decreases for large relaxation values to the typical theoretical values. Similar to G^P_{min} the TMR curve shows some peaks at 4 % and 8 % where it reaches values of 25000 %.

7.4.2 Asymmetric case

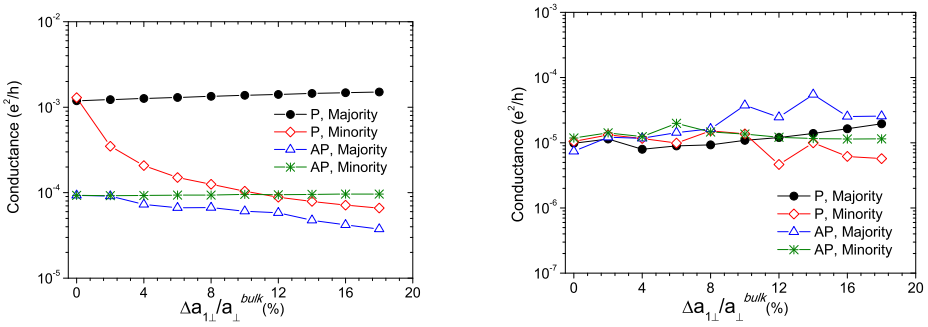

Figure 7.6: The spin-dependent transmission coefficient for asymmetric Fe/MgO/Fe MTJ as function of the out-of-plane relaxation for the parallel (P) and anti-parallel configurations (AP). The left curves are for the case of non-oxidized interface and the right for the oxidized one.

In the following the asymmetric calculation is presented. As in the symmetric case $G^{P,AP}$ were obtained for asymmetric interfaces Fe/MgO/Fe and Fe/FeO/MgO/Fe. Similar to the symmetric case, the interlayer distance was varied from 0 % to 18 % in steps of 2 % for the first interface, whereas the

interlayer distances in the second interface were not relaxed during the calculation.

Figure 7.6 shows $G^{P/AP}_{maj/min}$ as a function of the interlayer expansion. In the case of asymmetric Fe/MgO/Fe MTJ (Fig 7.6 (left)), G^{P}_{maj} and G^{AP}_{min} are parallel. Note that in the anti-parallel configuration the two spin channels behave differently, i.e. by breaking the symmetry one can differentiate between the two spin channels. The behavior (if not the values) of G^{P}_{maj} (G^{AP}_{min}) in the asymmetric case is exactly similar to that in the symmetric one. Contrary to the symmetric situation, where G^{P}_{min} had the main contribution to the tunneling current, G^{P}_{maj} in the asymmetric control the behavior of the tunneling current in the parallel configuration. For higher relaxation values, G^{P}_{min} and G^{P}_{maj} are parallel like in the symmetric case. However, for small relaxation G^{P}_{min} decreases exponentially as a function of out-of-plane relaxation.

For Fe/FeO/MgO/Fe MTJ, the tunneling currents for different channels are quite close to each other. G^{P}_{min} and G^{AP}_{min} are parallel showing no significant changes, except for high relaxation values where G^{P}_{min} changes abruptly. Similarly, the tunneling current for the majority channels are parallel with a slight increase in magnitude with increasing relaxation.

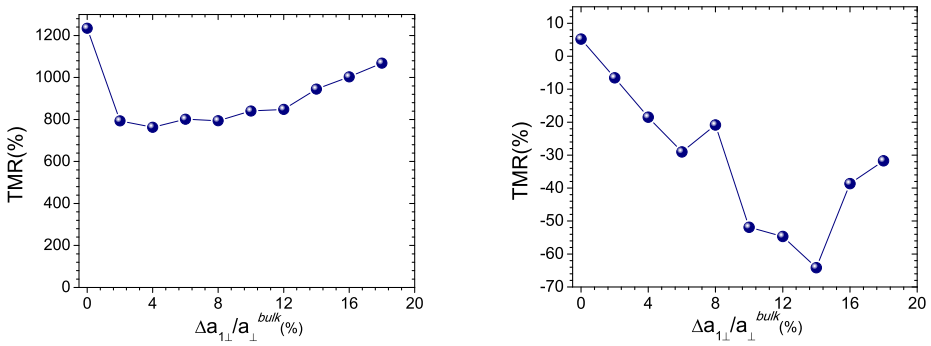

Figure 7.7: Dependence of the TMR of asymmetric Fe/MgO/Fe MTJ over the out-of-plane relaxation for two different interfaces, non-oxidized (left), oxidized (right).

The calculated TMR for the asymmetric case shows lower values than that of the symmetric ones. Figure 7.7 shows the magnitude of the TMR for Fe/MgO/Fe (left) and for Fe/FeO/MgO/Fe MTJs. In the first case, Fe/MgO/Fe, the TMR drops drastically by 40 % from its initial value when passing from 0 % to 2 % interlayer expansion. For higher out-of-plane relax-

ation the TMR magnitude starts to increase linearly up to 1000 %. In the second case, Fe/FeO/MgO/Fe, the TMR values are around zero. As the relaxation increases, the TMR decreases also by more than 40 %. However, in this case, the TMR switches to negative values for relaxations larger than 2 %.

7.5 Discussion

Although the interface oxidation of Fe/MgO is still a quite controversial topic, few percentage of oxygen at the interface is already sufficient to induce a large relaxation. Furthermore, some recent transmission electron microscopy measurements show that even for a sharp Fe/MgO interface the Fe-Fe interlayer distance is expanded by 4 % from the Fe bulk lattice parameter [115]. Thus, even if there is no oxidized layer at the interface, the out of plane relaxation is still quite large. As mentioned before, experiments show that the oxidation of the last Fe layer is found for one interface and not for both. Therefore, the Fe/MgO/Fe asymmetric structure is the most realistic one.

Both oxidized and non-oxidized interface for asymmetric structure showed a reduction of the TMR values as function of the out-of-plane relaxation. In the non-oxidized interface the TMR value is reduced by 40 % for small inter-layer relaxation. However, for large relaxation the TMR starts to increase. In the case of oxidized layer, the reduction is even larger and reaches 60 %. Although, the obtained TMR values in this case are much reduced with respect to the experimental ones, we are more concerned about the qualitative behavior of the TMR as a function of the relaxation. In the case of Fe/FeO/MgO/FeO/Fe we should note that the TMR is largely reduced from its intial value. It is only in the symmetric Fe/MgO/Fe that the TMR is not reduced, but rather it increases up to high values of about 7000%.

7.6 Conclusion

In conclusion, the transport properties of Fe/MgO/Fe MTJs are studied as a function of the Fe-Fe interlayer distances near the interface. The behavior of the TMR as a function of the relaxation depends on whether the structure is symmetric or asymmetric, and whether the interface is oxidized or not. In general, the TMR is largely reduced for asymmetric relaxation bringing the

theoretical TMR closer to their experimental counter part. We hope this work helps in understanding the low values observed in experiment.

Recently the group of Kirschner [116] suggested oxidizing the second interface of the MTJ to enhance the observed TMR value in experiment. However, our calculation shows a qualitatively large reduction of TMR for Fe/FeO/MgO/FeO/Fe as function of relaxation. Therefore, symmetric oxidized interfaces might not enhance the observed values in experiment. One possible alternative to enhance the observed TMR magnitude is by symmetrizing the interface of Fe/MgO/Fe MTJs, by contaminating the interfaces with an appropriate element or compound that would lead to a similar relaxation on both interfaces.

Chapter 8

General Conclusion

Spin-dependent transport (SDT) in magnetic tunnel junctions is a rapidly developing research field that attracted recently worldwide attention. The interest in this field is not only for its fundamental aspects but also for its possible applications, in particular in storage technology. The interfacial electronic structure between a magnetic and a non-magnetic film plays an important role in determining the SDT properties. The present thesis contributes to this field by a combined experimental and theoretical study on the influence of lattice relaxations on the SDT properties in ferromagnetic materials.

The first type of relaxation investigated in this thesis is the lattice relaxation of Fe films during their growth on a Ag(001) crystal. We report the discovery of 180 ° electron-spin precession in spin-polarized electron reflection experiments on Fe films on Ag(001), the largest possible precession angle in a single electron reflection. Both, experiments as a function of Fe film thickness and *ab initio* calculations show that the appearance of this ultimate spin precession depends with utmost sensitivity on the relaxation of the Fe surface layers during growth. Similar spin precession is also predicted for other ferromagnetic films.

The second type of relaxation studied in this thesis is the surface relaxation of Fe(001) induced by MgO deposition. It is shown that the spin polarization direction of the reflected electrons on Fe(001) strongly changes with minute amounts of MgO. Our *ab initio* electronic band structure and spin-dependent electron reflection calculations reveal that the MgO-induced out-of-plane relaxation of the Fe surface layer is responsible for this behavior. Our study points towards the subtle feature that the major change of the spin-dependent electron reflection properties of the Fe(001) surface is already caused by the very first MgO coverage.

The latter results have motivated us to investigate the effect of lattice relaxations on the transport properties of Fe/MgO/Fe magnetic tunnel junctions. The conductance coefficients were calculated for different degrees of relax-

ation. First, both interfaces where relaxed (symmetric structure) by varying the out-of-plane relaxation at the interface. Second, only one interface is relaxed (asymmetric structure). In both cases, the calculated TMR depends on whether the interface is oxidized or not. In general, the asymmetric structures show a large reduction of the TMR values for small out-of-plane relaxation. However, the symmetrization of the structures in the non-oxidized layer leads to a large TMR for large relaxation values. We think that the asymmetric results may help in understanding the reduced TMR values found in experiments. We suggest that a symmetrization of the structure by introducing an appropriate element at the interface (not just by oxidation as has been proposed by other groups) might help in enhancing the experimental TMR values.

In general, lattice relaxation plays an important role in determining the SDT properties in magnetic/non-magnetic film systems. Even if the relaxation is quite small, it still might have a strong effect on the spin-dependent reflection properties, as we have seen in the case of Fe/Ag(001). I hope that this work will motivate further experimental and theoretical investigations on the effect of lattice relaxations on the spin-dependent transport.

Bibliography

[1] P. Bose, A. Ernst, I. Mertig, and J. Henk, Phys. Rev. B **78**, 092403 (2008). III, 1, 104

[2] Youqi Ke, Ke Xia, and Hong Guo, Phys. Rev. Lett. **105**, 236801 (2010). III, 1

[3] J. Mathon and A. Umerski, Phys. Rev. B **74**, 140404 (2006). III, 1, 102, 104

[4] M. Müller, F. Matthes, and C.M. Schneider, Europhys. Lett. **80**, 17007 (2007). III, 1, 88

[5] H.X.Yang, M.Chshiev, A.Kalitsov, A.schuhl, and W.H.Bulter, Appl. Phys. Lett. **96**, 262509 (2010). III, 1

[6] Xiaobing Feng, O. Bengone, M. Alouani, S. Lebègue, I.Rungger and S.Sanvito, Phys. Rev . B **79**, 174414 (2009). III, 1

[7] D. Oberli, R. Burgermeister, S. Riesen, W. Weber, and H.C. Siegmann, Phys. Rev. Lett. **81**, 4228 (1998). IV, 2

[8] W. Weber, D. Oberli, S. Riesen, and H.C. Siegmann, New J. Phys. **1**, 9.1 (1999). IV, 2

[9] A. Chambers and D.C Jackson, Philos. Mag. **31**, 1357 (1975). IV, 2, 77

[10] O. K. Andersen, Phys. Rev. B **12**, 3060 (1975) and references therein. V, 3, 50

[11] J. Henk, *Handbook of Thin Film Materials*, edited by H. S. Nalwa (Academic, San Diego, CA, 2001). V, 3, 69

[12] H. L. Meyerheim *et al.*, Phys. Rev. B **65**, 144433 (2002). V, XVI, 3, 88, 94, 96

[13] S. Yuasa, T. Nagahama, A. Fukushima, Y. Suzuki, and K. Ando, Nature Materials **3**, 868 (2004). 5

[14] S. S. P. Parkin *et al.*, Nature Materials, **3**, 12, 862-867 (2004). 102

[15] W. Gerlach, O. Stern, Zeitschrift für Physik **9** 353-355 (1922). 9

[16] O. Stern, Zeitschrift für Physik **7** 249-253 (1921). 10

[17] Arnold Sommerfeld Atombau und Spektrallinien. Braunschweig (1924). 10

[18] T. E. Phipps, J. B. Taylor, "The Magnetic Moment of the Hydrogen Atom". Physical Review **29** (1927). 10

[19] S. Goudsmit and G.E. Uhlenbeck, Physica **6** 273 (1926). 10

[20] J.Kessler, *Polarized Electrons*, Springer Series on Atoms and Plasmas, second edition (1985). 15, 16

[21] W. Thomson, Proceedings of the Royal Society of London **8**, 546 (1856). 17

[22] M.N. Baibich, J.M. Broto, A. Fert, F. Nguyen van Dau, F. Petroff, P. Eitenne, G. Creuzet, A. Friederich, and J. Chazelas, Phys. Rev. Lett. **61**, 2472 (1988). 17

[23] G. Binasch, P. Grünberg, F. Saurenbach, and W. Zinn, Phys. Rev. B **39**, 4828 (1989). 17

[24] M. Julliere, Phys. Lett. A **54**, 225 (1975). 18

[25] R. Landauer, IBM J. Res. Dev. **1**, 223 (1957). 19

[26] M. R. O'Neill, M. Kalisvaart, F. B. Dunning, and G. K. Walters, Phys. Rev. Lett. **34**, 1167 (1975). 19

[27] E Bauer *et al.*, J. Phys. D: Appl. Phys. **35** 2327 (2002). 19

[28] S. Samarin, O. M. Artamonov, A. D. Sergeant, J. Kirschner, and J. F. Williams, Journal of Physics: Conference Series **100** 072033 (2008). 19

[29] S. Ikeda, J. Hayakawa, Y. Ashizawa, Y.M. Lee, K. Miura, H. Hasegawa, M. Tsunoda, F. Matsukura and H. Ohno Appl. Phys. Lett. **93**, 082508 (2008). 102

[30] J.Stöhr, H.C.Siegmann, *Magnetism From Fundamentals to Nonoscale Dynamics*, Springer, (2006). 15

[31] H.-J. Drouhin, N. Rougemaille, J. Appl. Phys. **91**, 9948 (2002). 21

[32] D.T.Pierce, R.J.Celotta, G.-C.Wang, W.N.Unertl, A.Galejs, C.E.Kuyatt, and S.R.Mielczarek, *GaAs Spin Polarized Electron source*, Rev. Sci. Instrum. 51, 478-499(1980). 26

[33] M. Born and J. R. Oppenheimer, Ann. Phys. **87**, 457 (1927). 40

[34] V. Fock, Z. Phys. **61**, 126 (1930). 40

[35] V. Fock, Z. Phys. **62**, 795 (1930). 40

[36] P. Hohenberg and W. Kohn, Phys. Rev. **136**, 864 (1964). 40

[37] W. Kohn and L. L. Sham, Phys. Rev. **140**, 1133 (1965). 40

[38] D. M. Ceperly and B. J. Alder, Phys. Rev. Lett. **45**, 566 (1980). 46

[39] A. D. Becle, Phys. Rev. A **38**, 3098 (1988). 47

[40] Y. Wang and J. P. Perdew, Phys. Rev. B **44**, 13298 (1991). 47

[41] J. P. Perdew, K. Burke, and M. Ernzerhof, Phys. Rev. B **77**, 3865 (1996). 47

[42] V. Anisimov, F. Aryasetiawan, and A. I. Lichtesntein, J. Phys. Condens Matter **9**, 767 (1997). 47

[43] J. C. Slater, Phys. Rev. **51**, 846 (1937). 48

[44] J. C. Slater, Phys. Rev. **92**, 846 (1953). 48

[45] M. M. Saffren and J. C. Slater, Phys. Rev. **92**, 1126 (1953). 48

[46] O. K. Andersen, Phys. Rev. Lett. **8**, 149 (1964). 48

[47] J. Korringa, Physica **13**, 392 (1947). 48, 61

[48] W. Kohn and N. Rostoker, Phys. Rev. **94**, 1111 (1954). 48, 61

[49] D. D. Koelling and G. O. Arbman, J. Phys. F: Metal Phys. **5**, 2041-53 (1975). 50

[50] D. J. Singh, *Planewaves, Pseudopotentials and the LAPW Method* Kluwer Academic Publishers, Boston/Dordercht/LONDON (1994). 51

[51] D. R. Hamann, Phys. Rev. Lett. **42**, 662 (1979). 51

[52] M. Weinert, J. Math. Phys. **22**, 2433 (1981). 52

[53] W. Ning, C. Kailai, and W. Dingsheng, Phys. Rev. Lett. **56**, 2759 (1986). 56

[54] O. K. Andersen, in *Computational Methods in Band Theory*, edited by P. M. Marcus, J. F. Janak, and A. R. Williams, Plenum, New York (1971). 56

[55] H. Skriver, *The LMTO Method*, Springer, New York (1984). 58

[56] O. K. Andersen, and O. Jepsen, Physica **91**, 317 (1977). 59

[57] C. Davisson, L.H. Germer, Physical Review **30** (6): 705-740 (1927). 60

[58] M.A. Van Hove, W.H. Weinberg, C. M. Chan . *Low-Energy Electron Diffraction* Springer-Verlag, Berlin Heidelberg New York (1986). 60

[59] R. Feder, Solid State Commun. **31**, 821 (1979). 60

[60] R. Feder, J. Phys. C: Soild State Phys. **14** 2049 (1981). 60

[61] R. Feder, in *Polarized Electrons in Surface Physics* (R. Feder, Ed.). Advanced Series in Surface Science, World Scientific, Singapore, (1985). 60

[62] J. Kirschner and R. Feder, Phys. Rev. Lett. **42**, 1008 (1979). 60, 67

[63] J. B. Pendry *Low Energy Electron Diffraction*, Academic Press, London, (1974). 60

[64] J. B. Pendry, Phys.Rev. B **40**, 12164 (1989). 60

[65] A. Gonis, *Green Functions for Ordered and Disordered Systems*, Studies in Mathematical Physics, Vol. **4**. North-Holland, Amsterdam, (1992). 64

[66] http://www.fkf.mpg.de/andersen/LMTODOC/LMTODOC.html. 69

[67] http://www.flapw.de/pm/index.php. 69

[68] G. C. Smith, H. A. Padrmore, and C. Norris, Surf. Sci. **119**, L287 (1982). 74

[69] B. Heinrich, S. T. Purcell, J. R. Dutcher, K. B. Urquhart, J. F. Cochran. and A. S. Arrott, Phys. Rev. B **38**, 12879 (1988). 74

[70] P. J. Schurer, Z. Celinski, and B. Heinrich, Phys. Rev. B **51**, 2506 (1995). 74

[71] H. Li, Y. S. Li, J. Quinn, D. Tian, J. Sokolov, F. Jona, and P. M. Marcus, Phys. Rev. B **42**, 9195 (1990). 74

[72] J. Massies and N. Grandjean, Phys. Rev. Lett. **71**, 1411 (1993). 76

[73] J. Fassbender, U. May, B. Schirmer, R. M. Jungblut, B. Hillebrands and G. Güntherodt, Phys. Rev. Lett. **75**, 4476 (1995). 76

[74] L. Tati Bismaths, L. Joly *et al*, Phys. Rev. B **77**, 220405(R) (2008). 76

[75] L. Tati-Bismaths, *Etude du mouvement du spin d'électrons dans les puits quantiques dépendants du spin*, Thèse de doctorat, Université Louis Pasteur, (2008). 76

[76] J. W. Matthews and J. L. Crawford, Thin Soild Films **5**, 187 (1970). 77, 78

[77] L. B. Freund, J. Appl. Phys. **68**, 2073 (1990). 77, 78

[78] J. L. Vassent, M Dynna, A. Marty, B. Gilles and G. Patrat, J. Appl. Phys. **80**, 5727 (1996). 77

[79] S. Tanuma, C.J. Powell and D.R. Penn, Surf. Interface Anal. **17**, 927 (1991). 75

[80] T. Kebe, K. Zakeri, J. Lindner, M. Spasova, and M. Farle, J. Phys. Condens. Matter **18**, 8791 (2006). 81, 94

[81] C. Ramsauer, Ann. Physik **4**, 513 (1921). 83

[82] J.S. Townsend and V.A. Bailey, Philos. Mag. **43**, 593 (1922). 83

[83] D. Sébilleau, *private communication*. 85

[84] W. H. Butler, X.-G. Zhang, T. C. Schulthess and J. M. MacLaren, Phys. Rev. B **63**, 054416 (2001). 87, 102, 103, 104

[85] G. X. Miao *et al.*, Phys. Rev. Lett. **100**, 246803 (2008). 87

[86] L. Plucinski, Y. Zhao, B. Sinkovic and E. Vescovo, Phys. Rev. B **75**, 214411 (2007). 88

[87] P. Luches, S. Benedetti, M. Liberati, F. Boscherini, I. I. Pronin and S. Valeri, Surf. Sci. **601**, 3902 (2007). 88

[88] M. Sicot, S. Andrieu *et al.*, Phys. Rev. B **68**, 184406 (2003). 88, 93

[89] Y. S. Dedkov, M. Fonin, U. Rüdiger and G. Güntherodt, Applied Physics A **82**, 489 (2006). 88

[90] C. Heiliger, P. Zahn and I. Mertig, J. Magn. Magn. Mater. **316**, 478 (2007). 88

[91] S. G. Wang, G. Han, H. G. Yu, Y. Jiang, C. Wang, A. Kohn and R. C. C. Ward, J. Magn. Magn. Mater. **310**, 1935 (2007). 88, 104

[92] H. L. Meyerheim, R. Popescu, J. Kirschner, N. Jedrecy, M. Sauvage-Simkin, B. Heinrich, and R. Pinchaux, Phys. Rev. Lett. **87**, 076102 (2001). 88, 104

[93] M. Klaua *et al.*, Phys. Rev. B **64**, 134411 (2001). 89

[94] J.L. Vassent, A. Marty, B. Gilles and C. Chatillon, J. Cryst. Growth **219**, 434 (2000). 89

[95] M. Suleman and E.B. Pattinson, Surface Science **35**, 75 (1973). 89

[96] Y.Z. Wu, A.K. Schmid and Z.Q. Qiu, Phys. Rev. Lett. **97**, 217205 (2006). 90, 91

[97] M. A. Muellar, T. Miller and T. C. Chiang, Phys. Rev. B **41**, 5214 (1990). 90

[98] M.P. Seah and W.A. Dench, Surf. Interface Anal. **1**, 2 (1979).

[99] W. Schmitt, H. Hopster and G. Güntherodt, Phys. Rev. B **31**, 6 (1985). 92

[100] K. Oguz, P. Jivrajka, M. Venkatesan, G. Feng and J.M.D. Coey, J. Appl. Phys. **103**, 07B526 (2008). 92

[101] C. Li and A.J. Freeman, Phys. Rev. B **43**, 780 (1991). 93

[102] J. Sokolov *et al.*, Solid State Commun. **49**, 307 (1984). 93

[103] K.O. Legg, F. Jona, D.W. Jepsen and P.M. Marcus, Phys. Rev. B **16**, 5271 (1977). 94

[104] Y. Sakisaka, T. Miyano and M. Onchi, Phys. Rev. B **30**, 6849 (1984). XVI, 95

[105] W. H. Bulter, Sci. Technol. Adv. Mater. **9**, 014106 (2008). XVI, 103

[106] X. G. Zhang, W. H. Butler, and A. Bandyopadhyay, Phys. Rev. B **68**, 092402 (2003). 104

[107] C. Zhang, X.-G. Zhang, P. S. Krstic, Hai-ping Cheng, W. H. Butler, and J. M. MacLaren, Phys. Rev. B **69**, 134406 (2004). 104

[108] F. Bonell, A. M. Bataille, S. Andrieu, C. Tiusan, B. Kierren, G.Lengaigne, and D. Lacour, Eur. Phys. J.: Appl. Phys. **43**, 357 (2008). 105

[109] F. Bonell, S. Andrieu, A. M. Bataille, C. Tiusan, and G. Lengaigne, Phys. Rev. B **79**, 224405 (2009). 105

[110] S. Sanvito, *Handbook of Computational Nanotechnology*, American Scientific Publishers, California (2004). 105

[111] I. Rungger and S. Sanvito, Phys. Rev. B **78**, 035407 (2008). 108

[112] A. R. Rocha *et al*, Phys. Rev. B **73**, 085414 (2006). 108

[113] http://www.smeagol.tcd.ie. 108

[114] F. J. Palomaresa and C. Munuera, C. Martinez Boubeta and A. Cebollada, J. Appl. Phys. **97**, 036104 2005. 108

[115] C. Wang, A. Kohn, S. G. Wang, L. Y. Chang, S.-Y. Choi, A. I. Kirkland, A. K. Petford-Long, and R. C. C. Ward, Phys. Rev. B **82**, 024428 (2010). 113

[116] C. Tusche, H. L. Meyerheim, N. Jedrecy, G. Renaud, A. Ernst, J. Henk, P. Bruno, and J. Kirschner PRL 95, 176101 (2005). 114